CONTROLLING CARBON SURFACES WITH PORES AND COATINGS FOR ENERGY APPLICATIONS

A Dissertation

Presented to the Faculty of the Graduate School

of Cornell University

In Partial Fulfillment of the Requirements for the Degree of

Doctor of Philosophy

by

Brian Patrick Williams

January 2017

CONTROLLING CARBON SURFACES WITH PORES AND COATINGS FOR ENERGY APPLICATIONS

Brian Patrick Williams, Ph. D.

Cornell University 2017

In the past decade new and complex methods were developed to create hierarchically porous carbon materials which have found applications in areas such energy storage, catalytic supports, and adsorbents. Carbon is used in these applications because it can have both high surface area and high conductivity but remain relatively inert. Due the versatile nature of carbon chemistry, there are dozens of precursors and methods to create porous carbon from soft and hard templating and post-treatments to modify the surface chemistry. However a majority of these templating techniques can be slow and difficult processes. As such it is desirable to develop simple methods to maintain control over hierarchical pores and the corresponding surface chemistry.

In a series of projects, the carbon surfaces were modified with pores and coatings for various energy applications. First, carbon in the form of petroleum coke, was modified by physically adsorbing ionic and nonionic polymers onto the surface to disperse and stabilize the particles in slurry for gasification. Atomic force microscopy, adsorption isotherms, and rheology were used to show the nature of the dispersion, stabilization, and yield stress of the slurry. Second, carbon with tunable hierarchical pores was developed for use as an interlayer in lithium sulfur batteries and tested for high rate capacity. The mesoporous carbon was produced from electrospinning immiscible blended polymers and subsequent heat treatments.

The macro- and micro- pores are a natural product of the electrospinning and heat treatments. A fundamental study of the overall sulfur loading and the thickness of the interlayer was also conducted. Finally, large hierarchical mesopores were tested as zinc bromine redox flow battery cathodes and modified with metal oxide coatings. The effect of pore size on rate capabilities is considered again as well as the catalytic, adsorptive, and protective effects of the metal oxide coating.

BIOGRAPHICAL SKETCH

Brian Williams pursued his Ph.D at Cornell University under the supervision Professor Yong Lak Joo in the Robert Frederick Smith School of Chemical and Biomolecular Engineering. He received his Bachelor's degree in Chemical Engineering from Rensselaer Polytechnic Institute in 2011. He graduated from Hamden High School in 2007 as the salutatorian of his class in the town where he was raised. His research interests are mesoporous carbons and carbon surfaces for energy storage.

To all the loving friends and family who tolerate me…

ACKNOWLEDGMENTS

I would like to acknowledge for Axium Nano, LCC for its continual funding over my research, my advisor Prof. Joo, and all Joo group members for their advice and support.

TABLE OF CONTENTS

CHAPTER 1

Introduction

The Versatility of Carbon

Known to the ancient Egyptians and Sumerians for smelting ores for bronze as early as 3750 BC, carbon was a driving force for discovery in the coming Iron Age.[1-2] Today carbon is still an important area of research. Carbon is the fourth most abundant element in the universe and seventeenth by mass in the Earth's crust.[3] It prevalence throughout life is owed to the wide array of stable bonds it can form with a coordination number commonly seen up to four and five for organometallic compounds.[3-4] When carbon is considered on its own, there is still great variation from bond order, crystallinity, shape, and range of order. Until 1985, carbon was primarily viewed with two allotropes, diamond and graphite.[3] After fullerenes were discovered that year, new effort went towards synthesizing new carbon materials. Since then graphene, nanotubes, nanoribbons, fullerenes, amorphous carbon, polymer-like carbon, nano-onions, carbynes, carbon nanofoam, and linked structures have been added to the major groups of carbon allotropes.[3-5] Listing all the allotropes of carbon would be a difficult task as new forms are readily being discovered and a single category can have many variations. For instance, carbon nanotubes can be single or multi-walled and can have three conformations, zigzag, armchair, or chiral.[3] Beyond the allotropes, there are engineering carbons, such carbon blacks, glassy carbon, and activated carbon derived from various petroleum and organic precursor sources which contain disordered microstructures of graphite, sp^3 hybridized carbon, and graphene.[4,6]

The wide array of structures and properties carbon has to offer has lead to a diverse field of applications from energy storage to biomolecule caging, catalysis, filtration, dyes, and thermal, mechanical, and electrical composite additives.[3] Over the years, carbon has found use in energy and energy storage applications because it can be: 1. electrical conductive, 2.

chemically inert, 3. porous on multiple length scales, 4. high in surface area, 5.chemically modified at the surface, and 6. made from relatively abundant precursors.[7-8] For an electric energy storage device, electrical conductivity is key to functionality from a supercapacitor to a battery to transport electrons. The delocalized pi bonds in graphitic or graphene like carbons with long range order are essential for transporting those electrons in carbon,[3] a feature rarely found in other nonmetallic materials. However, carbon is only used if chemical inertness or surface area also was desired where metals and their alloys would not due. Today's supercapacitors use nanostructured carbons because traditional capacitors do not provide the needed surface area.[7-8] As a testament to its general inertness, graphite fibers are used as wires in high temperature furnace since they can also withstand the oxidative conditions at high temperatures. Carbon can also withstand highly corrosive environments as well.[7] However, oxygen containing functional surface groups, which are found naturally or can be added by oxidizing agents or heat treatments, creates further possibilities to functionalize the surface and tailor it to a particular application.[6]

Carbon is also relatively inexpensive since precursors are abundant.[9-10] Many organics and polymers with carbon in them can be lumped in a generalized set of reactions upon thermal degradation leading to sp^2 hybridized carbon.[9-10] Perhaps in the case of petroleum thermal cracking, precursors are too common.[11] Petroleum coke is a solid carbon, coal-like by product produced in large and growing quantities during the oil refinery process of heavy oils.[12] Like coal, the chemical energy stored in the carbon bonds in petcoke can be released with traditional open furnaces and boilers but is rich in sulfur and other metal contaminants which makes the practice environmental unfriendly.[12-13] Petcoke can be partially oxidized in gasifiers to reduce pollutant emissions and produce higher value products.[13] In Chapter 2, a study is conducted to modify the surface of petcoke by adsorbing polymeric dispersants and stabilizers to improve the properties of water-petcoke slurries for gasification and pumping purposes.

In Chapters 3 and 4, the ability and application to create pores is examined. Carbon can be made porous at any length scale.[14-15] Activation processes to create micropores (<2nm) are well established. More recently, techniques have been developed to make mesopores (≥2nm and ≤50nm) and in part macropores (>50nm) from templating and phase separation strategies.[14-15] By electrospinning a blend of a carbonizing and a pyrolyzing polymer, mesoporous carbon nanofibers with large mesopores (>10nm) and with macroporous spaces between fibers were made with a presumably more cost effective method than silica templating or resol resins.[16-17] Physical activation with air added micropores to create hierarchical pores. Compared to other typical works with mesopores,[16] the mesopores that were produced were larger and the effect of the change in pore size was examined for two applications along with other fundamental studies related to the application. In Chapter 3, the mesoporous carbon nanofibers are applied as a lithium sulfur interlayer to extend the capacity retention of lithium sulfur batteries and enhance rate capabilities where large mesopores could be more advantageous than small mesopores. A fundamental study on the effect of the overall sulfur loading and the weight of the interlayer is also conducted to address scalability.

In Chapter 4, the same mesoporous carbon nanofibers are applied as a zinc bromine redox flow battery cathode. The reasoning behind this project was that the large mesopores may better accommodate the bulky, phase separated bromine complex. Along with the effect of pore size on rate capability, the catalytic, adsorptive, and protective effects of metal oxide coatings on the nanofibers are considered. Metal oxide coatings were originally proposed for this project to provide a robust protective layer from deep cycling reactions on the carbon electrode and after investigation the coatings seemed to provide other benefits as well. While the title of this work, controlling carbon surfaces with pores and coatings for energy applications, is indeed broad, it is hoped that readers will see the themes of carbon surfaces, pores, and coatings coming through throughout the work and that they will enjoy the read.

REFERENCES

1. Cecen, Ferhan and Ozgur Aktas. Activated Carbon for Water and Wastewater Treatment. Wiley-Vch. (2012) Google Books
2. Gascoigne, Bamber. "History of Metallurgy" HistoryWorld. From 2001, Retrived 8/10/16, http://www.historyworld.net/wrldhis/PlainTextHistories.asp?ParagraphID=bba
3. Miessler, Gary and Donald Tarr. Inorganic Chemistry Fourth Edition. Pearson Education, Inc. (2011), Print.
4. Burchell, Timothy. Carbon Materials for Advanced Technologies. Pergamon. (1999), Google Books
5. "Allotropes of Carbon." Boundless Chemistry. Boundless, 26 May. 2016. Retrieved 8/10/16, https://www.boundless.com/chemistry/textbooks/boundless-chemistry-textbook/nonmetallic-elements-21/carbon-150/allotropes-of-carbon-582-3569/
6. H.P. Boehm, Some aspects of the surface chemistry of carbon black and other carbons, Carbon 32 (1994) 759–769.
7. E. Frackowiak, F. Béguin, Carbon materials for the electrochemical storage of energy in capacitors, Carbon 39 (2001) 937–950.
8. L.L. Zhang, X.S. Zhao, Carbon-based materials as supercapacitor electrodes., Chem. Soc. Rev. 38 (2009) 2520–31.
9. I. Lewis, CHEMISTRY OF CARBONIZATION, Carbon 20 (1982) 519–529.
10. Y.N. Sazanov, a. V. Gribanov, Criteria of polymer carbonization, Russ. J. Appl. Chem. 82 (2009) 473–482.
11. D. Gordon, The carbon contained in global oils, Carnegie Pap. Energy and Climate (2012).
12. L. Stockman, Petroleum Coke : the coal hiding in the Tar Sands, Oil Chang. Int. (2013).
13. B.N. Murthy, A.N. Sawarkar, N. a. Deshmukh, T. Mathew, J.B. Joshi, Petroleum coke gasification: A review, Can. J. Chem. Eng. 92 (2014) 441–468.
14. C. Liang, Z. Li, S. Dai, Mesoporous carbon materials: synthesis and modification., Angew. Chem. Int. Ed. Engl. 47 (2008) 3696–717.
15. J. Lee, J. Kim, T. Hyeon, Recent Progress in the Synthesis of Porous Carbon Materials, Adv. Mater. 18 (2006) 2073–2094.
16. L. Fu, G. Qi, R. Sahore, R. Sougrat, F.J. DiSalvo, E.P. Giannelis, Facile synthesis and application of a carbon foam with large mesopores., Phys. Chem. Chem. Phys, **15**, 19134 (2013).
17. J.G. Wang, K. Xie, B. Wei, Advanced engineering of nanostructured carbons for lithium-sulfur batteries, Nano Energy. 15 (2015) 413–444.

CHAPTER 2

Enhanced Dispersion and Stability of Petroleum Coke Water Slurries via Triblock Copolymer and Xanthan Gum: Rheological and Adsorption Studies

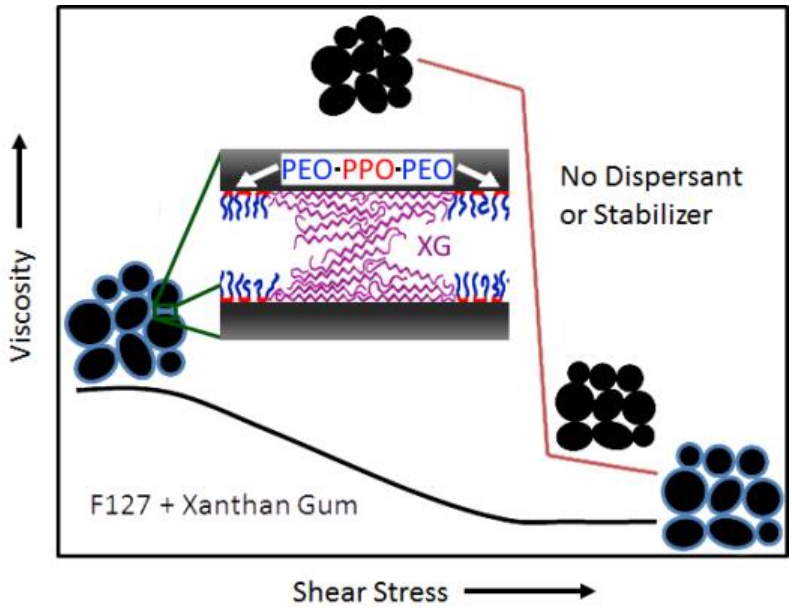

Abstract

The rheology of petroleum coke (petcoke) water slurries was investigated with a variety of nonionic and anionic dispersants including polyethylene oxide (PEO)-*b*-polypropylene oxide (PPO)-*b*-PEO triblock copolymers (trade name: Pluronic, BASF), polyvinyl alcohol (PVA), polyvinylpyrrolidone (PVP), polyethylene oxide (PEO), polycarboxylate acid (PCA), sodium lignosulfonate (SLS), and polyacrylic acid (PAA). Each effective dispersant system shared very similar rheological behavior to the others when examined at the same volume fraction from its maximum petcoke loading. Triblock copolymer, Pluronic F127 (F127), was found to be the best dispersant by comparing the maximum petcoke loading for each dispersant. The yield stress was measured as a function of petcoke loading and dispersant concentration for F127, and a minimum dispersant concentration was observed. An adsorption isotherm and atomic force

microscopy (AFM) images reveal that this effective dispersion of petcoke particles by F127 is due to the formation of a uniform monolayer of brushes where hydrophobic PPO domains of F127 adhere to the petcoke surface, while hydrophilic PEO tails fill the gap between petcoke particles. F127 was then compared to other Pluronics with various PEO and PPO chain lengths, and the effects of surface and dispersant hydrophilicity were examined. Finally, xanthan gum (XG) was tested as a stabilizer in combination with F127 for potential industrial application, and F127 appears to break the XG aggregates into smaller aggregates through competitive adsorption, leading to an excellent degree of dispersion but reduced the stability of petcoke slurries.

1. Introduction

Petcoke is a carbonaceous by-product of petroleum refineries that has seen escalating use as a gasification feedstock in recent years.[1-2] Since petcoke is low in ash but high in sulfur, nickel, and vanadium content, it is not suitable to burn directly in boilers in many parts of the world due to environmental regulations.[3] However, in the United States, the lead producer of petcoke, the supply of petcoke has increased 9% from 2009 to 2013 and exports have increased 34%.[4] These increases are primarily due to refining larger quantities of heavy, unconventional oil which have a higher propensity to form petcoke.[5-7] Petcoke is typically produced as a waste product in a delayed coker by thermally cracking the distilled fraction of petroleum too heavy for hydrocracking and fluidized bed cracking but too light for the asphalt fraction.[8] A series of radical side reactions based on thermal polymerizations, aromatic condensations, and recombinations eventually create aromatic carbon solids that will not degrade further,[6,9] thus

creating a waste by-product. As conventional oil becomes more limited and more heavy unconventional oils are refined, the supply of petcoke is expected only to increase globally.[7]

Petcoke is a prime candidate for gasification because the high levels of sulfur and heavy metal contaminants in petcoke are more cost effectively contained in gasification processes than traditional boilers.[3,10] In a gasifier, sulfur is converted to hydrogen sulfide and can be removed from the synthesis gas easily. In an entrained flow gasifier, high temperatures melt the ash and metal contaminants into a liquid slag which can be simply removed from bottom of the reactor.[11] Due to the low demand of petcoke, the low cost of the feedstock can justify the higher capital costs of the gasifier where environmental regulations are a concern.[3,10]

Entrained gasifiers partially oxidize finely ground fuel particles, typically with pure oxygen, in short residence times by achieving very high temperatures and pressures.[11] The entrained gasifiers can be fed its feedstock dry or as a slurry, but slurry is usually preferred since it can be more economically pumped to the high pressures contained within the gasifier.[3,11-12] As such, the pumping cost of the petcoke slurry is an important consideration. More water content creates a less viscous slurry, but the lower heating content from the additional water lowers the reactor's operational temperature.[13] Therefore, to maintain quick reaction rates and low residence times, a processable slurry with the highest percentage of petcoke is desirable.[13,14]

Polymeric dispersants have been used extensively at low concentrations to reduce the viscosity and yield stress of highly loaded slurries such as coal, ceramics, mining ores, or foods.[15-19] Polymeric dispersants are also useful in tuning the rheology for efficient wet grinding of a fuel feedstock.[20-21] Previous work on polymeric dispersants has been done on petcoke-oil slurries[14] and coal-petcoke slurries,[13,22-24] but only limited studies have done on petcoke-water

slurries. These studies predominately use anionic dispersants effective for coal dispersion rather than more general use ionic and anionic dispersants.[2,13]

The triblock copolymers such as polyethylene oxide (PEO)-*b*-polypropylene oxide (PPO) -*b*-PEO with varying ratios of PPO and PEO (Pluronics F127, P123, F88, F68 by BASF) have been well studied as a nonionic dispersant. The hydrophobic PPO block is well known to adsorb to hydrophobic surfaces and create a polymer brush with the hydrophilic PEO blocks extending out into the water thus increasing the degree of dispersion of a particle by steric hinderance.[25-27] Steric stabilizers are also often added to suspensions to create delicate networks to hold particles in suspension but can easily come apart under shear.[15,28] Xanthan gum (XG) is a common hydrocolloid used to stabilize suspensions and emulsions due to effectiveness at low polymer concentrations.[28] The current study looks at rheological and adsorption properties of Pluronics, xanthan gum, and other common dispersants in highly loaded petcoke slurries to reduce slurry viscosity and yield stress. This is done by examining the yield stress of the slurries to determine a maximum petcoke loading for each dispersant and comparing rheological behavior near the maximum petcoke loading. Different Pluronics were then compared to examine the relative effectiveness of different lengths of hydrophobic cores and hydrophilic tails for dispersion. AFM images were taken and an adsorption isotherm was measured to investigate the nature of the dispersant coating. Finally, XG was added to the dispersion to stabilize the slurry and to explore the interplay between a dispersant and a stabilizer. Sedimentation time and rheological behavior was measured, and AFM images were taken to show the stabilization mechanism of XG in the presence of Pluronic.

2. Experimental

Petcoke and lignite coal samples were obtained from SK Innovation in Korea. The petcoke particle size distribution was measured to be: d_{50} = 57 µm, d_{90} = 113 µm. The lignite coal was screened through a 50 µm mesh. As a model carbon system for comparison, carbonized polyacrylonitrile (PAN) was also prepared from PAN powder (M_w=50,000) available from Sarchem Laboratories, Inc. by stabilizing PAN in air for 1 hour at 270°C (1°C/min ramp) and carbonizing it in nitrogen for 20 minutes at 1000°C (10°C/min ramp). The resulting carbon was grounded and filtered through a 234 µm mesh. The Pluronics with various ratios of PPO and PEO were obtained from Sigma Aldrich and BASF. Pluronic F127 (F127), PEO:PPO:PEO = 100:65:100, was predominately used in the study. The remaining chemicals were purchased from various sources at or above ACS reagent grade unless noted. The molecular weight of the sodium lignosulfonate and polycarboxylate used in the study was measured using intrinsic viscosity and the Mark-Houwink equation.

Rheological measurements were taken with a Physica MCR 300 rheometer with a 50 mm parallel plate at a 1mm gap. Low viscosity light mineral oil was used at the edges to prevent water evaporation. Slurries were prepared with deionized water. The reported dispersant and XG weight percentages were based on the dry petcoke weight and were not considered to contribute to the total slurry weight. All percentages are based on weight unless noted. Further details of sample preparation are provided in the supporting information. Rod penetration depth settling experiment samples were sealed in 25mL scintillation vials for set periods of time until the measurement and each sample was only used for one measurement. The sediment depth was measured as the depth of sample which upheld an aluminum rod exerting 18 kPa (1.25 cm diameter, 228 g) on the sample. In samples where XG was allowed to adsorb to the petcoke first

before F127 was added, a quarter of the water was set aside to dissolve the F127 and the rest was used to disperse the XG. Petcoke was added to the dispersed XG, thoroughly mixed, and allowed to rest for 1 hour. The F127 solution was then added to the petcoke and XG and thoroughly mixed. For the time dependent rheology the time to the rheological measurement was measured from when both the XG and F127 parts were mixed together. A fresh sample was prepared for each time point shown.

AFM images were taken with an Asylum MFP-3D in tapping mode using a 100 μm silicon nitride cantilever in deionized water at a frequency of ~7 kHz and an amplitude of ~ 2-3.5 V. Petcoke was fixed to glass slides using epoxy and were allowed to equilibrate with the dispersant solution for 1 hour. The 1% F127 solutions contained the same concentration of F127 as a 1% F127 60% petcoke slurry. The 0.1% F127 solutions were made from 0.1% F127 20% petcoke slurries that were allowed to settle overnight. The liquid used in the AFM was separated from the slurry using a PTFE 0.2 μm VWR syringe filter. The petcoke slurries prepared for the F127 adsorption experiments were made with 20% petcoke and were allowed to equilibrate overnight. The liquid separated from the petcoke slurry with a syringe filter was massed and dried, and the resulting Pluronic residue was massed to calculate the amount adsorbed. The BET surface area of the petcoke was measured to be 1.7 m^2/g in liquid nitrogen with a surface area analyzer (Gemini VII 2390t, Micromeritics) to calculate surface concentrations.

3. Results and Discussion

3.1 Effect of Petcoke Loading and Dispersant on Yield Stress

Shear stress ramps were performed on petcoke slurries with 1% F127 and increasing petcoke loadings to determine their yield stresses by a sudden drop in viscosity as the loading varies. (Fig. 1a) By increasing the petcoke loading above 70%, a sharp transition from a free flowing fluid to a thick paste was visually observed as well as a sudden shift in yield stress from rheological measurements across only 2% of the loading. This sudden change in yield stress has been defined as the maximum petcoke loading, c_{max}, for F127. Observations of a maximum packing fraction are expected from theory and experimentation.[19,29] However, the apparent viscosities of slurries below and just above their maximum loading are quite similar at stresses above their yield stress despite their fluid, paste, or powder like nature at rest. Slurries below or just above the maximum loading fit to Herschel-Bulkley models well (Fig. 1b) when above the yield stress for the slurry. Slurries with measurable yield stresses showed regions of linear elasticity. The general guideline of a viscosity of 1000 mPa sec to determine the maximum loading for pumping applications[29] was found not to be appropriate given the great sensitivity of the yield stress to the petcoke loading and that above the yield stress, the resulting viscosity be can well below 1000 mPa sec. This sensitivity has been observed in other slurry systems with dispersants.[17,30]

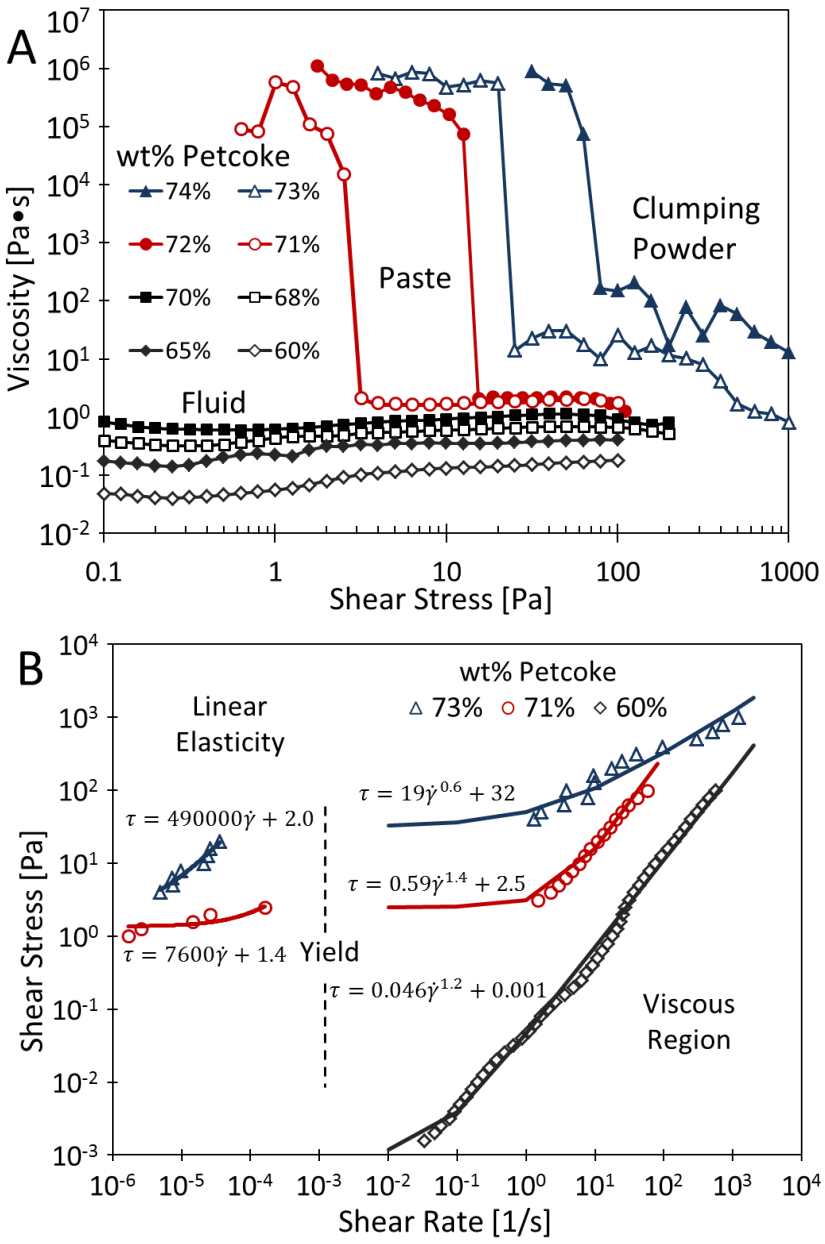
A
Viscosity [Pa•s]
wt% Petcoke
74%
73%
72%
71%
70%
68%
65%
60%
Clumping
Powder
Paste
Fluid
Shear Stress [Pa]
B
Shear Stress [Pa]
Linear
Elasticity
wt% Petcoke
73%
71%
60%
$\tau = 490000\dot{\gamma} + 2.0$
$\tau = 19\dot{\gamma}^{0.6} + 32$
$\tau = 0.59\dot{\gamma}^{1.4} + 2.5$
$\tau = 7600\dot{\gamma} + 1.4$
Yield
$\tau = 0.046\dot{\gamma}^{1.2} + 0.001$
Viscous
Region
Shear Rate [1/s]

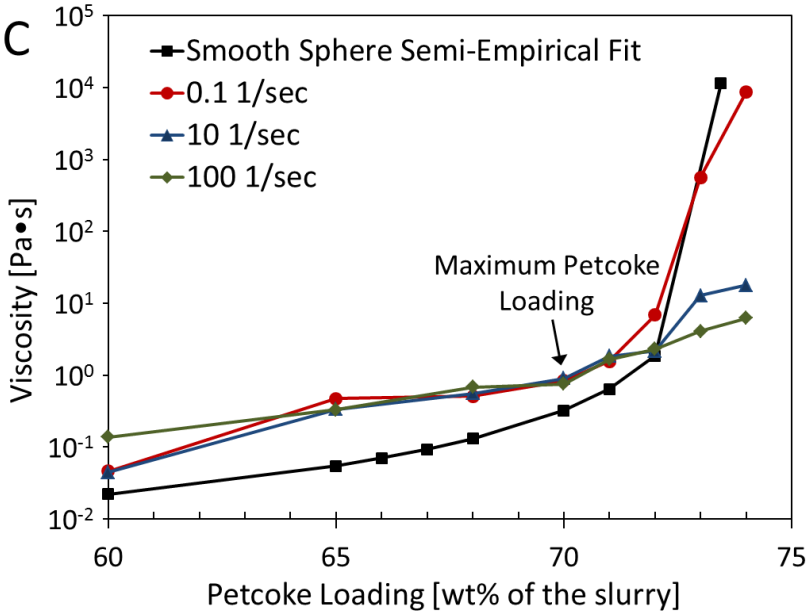

Fig. 1: a) Viscosity vs. shear stress of 1% F127 petcoke slurries with increasing petcoke loadings b) Shear stress vs. shear rate fitted to a Herschel-Bulkley model after its yield stress and to a linear fit before c) 1wt% F127 Petcoke slurry viscosity as a function of petcoke loading at three different shear rates compared to a semi-empirical fit of smooth monodisperse sphere viscosity. $\mu_r = (1-\Phi/A)^{-2}$ where A=0.68 and the real density of petcoke is 1.3g/cm^3.

Without dispersant the transition from paste to fluid and the corresponding change in yield stress gradually takes place over a range of 10% petcoke instead of ~ 2% with dispersant. In addition, without dispersant the petcoke slurry was very unstable at low petcoke loadings (~40%) and would phase separate in seconds to floating and sinking portions, while at 60%, the slurry was a stable homogenous paste. This prevented accurate rheological measurements but from general observation, without dispersant a petcoke slurry will flow under its own weight under 45% petcoke and is the assumed maximum loading without dispersant for comparison.

At low shear rates (0.1 1/sec), the rheological behavior at relatively high petcoke loadings is similar to a semi-empirical fit for smooth sphere slurries based on volume fraction described

by Maron and Pierce (Fig. 1c).[19,31] The differences observed at low petcoke loadings are possibly due to the jagged angular shape of the petcoke particles. Higher shear rates (10 and 100 1/s) did not follow the smooth sphere fit despite decreasing plate slip effects[32] possibly due to the observed sudden and strong yielding behavior resulting from significant shear induced ordering.[33-34]

Like other highly loaded suspensions, it is observed that the maximum petcoke loading highly depends on the volume fraction of the suspending fluid and solids. A nonionic polymeric dispersant, can prevent a strong direct contact between particles by its physical presence and by attracting and retaining water near the surface of the particles to hydrate the hydrophilic portion of the polymer. By this effect a dispersant can also lower the yield stress and zero shear viscosity. When the highest possible loading in slurry is desired, a good dispersant effectively raises the maximum loading by lowering the yield stress. Demonstrating the yield stress behavior similar to that of Fig. 1a for F127 and a transition from fluid to paste, a maximum petcoke loading was observed for a variety of polymeric dispersants both nonionic and anionic including polyvinyl alcohol (PVA), polyvinylpyrrolidone (PVP), polyethylene oxide (PEO), polycarboxylate acid (PCA), sodium lignosulfonate (SLS), and polyacrylic acid (PAA). (see Table 1). In Fig. 2a shear rate ramps were performed and dilatant behavior was observed for most of the dispersants at 60% petcoke with varying degrees of effectiveness. It is apparent that the infinite shear viscosity varies little with the dispersant with the exception of F127. At a sufficiently high shear stress, even petcoke slurries without dispersant nearly approach the viscosity of low yield, fluid-like slurries that use dispersants.

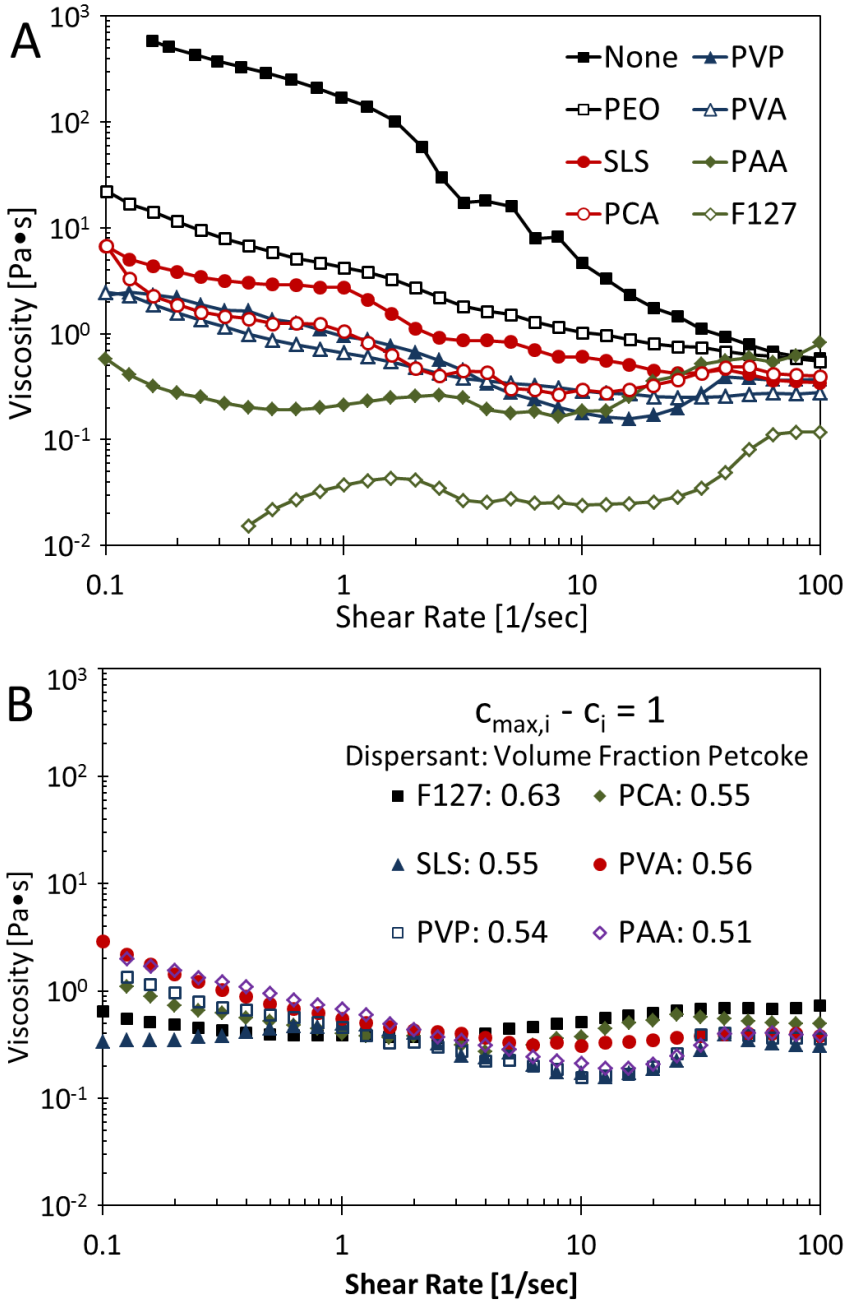

Fig. 2: a) Viscosity as a function of shear rate with 1wt% dispersant 60wt% petcoke slurries b) Dispersants in slurries that are 1vol% below their corresponding maximum loading

Fig. 2b shows that the rheological behavior of petcoke slurries can be generalized by comparing the viscosity at the same deviation of the petcoke concentration from the maximum loading, *i.e.* the difference of the particle volume fraction from that of each slurry's maximum

loading, $c_{max,i}$ - c_i for many different dispersants, i. As such, the overall rheological performance of each dispersant in slurry is easily compared by examining the value of its maximum loading. Most polymers have a maximum loading petcoke volume fraction, $c_{max,i}$ (Table 1) near but beyond the point where the void space is completely filled with fluid, calculated to be 58 vol% petcoke from the petcoke's packed bulk density (0.7g/mL). This density is close to the 60 vol% theoretical maximum volume fraction for randomly packed monodisperse spheres. Work by Yoon, *et al.* with petcoke-coal mixture slurries reported that the ionic and anionic dispersants tested were roughly equally effective for petcoke.[22] This work supports this claim except for the enhanced performance by F127. Compared to other dispersants, F127 exhibit superior performance in increasing the maximum loading to the point where the original randomly packed void space did not need to be completely filled to have fluid-like behavior. This suggests that F127 improved the packing order of the petcoke from its initial random packing. Since F127 was observed to be the most effective at increasing the maximum loading of petcoke slurries, it was selected for further studies.

Table 1: Maximum Petcoke Loading and Volume Fraction for Selected Dispersants

Dispersant	Details	Max. Petcoke Loading wt%	Volume Fraction
None	Just water and petcoke	45%	0.39
1% F127	M_w=12600 70% PEO from Sigma Aldrich	70%	0.64
1% PCA	Powerflow WD600:SD512 1:1 Tech. grade from KG Chemical, M_v=210,000	62%	0.56
1% SLS	Tech. grade from Spectrum Chemicals, M_v=110,000	62%	0.56
1% PVP	M_w=40,000 from Sigma Aldrich	61%	0.55
1% PVA	M_w=9,500, 80% hydrolyzed from Sigma Aldrich	63%	0.57
1% PAA	M_w=100,000 from Sigma Aldrich	58%	0.52
1% PEO	M_n=10,000 from Sigma Aldrich	58%	0.52
0.08% XG	Prac. Grade from MP Biomedicals, Mw≥ 2,000,000	56%	0.49
1% F127 0.08% XG	Added at the same time	67%	0.61

3.2 Surface Coverage and Adsorption

As the nature of the surface is important to the performance of a dispersant, another carbon gasification feedstock was tested in slurries with F127. A maximum loading was also obtained with F127 in lignite coal and carbonized PAN powder as a model carbon. (Fig. 3a) F127 increased the maximum loading by 25% compared to petcoke slurries with no dispersant but only increased the maximum loading by 3% for lignite and carbonized PAN. Hydrophilic surface functional groups are thought to decrease the effectiveness of the F127; both the lignite (135°) and carbonized PAN (125°) have lower contact angles than petcoke (140°). In lignite, volatile matter and ash are known to decrease polymeric dispersant effectiveness in coal and raise surface hydrophilicity.[17,30,35] Unlike lignite, carbonized PAN has a low volatile component and no ash, but it is expected that there are significant amounts of hydrophilic oxygen and

nitrogen containing functional groups on the naturally hydrophobic PAN-based carbon surface[34] which interferes with performance.

Using X-ray photoelectron spectroscopy (XPS), petcoke was measured to have a O:C ratio of 0.18, while lignite had a ratio of 0.62 and 5.9 times the atom% of Si on the surface as petcoke. Carbonized PAN had a O:C ratio of 0.13 so slightly fewer oxygen groups than petcoke but 2.6 times the nitrogen and the most hydrophilic surface according to contact angles. Another model particle such as graphite powder (133°) has relatively clean, hydrophobic surface but demonstrated little improvement in rheological behavior with F127 suggesting the importance of overall surface hydrophilicity rather than particular surface groups or the graphitic order of the carbon.

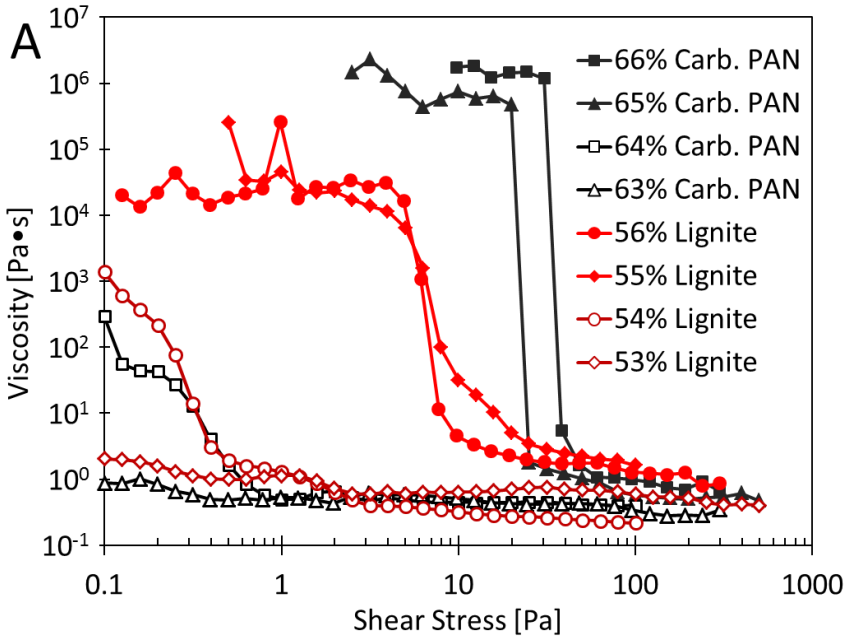

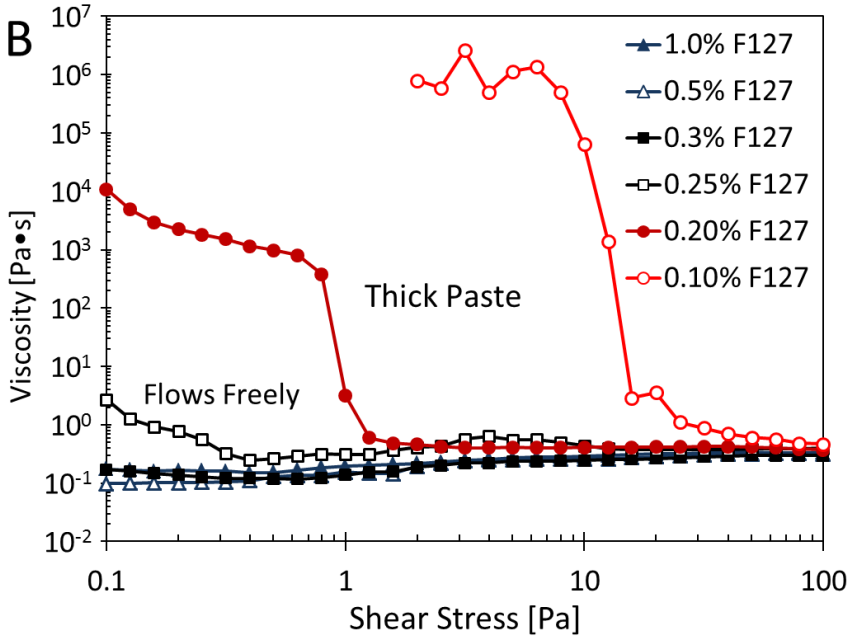

Fig. 3: a) Shear stress ramps of carbonized PAN and lignite coal at different wt% loadings b) 65wt% petcoke slurries with increasing wt% F127

Beyond the hydrophobicity of the surface, the amount of dispersant required for dispersion is important as well. In Fig. 3b shear stress ramps were performed on 65% petcoke slurries with increasing F127 concentrations to find the effective minimum F127 concentration. A transition at 0.25% F127 from a high yield stress to a negligible yield stress was observed and has been termed as the minimum dispersant concentration. Increasing the F127 concentration beyond this point seemed to have little to no effect on the slurry's viscosity after its negligible yield stress. Other dispersants (PVA, PEO, and PCA) were measured to have approximately the same minimum concentration to take effect and minimum dispersant concentrations have been observed previously in other slurry systems.[22,30,35] The minimum dispersant concentration is thought to be an effect of adsorbing enough polymer onto the surface of the petcoke to make a complete and sufficiently dense and uniform monolayer.

Atomic force microscopy (AFM) images (Fig. 4a-d) show dispersed aggregates below the minimum concentration at 0.1% F127, (Fig.4a) and a smooth saturated monolayer above it at 1% F127 (Fig. 4b). Monolayer formation is in agreement with previous work on the adsorption of Pluronic with high PEO composition on hydrophobic surfaces.[27,37-38]. The AFM images of F127 were under its critical micelle temperature (24°C at 1% F127)[30], and thus roughness created from adsorbing and desorbing micelles is not expected. PCA, an anionic dispersant (Fig. 4c), on the other hand, does not form a smooth monolayer, but small disperse aggregates. Anionic are known to adsorb less densely onto surfaces due to their charge repelling nearby adsorbed molecules,[17,39] and in many cases, the charge repulsion between particles more than makes up for an incomplete monolayer. The bare petcoke surface contains macroscopic defects (Fig. 4d), but appears to be predominately microscopically smooth (Fig. 4e) in the areas imaged.

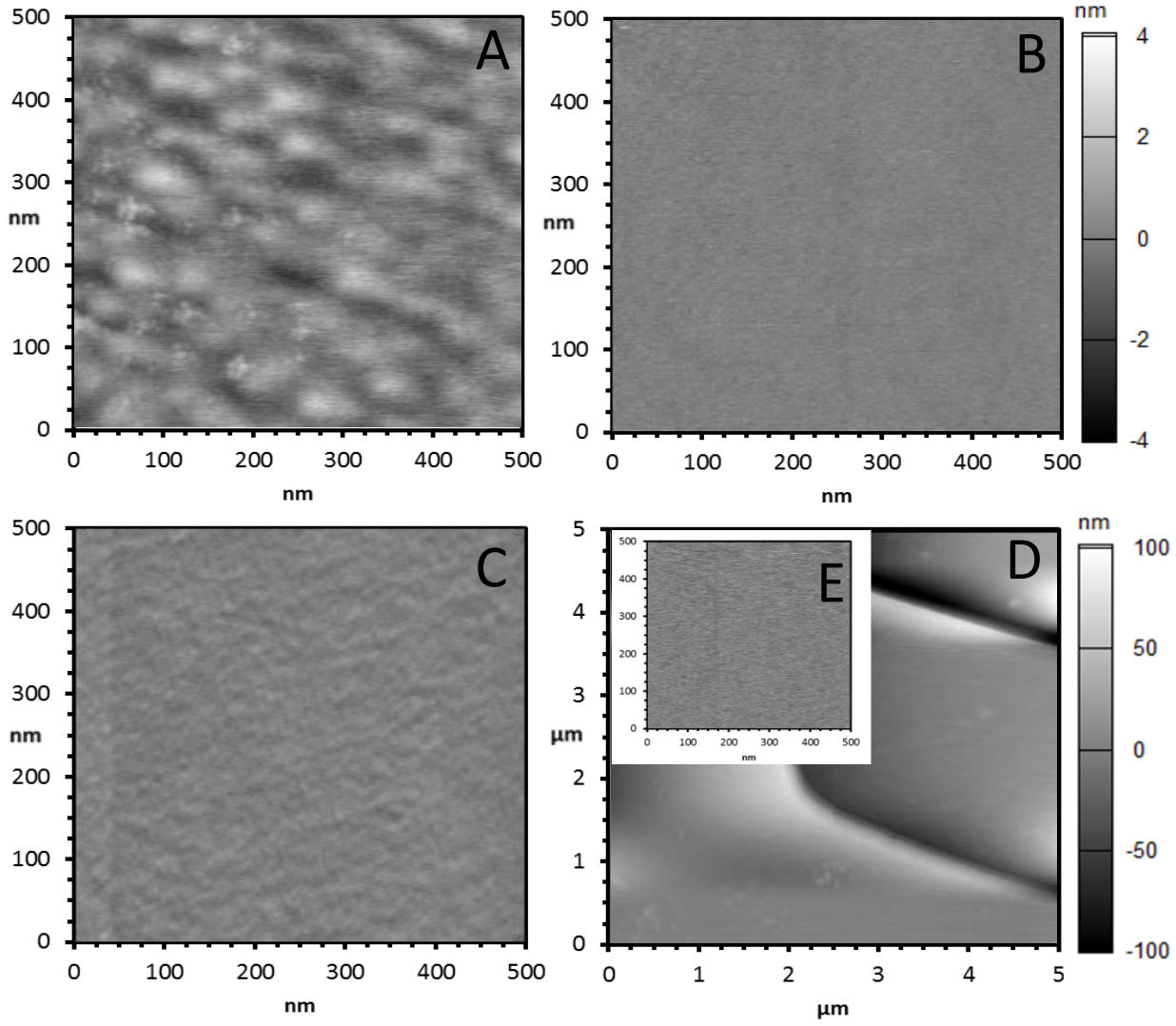

Fig. 4: AFM images of petcoke in solutions of a) 0.1% F127 b)1% F127 c) 1% PCA d,e)no dispersant. a-c,e) have a height scale of 8 nm and d) has a scale of 200nm.

The adsorption isotherm in Fig.5a shows three regions of adsorption from the approximate three regions with different slopes. The first region is monolayer adsorption supported by a previous AFM image from Fig. 4b and a reasonable fit to a Langmuir isotherm in Fig. 5a. The next two regions are thought to be multilayer adsorption above 1% F127[40] and micelle adsorption above the approximate critical micelle concentration at 5% F127.[27,38] 80% of

all the F127 in the slurry was adsorbed to the surface below 0.3% F127, which supports strong, partially irreversible adsorption in the monolayer. Above 0.3% F127, the fraction of F127 adsorbed to the surface quickly decreased meaning a majority of the easy adsorbing sites have been taken up. In Fig. 5b F127 had no significant improvement to the maximum loading after the 0.3% "minimum" concentration despite evidence from Fig. 5a showing that the surface continues to adsorb F127 after the minimum concentration. This may indicate that a strongly adsorbed monolayer is critical to petcoke dispersion rather than the combined thicknesses of the monolayer and multilayers.

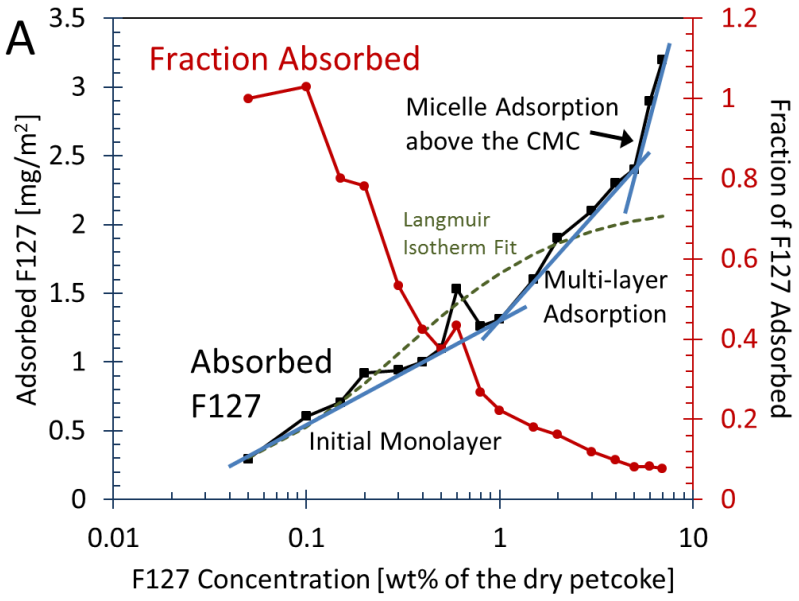

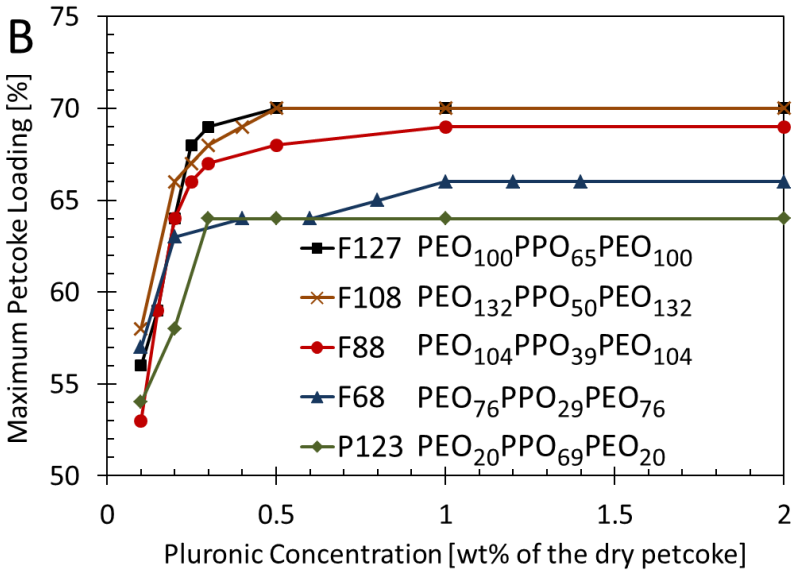

Fig. 5: a) Adsorption Isotherm of F127 on petcoke and the fraction of the total F127 that adsorbs to the petcoke surface in a 20wt% petcoke slurry. The solid lines are guides for the eye. The dashed line is a Langmuir isotherm fit: W_m= 2.15 mg F127/m^2 petcoke, K= 3.26 $wt\%^{-1}$ b) Maximum petcoke loading vs. Pluronic concentration with five types of Pluronic

In Fig. 5b, the overall length of the Pluronic and the ratio of the PEO to PPO block sizes were also varied. It is known that the hydrophobic PPO will serve as an anchor to a hydrophobic surface[41] such as petcoke (140° contact angle). Increasing the size of the PPO block presumably strengthens the anchoring connection and increases the adsorbed polymer surface density.[41] Pluronics with relatively small PPO sections such as between F127 and F108 required higher Pluronic concentrations to reach its maximum loading plateau from having a weaker interaction to the surface. P123 with the shortest PEO blocks and the longest PPO block however was the worst of the Pluronics tested. In general, increasing the length of the PEO blocks between F127, F88, F68, and P123 was more significant towards increasing the maximum loading. In literature, longer PEO blocks have been shown to increase the thickness of the adsorbed Pluronic layer on polystyrene latex beads[42-43] which would lead to more steric hindrance and lubrication. F108

though has longer PEO blocks than F127 but performed the same as F127 showing a limit to this effect.

The PPO anchor blocks are still important for the overall functionality. F88 has a smaller PPO block and approximately equally sized PEO blocks as F127, but did not perform quite as well as F127. This is also thought to be due to weaker adsorption by F88 as the adsorbed density would also decrease with smaller PPO blocks. Pure PEO homopolymer of similar M_w without hydrophobic sections is a much less effective dispersant than the least effective Pluronic, P123. (Table 1) P123 is still more effective than PEO and PVA despite having a similar correlated adsorbed layer thickness as PEO (~ 3nm at *Mw* = 10,000) and a thinner layer than PVA (~16 nm at *Mw* = 10,000) on polystyrene latex according to work by Killman *et al*.[43]

PVA also demonstrates the importance of hydrophobic anchors with petcoke which performed better than PEO and PVP containing no hydrophobic sections, although the larger PPO block anchors in Pluronic were more effective. To produce PVA, hydrophobic polyvinyl acetate is randomly hydrolyzed to the hydrophilic alcohol and if the hydrolysis is not complete, the remaining acetate groups can create hydrophobic anchor sections.[43-44] As shown in Table 2, as M_w increases, the petcoke maximum loading decreases presumably from greater polymer entanglements between particles. If the hydrolysis of PVA is nearly complete, the maximum loading drops off because there are not enough hydrophobic acetate groups to associate the polymer to the surface.

Table 2: Maximum Petcoke Loading with PVA

M_w, % Hydrolyzed	Max. Petcoke Loading wt%	M_w, % Hydrolyzed	Max. Petcoke Loading wt%
9500, 80%	65%	Not available	
18000, 88%	63%	18000, 98%	58%
25000, 88%	61%	Not available	
78000, 88%	55%	78000, 99.9%	45%

Pluronic also increases the attraction of petcoke particles to the solvent as one might expect a surfactant to. Petcoke's maximum loading in hexane without F127 is 54 vol% which is 15% higher than in water alone. When petcoke was coated in F127 by making the slurry with water and F127 and then evaporating out the water, the F127-coated maximum petcoke loading was only 49 vol% in hexane. The hydrophilic PEO tails of F127 surface negatively impacted dispersion in a hydrophobic hexane solvent suggesting that solvent attraction is a contributing factor in petcoke dispersion despite the large size of the particles. The same experiment with P123 resulted in the same maximum loading. The shorter PEO blocks in P123 should have theoretically caused less bridging between particles. However, without a change in the maximum loading it is presumed that the lower maximum loading with F127 in hexane was due to the hydrophilic surface of the petcoke particles rather than bridging effects. The hydrophilic surface is thought to increase the wettability of petcoke particles in water which would decrease the hydrophobic interactions between particles[17] and increase the maximum loading as discussed previously by drawing water close to the surface to prevent particle-particle contacts from lubrication forces.

3.3 Effect of Xanthan Gum on Stability

While F127 was found to be a good dispersant, it added little to no stability. To be industrially relevant, the slurry stability of at least a few days is required, preferably longer. Hydrocolloids like XG are added to increase the stability of suspensions and colloids by creating an additional flocculation network to keep particles separate but in place and which easily breaks down under shear stress. 0.08% XG is not an effective dispersant by itself creating a slurry with a maximum loading of 56% petcoke and lowers the maximum loading with F127 from 70% to 67% petcoke.

Fig. 6a shows how the concentration of XG affects the settling time for 1% F127 60% petcoke slurries by measuring the growth of hard packed sediment. 0.08% XG showed stability for at least one day. When XG was added and allowed to adsorb first before F127, sediment depths showed more stability. Fig. 6b shows this to be a result of increased yield stress and zero shear viscosity. Fig. 6c shows that the sediment depth changes very little between samples of different loadings below the maximum loading after 2 hours and on the verge of settling after 48 hours. The pastes that form above the maximum loading are actually quite stable but are so thick they can fully support the weight of the rod.

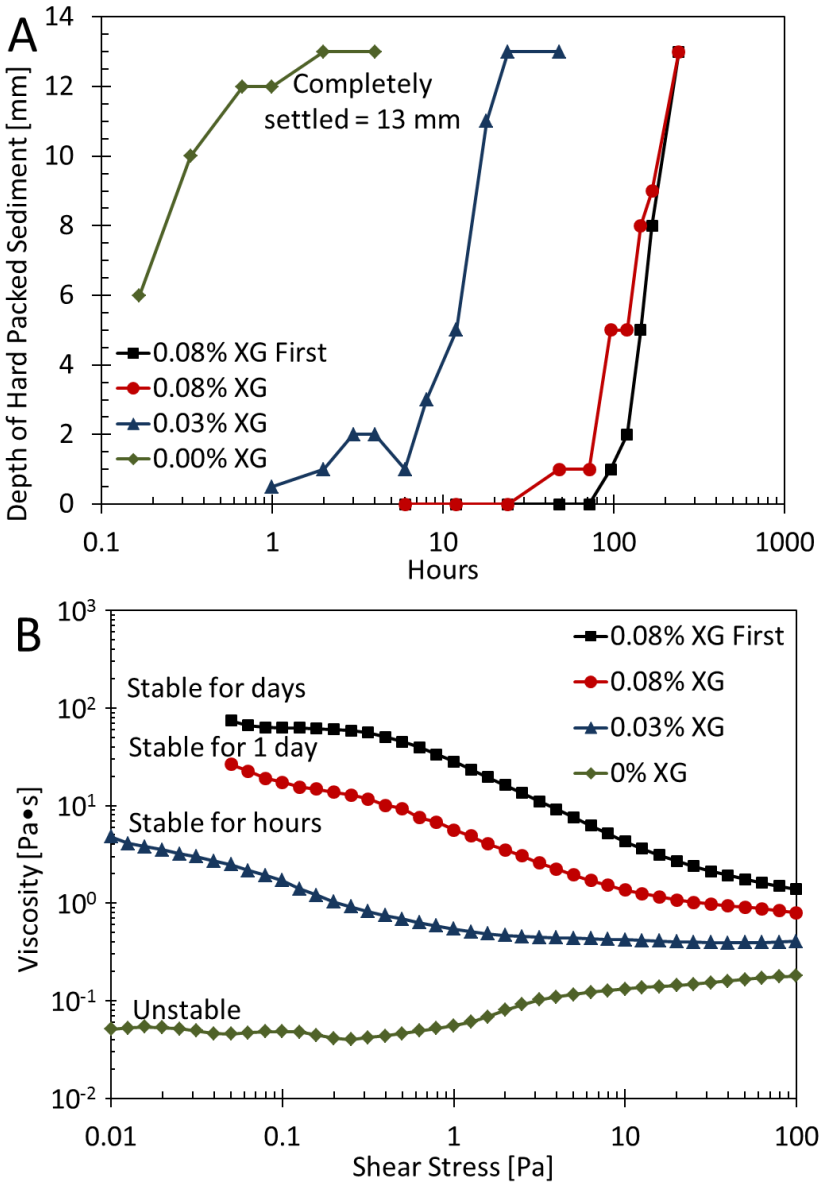
A
Depth of Hard Packed Sediment [mm]
Hours
Completely
settled = 13 mm
0.08% XG First
0.08% XG
0.03% XG
0.00% XG
B
Viscosity [Pa•s]
Shear Stress [Pa]
Stable for days
Stable for 1 day
Stable for hours
Unstable
0.08% XG First
0.08% XG
0.03% XG
0% XG

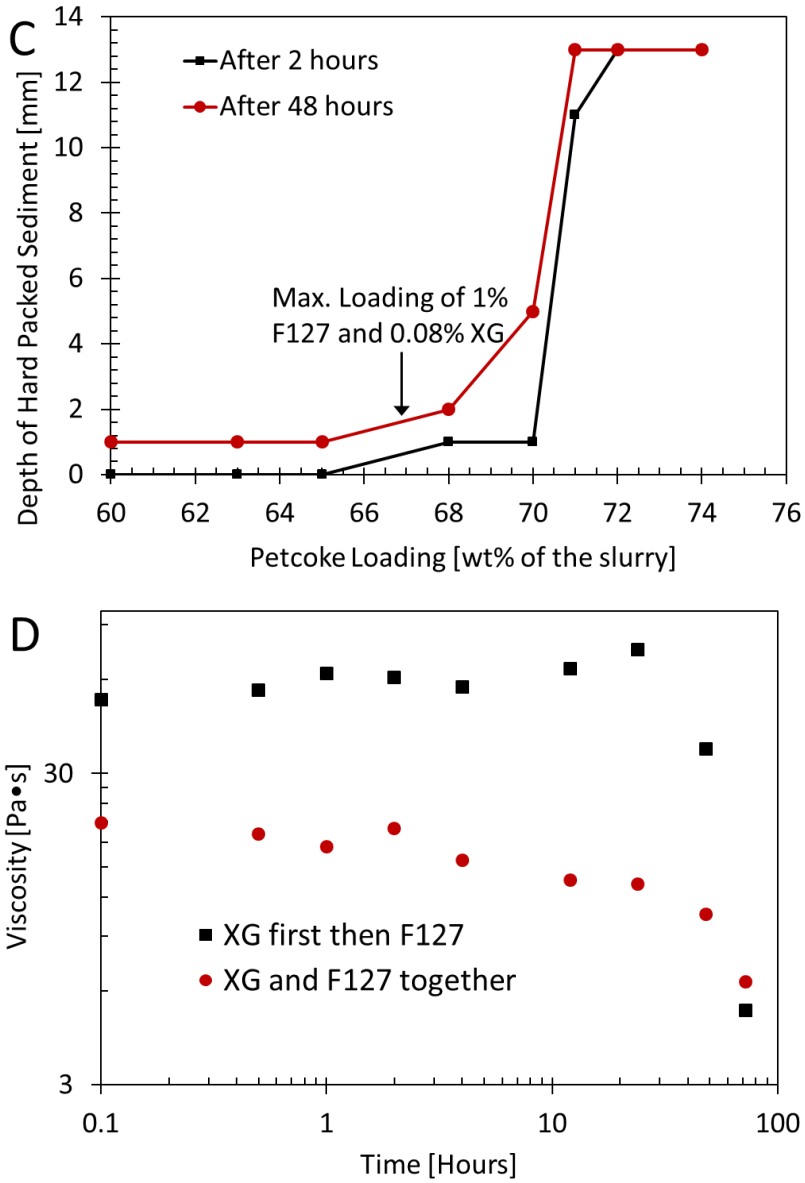

Fig. 6: a) The growth of hard packed sediment over time with increasing amounts of XG in 1wt% F127 60wt% petcoke slurries. The maximum depth of sediment was 13 mm. b) Compares viscosity vs. shear stress with the resulting stability from 6a). c) Effect on stability with increasing petcoke loading with 1wt% F127 and 0.08wt% XG added at the same time after 2 hours and 48 hours d) Time dependent rheology of 1wt% F127 0.08wt% XG 60wt% petcoke slurries measured at 0.1 Pa comparing the effect of XG adsorbing first then adding F127 vs. XG and F127 adsorbing at the same time.

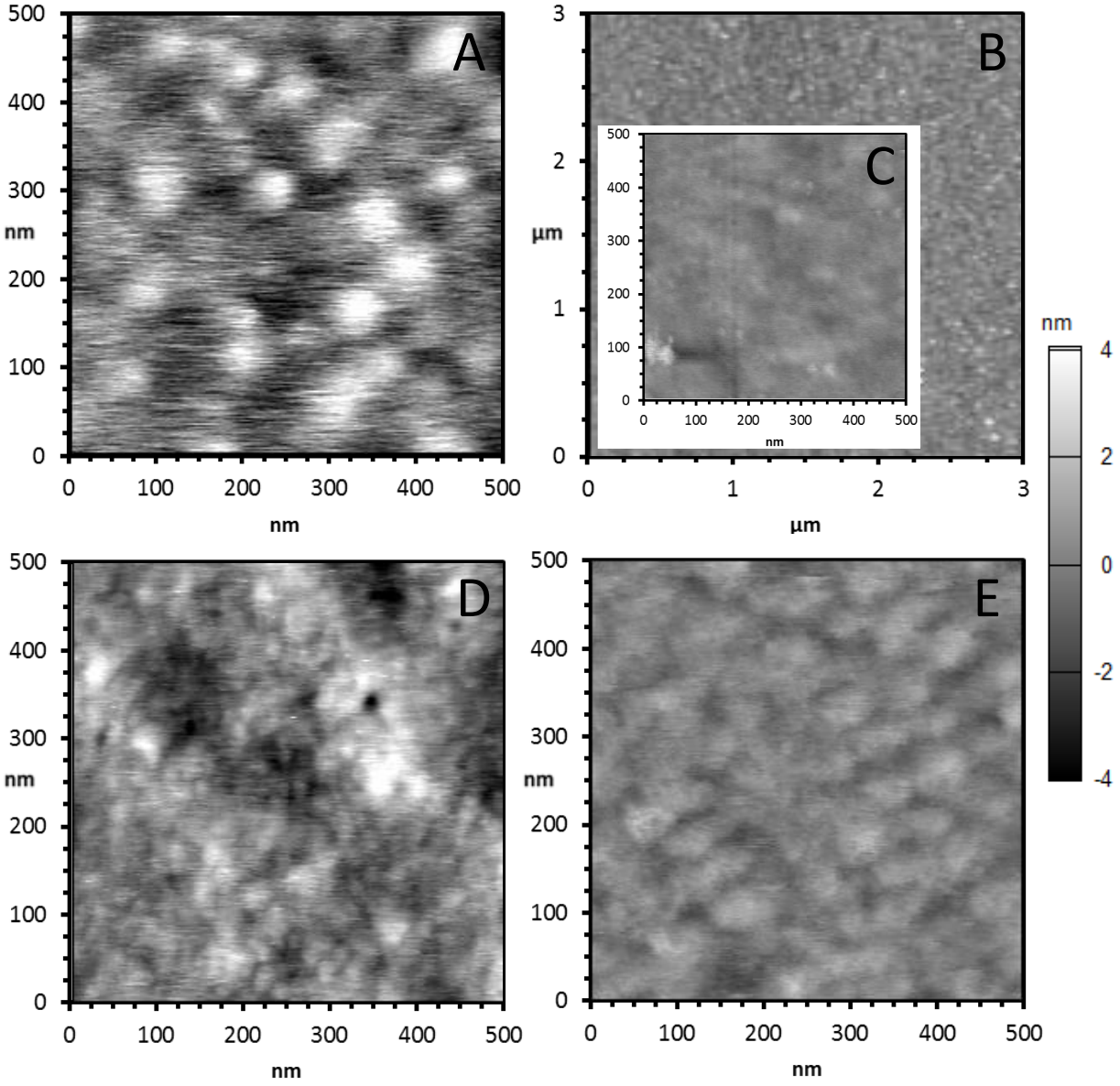

Fig. 7: AFM images of petcoke in solutions of a) 0.08% XG b,c)1% F127 0.08% XG d) 0.08% XG first then 1% F127 0.08% XG e) 1% F127 first then 1% F127 0.08% XG. The grayscale height scale is 8 nm.

From AFM images, XG is seen to create large uniform ~ 50 nm aggregates on the petcoke surface (Fig. 7a). When combined with F127 (Fig. 7b,c), the aggregates appear to be shorter and poorly defined, except for several small tall aggregates, perhaps due to a combination of partial coverage of the XG aggregate with F127 around its base and competitive adsorption with F127. When XG was allowed to adsorb first to the surface from a 0.08% XG solution

before F127 from a 1% F127 0.08% XG solution (Fig. 7d), XG aggregates are very tall and densely packed together although individual aggregates are smaller and less regular than in the case of XG only. F127 is thought to have broken the XG aggregates into smaller aggregates through competitive adsorption. When F127 was allowed to adsorb first (Fig. 7e), the XG aggregates are very wide, short, and less well defined compared to the previous case. In addition, there appears to be no small but tall aggregates like in the case where XG and F127 were added together. Adsorbing F127 first prevented any large, well defined aggregates from forming. Height profiles depicting the height of the aggregates more accurately are given in the supporting information. Competitive adsorption is further supported by Fig. 6d where over time the XG first and XG and F127 together samples decrease in viscosity. Presumably this is from F127 almost irreversibly replacing XG from the surface reducing the strength of the stabilization structure, a process that takes about 3 days. This may also be the main reason that the stabilized slurries settle which starts to occur at the same time as shown in Fig. 6a. A schematic of the XG and F127 system is presented in Fig. 8. Xanthan gum is believed to have a single or double helical semi-rigid rod secondary structure with disordered ends.[45-46] F127 is depicted in its brush form.

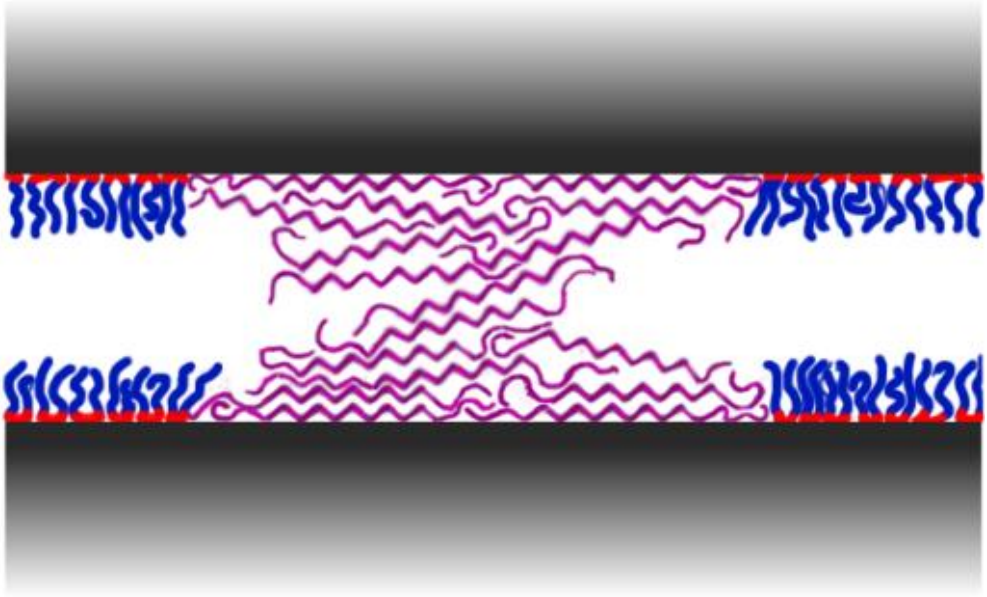

Fig. 8: A schematic representation of XG (purple) using flocculation stabilization to create a stabilizing network between two petcoke particle surfaces in conjunction with Pluronic (blue-PEO, red-PPO).

4. Conclusion

In literature, the slurrability of petcoke has been approximated as a high rank coal, and as such, anionic dispersants similar to typical coal dispersants have been used. However, since petcoke has less ash and volatile matter content which are known to add charge to the surface, anionic dispersants used with coal may not be optimal since the dispersant's charge prevents the adsorption of dense monolayers. After comparing the maximum petcoke loading for several anionic and nonionic dispersants, F127 was found to be superior by a significant margin. Slurry 1 vol% below its maximum petcoke loading for a particular dispersant was shown to exhibit similar rheological properties as slurries with different dispersants 1 vol% below their maximum loading making the comparison between dispersants simple. F127 was observed to have a minimum useful dispersant concentration of 0.25wt% which was shown to correspond to the completion of a strongly adsorbed monolayer through AFM and an adsorption isotherm.

Compared to other Pluronics, F127 is the most effective, presumably since it has one of the thickest adsorbed layers from the one of longest PEO blocks and a large PPO core. It is thought that Pluronics performed so well compared to other nonionic dispersants due to strength and density at which the Pluronics adsorbed to the uncharged hydrophobic surface to create a hydrophilic brush. Xanthan gum was shown to be an effective stabilizer at 0.08wt% with F127, especially when xanthan gum was added before the F127 but is competitively adsorbed off the surface over time.

Acknowledgement

The authors would like to acknowledge SK Innovation, the Cornell Center of Materials Research Shared Facilities (DMR-1120296), the National Science Foundation GK-12 Grass Roots Program (DGE-1045513) for funding and support.

Supporting Information

1. Additional Petroleum Coke Information

- **Origin:** North America
- **Heating Value**: 8456 Kcal/Kg (Dry basis)

  Test Method: ASTM D 5865

Table S1. Proximate analysis of petcoke used in the current study

Proximate Analysis	**Moisture**	**Volatile Matter**	**Fixed Carbon**	**Ash**	**Total**
	wt%	**wt%**	**wt%**	**wt%**	**wt%**
Petcoke	**0.73**	**12.33**	**86.38**	**0.58**	**100**

Table S2: Ultimate analysis of petcoke used in the current study

Atomic Analysis	**C**	**H**	**N**	**S**	**Total**
	wt%	**wt%**	**wt%**	**wt%**	**wt%**
Petcoke	**89.3**	**3.82**	**1.55**	**7.5**	**102**

- **Particle Size Distribution**

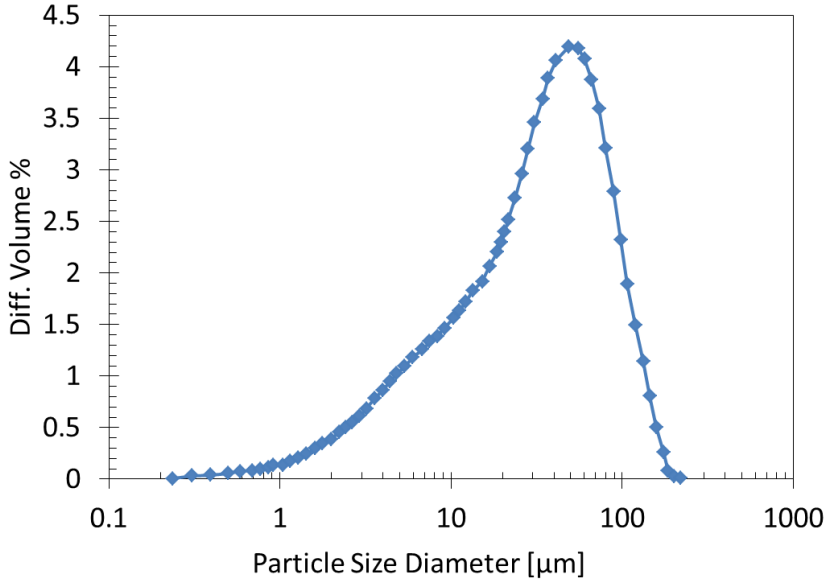

Figure S1 Differential volume % particle size distribution of petcoke particles which with d_{25}=35 µm, d_{50}=57 µm, d_{75}=84 µm, d_{90}=113 µm

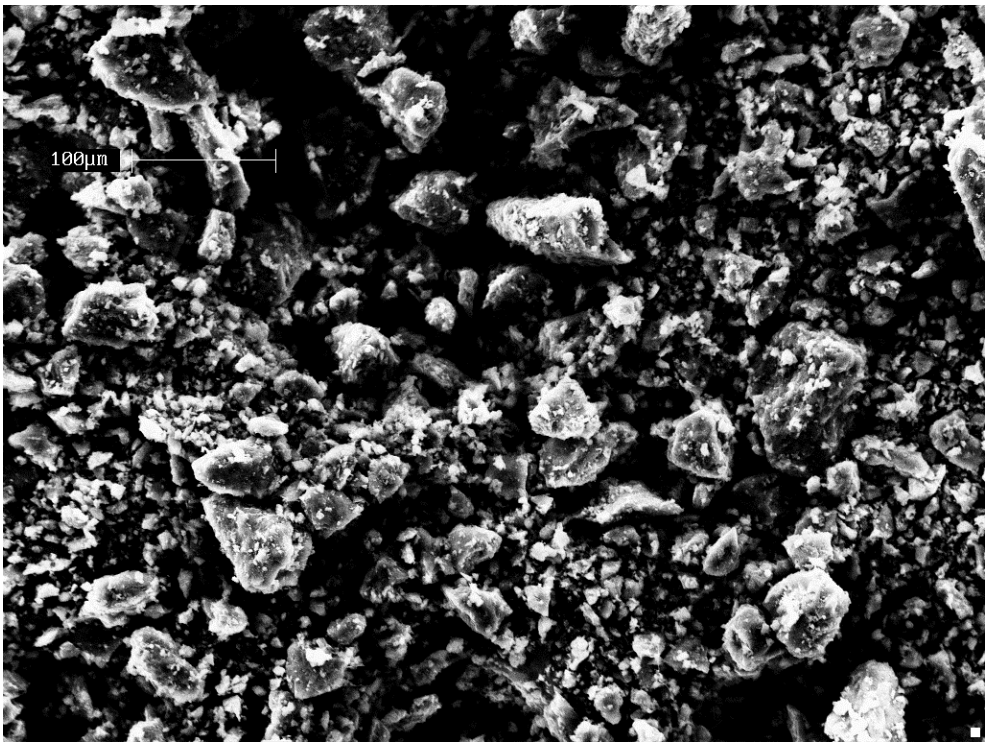

Figure S2 SEM image of petcoke particles

2. Additional Procedural Information

2.1 Preparation of Slurries for Rheological Measurements

Slurries were prepared to have a mass of 10 grams of deionized water (DI) and petcoke total. Polymer dispersants and xanthan gum (XG) did not contribute to this total and their weight percentages were based on the dry petcoke. For example, a 1% F127 0.08% XG 65% petcoke slurry would be made as: 6.5 g petcoke, 3.5 g DI, 0.065g F127, and 0.005g XG. A dry petcoke basis was used because the ratio of the dispersant to amount of petcoke the dispersant could cover seemed to be the most important aspect rather than the dispersant's concentration in the liquid before petcoke is added. Polymer dispersants and XG were dissolved/dispersed using a stir bar in the DI before the petcoke was added and the slurry was thoroughly mixed by gently stirring to prevent foaming. Before rheological tests were done, the slurry was allowed to sit for a half hour to fully adsorb the additives. Samples were always stirred just before use.

Slurries which had the XG added first were made by first dispersing the XG in 3g of DI, 1 g less than the total amount of DI that would be in the final slurry. The F127 was dissolved in remaining 1g of water in a separate vial. The full 6 g petcoke (60wt%) was added to the XG containing vial, thoroughly mixed, and was allowed to sit for 1 hour. Then the dissolved F127 was added and mixed.

Slurries that were prepared just below, at, or above the maximum loading were prepared by first finding the approximate maximum loading with a separate slurry sample. A 1% dispersant 74% petcoke slurry, which was above the maximum loading for any dispersant, was prepared and DI was slowly added and mixed in at 0.1 to 0.2g increments until a slow flow could be seen. Then several slurries around that concentration were made to confirm the visual observation with the rheometer for several samples.

2.2 Procedure for Rheometry Experiments

Rheological measurements were taken with a Physica MCR 300 rheometer with a 50 mm parallel plate at a 1mm gap. Low viscosity light mineral oil was used at the edges to prevent water evaporation. Ten seconds were allowed to reach equilibrium for every point measured. Ramps proceeded on a "points per a decade" fashion and ten points were taken per a decade. Each ramp took approximately 5 minutes. Approximately 4.5g of sample was used in each test.

Experiments which required shear rate ramps and shear stress ramps each had their own fresh sample placed on the rheometer. Shear rate ramps and shear stress ramps were immediately repeated on the same sample several times to obtain steady state responses. The second run of these ramps was reported as they were the most reproducible. Allowing up to 5 minutes between the first and second run for any structure broken down in the first run to potentially reform did not significant change the response in the second run. It was thought that if delicate XG structures which take a long time to reform were an issue that the stirring performed before placing the sample on the rheometer to disperse any sediment would disrupt them anyway. Also samples which can settle quickly showed less settling behavior when they were not allowed to rest.

2.3 Adsorption Isotherm

20wt% petcoke slurries with varying wt% F127 were made and were allowed to settle overnight. The liquid that could be easily poured off was filtered using a PTFE 0.2 μm VWR syringe filter and was massed. The syringe and syringe filter were rinse in a 1% F127 solution and then rinsed with DI water several times before their use. Solutions which do contain petcoke such as the 1% F127 solution contained the same initial F127 liquid concentration as a 60% petcoke slurry. From there the maximum mass of F127 that could be in the filtrate, assuming uniform F127 concentration, was calculated from the percent of filtrate which was recovered from the original slurry solution including the mass of the polymer. The filtrate was dried and the resulting Pluronic residue was massed. The fraction of the F127 mass not in the filtrate but could have been was assumed to have adsorbed to the petcoke, and this fraction was multiplied by total mass of F127 added to the original slurry to calculate the mass of F127 adsorbed. The mass adsorbed was then divided by the mass of petcoke in the slurry and the surface area of the petcoke. The BET surface area of the petcoke was measured to be $1.7 m^2/g$ in liquid nitrogen with a Gemini VII 2390t.

2.4 AFM Sample Preparation

Atomic force images (AFM) were taken with an Asylum MFP-3D in tapping mode using 100 μm silicon nitride cantilevers in deionized water at a frequency ~7kHz and an amplitude of

~1-3V. Petcoke was fixed to glass slides using epoxy and were allowed to equilibrate with the dispersant solution for 1 hour. The solutions were made like the solutions used for a 60% petcoke slurry except no petcoke was added.

To the make the 0.1% F127 solution used in the AFM, 0.1% F127 20% petcoke slurry was made with petcoke and allowed to equilibrate overnight. The liquid which was used in the AFM was then separated from the slurry using a PTFE 0.2 µm VWR syringe filter that was rinsed and washed with 1% F127 solution and DI water. The filtrate was used because at this concentration of F127 there is not enough F127 to cover all the surface area in the native slurry, though when there are only a few petcoke particles epoxied to a glass slide such as in the AFM sample, there is more than enough to cover every particle even with a low concentration standard solution made from directly dissolving 0.1% F127. To reproduce the concentration of F127 in the liquid phase after equilibrium is reached with the majority of petcoke particles in slurry, the liquid proportion of a 0.1% F127 slurry was used. This was not necessary at 1% since only a small fraction of the F127 in the slurry is actually adsorbed to the surface.

To create the sample with F127 first then XG, a standard 1% F127 solution was added to the slide and allowed to equilibrate. The F127solution was then poured off and rinsed with excess 1% F127 0.08% XG solution, and then the F127 + XG solution was added and allowed to equilibrate for 1 hour.

2.5 XPS and Contact Angle Measurements

X-ray photoelectron spectroscopy was performed with a Surface Science Instruments X-Probe SSX-100 by Cornell Center for Materials Research technical staff and the data was analyzed with CasaXPS. Contact angle measurements were taken with a Rame-Hart 500 goniometer and were analyzed with Image J. Powder samples are applied to painter's tape and the excess was shaken off. To find a clear baseline, powder was lightly scrapped near the drop. Multiple drops ~3 µL of deionized water were measured on petcoke and lignite and a single image was selected to show in section 4. A contact angle measurement was taken of the tape to show that the tape had little impact on the measured angle. Even with the tape, small amounts of powder did adhere to the surface of drop making some drops unsymmetrical towards

the bottom of the drop. Measurements were carried out the side of drop where the powder adhering to the drop was minimal.

3. Supplemental Results

3.1 XPS Analysis

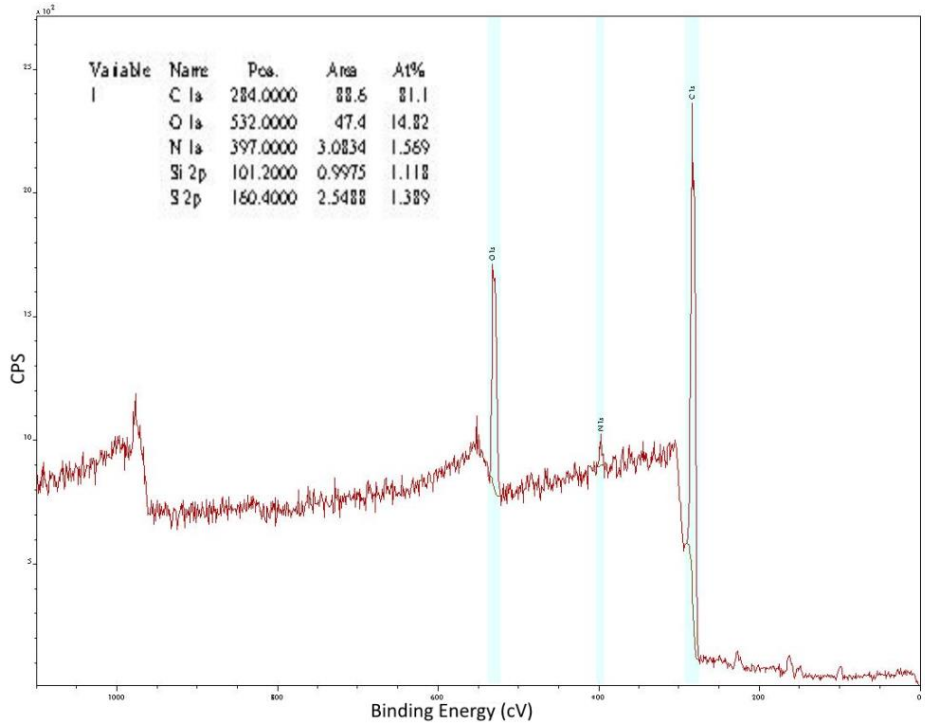

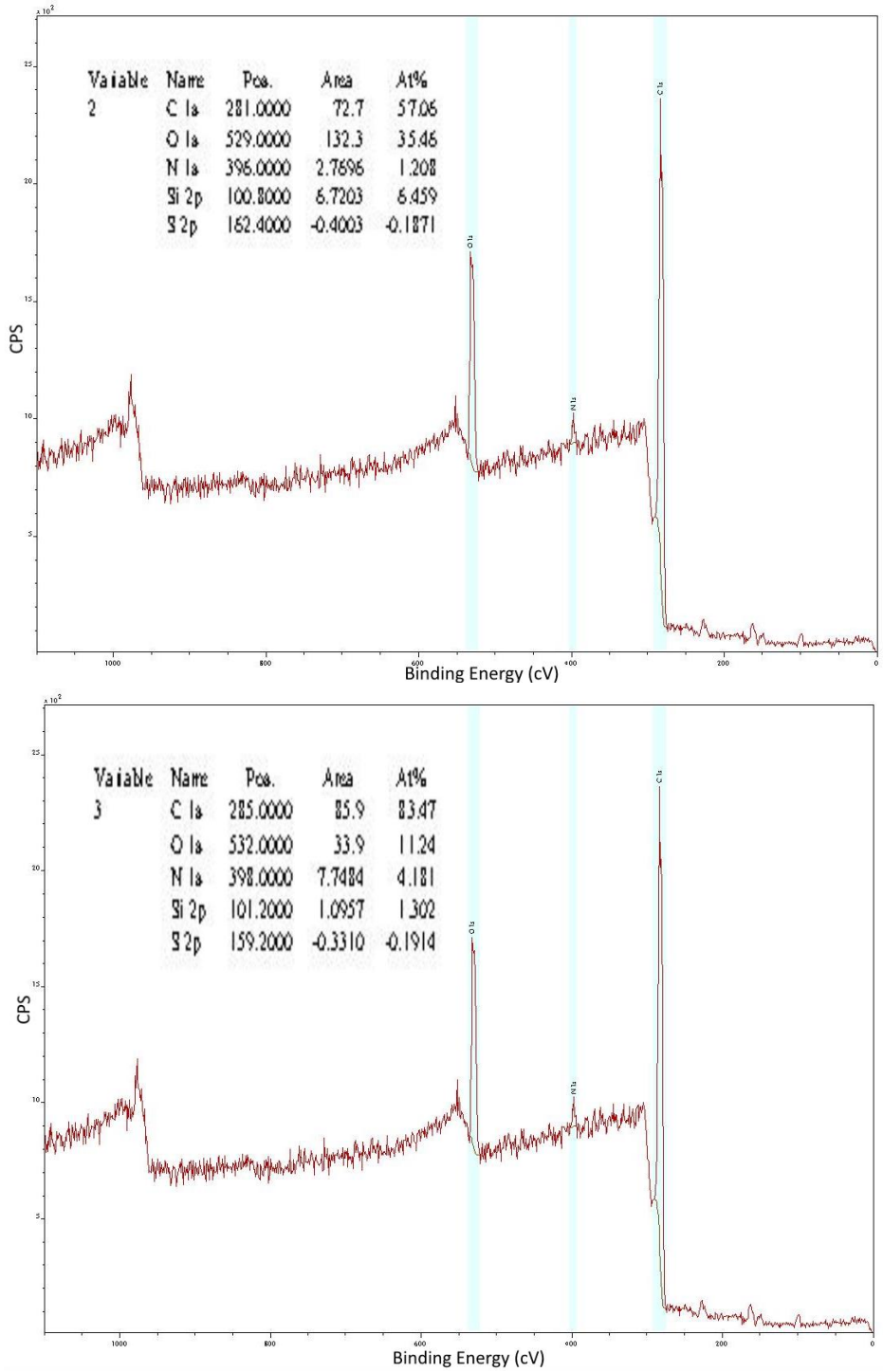

Figure S3 XPS results of three different carbon samples: a) petcoke, b) lignite, and c) carbonized PAN

3.2 Contact Angle Images

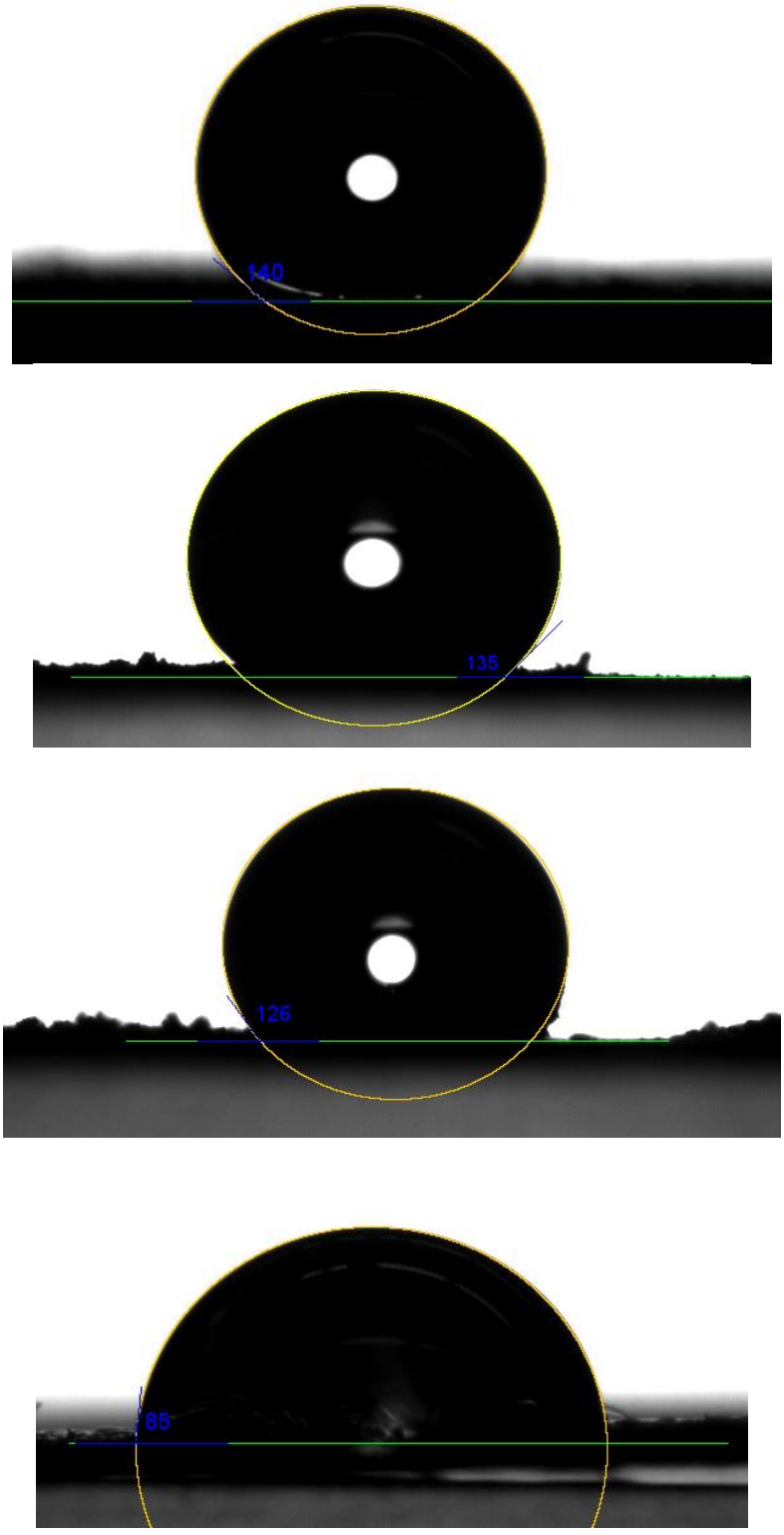

Figure S4 Contact angle measurements of a) petcoke, b) lignite, c) carbonized PAN, and d) supporting tape

3.3. Height Profiles of Adsorbed Petcoke Particle Surfaces via Atomic Force Microscopy

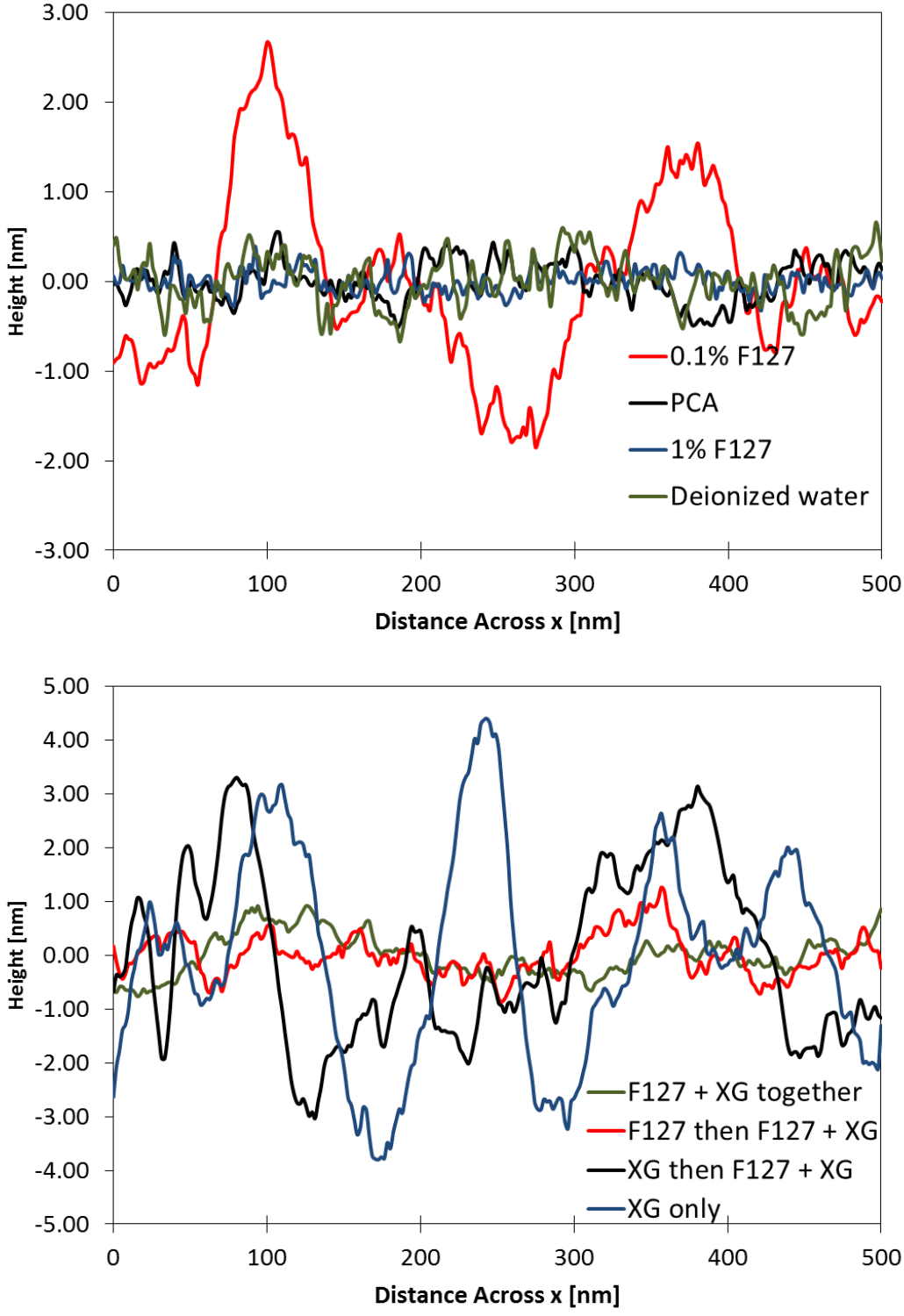

Figure S5. Height profiles of petcoke surface with a) adsorbed dispersant (F127 and PCA) and b) adsorbed dispersant (F127) and stabilizer (XG). These are the heights taken from a horizontal line across 300 nm from the 500 nm images.

REFERENCES

(1) Lee, S. H.; Yoon, S. J.; Ra, H. W.; Son, Y. Il; Hong, J. C.; Lee, J. G. Gasification Characteristics of Coke and Mixture with Coal in an Entrained-Flow Gasifier. *Energy* **2010**, *35*, 3239–3244.

(2) Zhan, X.; Zhou, Z.; Wang, F. Catalytic Effect of Black Liquor on the Gasification Reactivity of Petroleum Coke. *Appl. Energy* **2010**, *87*, 1710–1715.

(3) Murthy, B. N.; Sawarkar, A. N.; Deshmukh, N. a.; Mathew, T.; Joshi, J. B. Petroleum Coke Gasification: A Review. *Can. J. Chem. Eng.* **2014**, *92*, 441–468.

(4) U.S. Energy Information Administration, Dec. **2014**

(5) Gordon, Deborah. The Carbon Contained in Global Oils. *The Carnegie Papers.* **2012**

(6) Levinter, M.; Medvedeva, M. Mechanism of Coke Formation in the Cracking of Component Groups in Petroleum Residues. *Chem. Technol. Fuels Oils* **1966**, 628–632.

(7) Stockman, Lorne. *Petroleum Coke: The Coal Hiding in the Tar Sands*; Oil Change International: Washington DC; **2013**

(8) Fahim, M. A., Al-Sahhaf T.A., Elkilani, A.S. *Fundamentals of Petroleum Refining*; Elsevier: Oxford; **2010;** 1-9

(9) Lewis, I. CHEMISTRY OF CARBONIZATION. *Carbon.* **1982**, *20*, 519–529.

(10) Nexant, Inc., Global Energy Inc., Bechtel Corp. Gasification Plant Cost and Performance Optimization: Task 1 Topical Report IGCC Pant Cost Optimization; US Dept. of Energy National Energy Technology Laboratory Contract No. DE-AC26-99FT40342; 1; **2002**

(11) Philips, Jeffery. *Different Types of Gasifiers and Their Integration with Gas Turbines*; US Dept. of Energy *National Energy Technology Laboratory; **2006***

(12) Morel, William. *Economic Comparison of Coal Feeding Systems in Coal Gasification—Lock Hopper Vs Slurry*; US. Department of the Interior

(13) Zhan, X.; Zhou, Z.; Kang, W.; Wang, F. Promoted Slurryability of Petroleum Coke–water Slurry by Using Black Liquor as an Additive. *Fuel Process. Technol.* **2010**, *91*, 1256–1260.

(14) He, Q.; Wang, R.; Wang, W.; Xu, R.; Hu, B. Effect of Particle Size Distribution of Petroleum Coke on the Properties of Petroleum Coke–oil Slurry. *Fuel* **2011**, *90*, 2896–2901.

(15) Podolsak, A. K.; Tiu, C.; Saeki, T.; Usui, H. Rheological Properties and Some Applications for Rhamsan and Xanthan Gum Solutions. *Polym. Int.* **1996**, *40*, 155–167.

(16) Qiu, X.; Zhou, M.; Yang, D.; Lou, H.; Ouyang, X.; Pang, Y. Evaluation of Sulphonated Acetone–formaldehyde (SAF) Used in Coal Water Slurries Prepared from Different Coals. *Fuel* **2007**, *86*, 1439–1445.

(17) Pawlik, M. Polymeric Dispersants for Coal–water Slurries. *Colloids Surfaces A Physicochem. Eng. Asp.* **2005**, *266*, 82–90.
(18) Tsubaki, J.; Kato, M.; Miyazawa, M.; Kuma, T. The Effects of the Concentration of a Polymer Dispersant on Apparent Viscosity and Sedimentation Behavior of Dense Slurries. *Chem. Enginnering Sci.* **2001**, *56*, 3021–3026.
(19) Metzner, a. B. Rheology of Suspensions in Polymeric Liquids. *J. Rheol.* **1985**, *29*, 739-775.
(20) Klimpel, R. . The Selection of Wet Grinding Chemical Additives Based on Slurry Rheology Control. *Powder Technol.* **1999**, *105*, 430–435.
(21) Atesok, G.; Dincer, H.; Ozer, M.; Mutevellioglu, A. The Effects of Dispersants (PSS-NSF) Used in Coal-Water Slurries on the Grindability of Coals of Different Structures. *Fuel* **2005**, *84*, 801–808.
(22) Yoon, S. J.; Choi, Y.-C.; Lee, J.-G. The Effect of Additive Chemicals on the Viscosity of Coal-Petroleum Coke-Water Slurry Fuel for a Gasification Process. *Korean J. Chem. Eng.* **2010**, *26*, 1259–1264.
(23) Zhou, M.; Qiu, X.; Yang, D.; Lou, H.; Ouyang, X. High-Performance Dispersant of Coal–water Slurry Synthesized from Wheat Straw Alkali Lignin. *Fuel Process. Technol.* **2007**, *88*, 375–382.
(24) Xu, R.; He, Q.; Cai, J.; Pan, Y.; Shen, J.; Hu, B. Effects of Chemicals and Blending Petroleum Coke on the Properties of Low-Rank Indonesian Coal Water Mixtures. *Fuel Process. Technol.* **2008**, *89*, 249–253.
(25) Baker, J. A.; Berg, J. C. Investigation of the Adsorption Configuration of Poly (ethy1ene Oxide) and Its Copolymers with Poly (Propylene Oxide) on Model Polystyrene Latex Dispersions. **1988**, 1055–1061.
(26) Nejadnik, M.; Olsson, A. Adsorption of Pluronic F-127 on Surfaces with Different Hydrophobicities Probed by Quartz Crystal Microbalance with Dissipation. *Langmuir* **2009**, *25*, 6245–6249.
(27) Lin, Y.; Alexandridis, P. Temperature-Dependent Adsorption of Pluronic F127 Block Copolymers onto Carbon Black Particles Dispersed in Aqueous Media. *J. Phys. Chem. B* **2002**, *106*, 10834–10844.
(28) Dickinson, E. Hydrocolloids as Emulsifiers and Emulsion Stabilizers. *Food Hydrocoll.* **2009**, *23*, 1473–1482.
(29) Boylu, F.; Dinçer, H.; Ateşok, G. Effect of Coal Particle Size Distribution, Volume Fraction and Rank on the Rheology of Coal–water Slurries. *Fuel Process. Technol.* **2004**, *85*, 241–250.
(30) Vitolo, S.; Belli, R.; Mazzanti, M.; Quattroni, G.; Chimica, I.; Industriale, C.; Diotisalvi, V. Rheology of Coal-Water Mixtures Containing Petroleum Coke. *Fuel* **1996**, *75*, 259–261.
(31) Wildemuth, C. R.; Williams, M. C. Viscosity of Suspensions Modeled with a Shear-Dependent Maximum Packing Fraction. *Rheol. Acta* **1984**, *23*, 627–635.

(32) Malvern Instruments Limited. Overcoming and Quantifying 'Wall Slip' in Measurements made on a Rotational Rheometer. *Application Notes* **2014**

(33) Gadala-Maria, F.; Acrivos, A. Shear-Induced Structure in a Concentrated Suspension of Solid Spheres. *J. Rheol.* **1980**, *24*, 799.

(34) Wagner, N. J.; Brady, J. F. Shear Thickening in Colloidal Dispersions. *Phys. Today* **1999**, 27–32.

(35) Karatepe, N. Adsorption of a Non-Ionic Dispersant on Lignite Particle Surfaces. *Energy Convers. Manag.* **2003**, *44*, 1275–1284.

(36) Basova, Y. V.; Hatori, H.; Yamada, Y.; Miyashita, K. Effect of Oxidation–reduction Surface Treatment on the Electrochemical Behavior of PAN-Based Carbon Fibers. *Electrochem. commun.* **1999**, *1*, 540–544.

(37) Hamley, I. W.; Connell, S. D.; Collins, S. In Situ Atomic Force Microscopy Imaging of Adsorbed Block Copolymer Micelles. *Macromolecules* **2004**, *37*, 5337–5351.

(38) Brandani, P.; Stroeve, P. Adsorption and Desorption of PEO - PPO - PEO Triblock Copolymers on a Self-Assembled Hydrophobic Surface. *Macromolecules* **2003**, *36*, 9492–9501.

(39) Kim, Y.-H.; Kim, S.-K.; Park, J.-G.; Paik, U. Increase in the Adsorption Density of Anionic Molecules on Ceria for Defect-Free STI CMP. *J. Electrochem. Soc.* **2010**, *157*, H72.

(40) Amiji, M. M.; Park, K. Analysis on the Surface Adsorption of PEO/PPO/PEO Triblock Copolymers by Radiolabelling and Fluorescence Techniques. *J. Appl. Polym. Sci.* **1994**, *52*, 539–544.

(41) Li, J.-T.; Caldwell, K. D.; Rapoport, N. Surface Properties of Pluronic-Coated Polymeric Colloids. *Langmuir* **1994**, *10*, 4475–4482.

(42) Lee, J.; Martic, P. .; Tan, J. . Protein Adsorption on Pluronic Copolymer-Coated Polystyrene Particles. *J. Colloid Interface Sci.* **1989**, *131*, 252–266.

(43) Killmann, E.; Maier, H.; Baker, J. A. Hydrodynamic Layer Thicknesses of Various Adsorbed Polymers on Precipitated Silica and Polystyrene Latex. *Colloids and Surfaces* **1988**, *31*, 51–71.

(44) van den Boomgaard, T.; King, T. .; Tadros, T. .; Tang, H.; Vincent, B. The Influence of Temperature on the Adsorption and Adsorbed Layer Thickness of Various Molecular Weight Fractions of Poly(vinyl Alcohol) on Polystyrene Latex Particles. *J. Colloid Interface Sci.* **1978**, *66*, 68–76.

(45) Song, K.-W.; Kim, Y.-S.; Chang, G.-S. Rheology of Concentrated Xanthan Gum Solutions: Steady Shear Flow Behavior. *Fibers Polym.* **2006**, *7*, 129–138.

(46) Milas, M.; Reed, W.; Printz, S. Conformations and Flexibility of Native and Re-Natured Xanthan in Aqueous Solutions. *Int. J. Biol. …* **1996**, *18*, 211–221.

CHAPTER 3

Tunable Large Mesopores in Carbon Nanofiber Interlayers for High-Rate Lithium Sulfur Batteries

Brian P. Williams[1] and Yong Lak Joo[1,*]

[1] Robert Frederick Smith School of Chemical and Biomolecular Engineering, Cornell University, Ithaca, NY 14853 USA

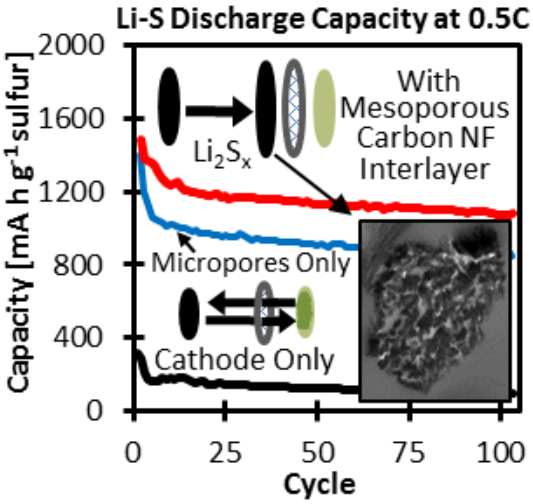

Abstract

Lithium sulfur battery interlayers were made from mesoporous carbon nanofibers with large tunable mesopores (17-50+ nm). The nanofibers were prepared by blending and electrospinning two immiscible polymers, polyacrylonitrile (PAN) and cellulose diacetate (CDA) with dimethylformamide as the solvent. Humidity control during the electrospinning process made adjustments to the size of the meso- scaled phase separation domains of the sacrificial CDA. The resultant fiber mat was carbonized and activated in air to create micropores in mesoporous carbon nanofibers (MPCNF). The pore characteristics of the activated MPCNFs were examined and then tested as interlayers in Li-sulfur batteries. First, a fundamental study

was conducted regarding the effectiveness of the interlayer versus its own weight and the overall sulfur composition along with a characterization of the pore filling and impedance. Secondly, the effect of micropores and three different pore widths of large mesopores in interlayers on battery performance was studied which revealed that the largest mesopores played a critical role in improving rate capability. Cells with MPCNF interlayers with 50+ nm pores and 70:30 sulfur:Super P composite cathodes had a discharge capacity of over ~1100mAh g^{-1} sulfur for 100 cycles at 0.5C and exhibited improved high charge rate capabilities with 850mAh g^{-1} at 3C.

1. Introduction

Mesoporous (2-50nm) carbons have been heavily studied for many applications including water purification, catalysis, molecular sieves, biomolecule adsorption, and energy storage because they can provide a relatively chemically inert, robust, conductive support with a balance of high surface and pores wide enough for quick diffusion.[1-3] For battery applications, a particular pore distribution may be desired over another to fit the exact diffusion needs of a particular electrolyte or the storage of a particular reaction product.[4-6]

In a lithium sulfur battery, unreacted sulfur is stored on a carbon cathode and is lithiated into lithium polysulfides (Li_2S_x, $8 \geq x \geq 2$) and then, ideally, fully lithiated into lithium sulfide (Li_2S) on the cathode.[7-15] Lithium polysulfides greater than Li_2S_2 are well known to be soluble in the commonly used electrolytes in lithium sulfur batteries.[7-15] Micropores or small mesopores are essential to carbon-based sulfur cathodes in organic electrolyte to resist and adsorb the dissolved lithium polysulfides from diffusing out of the cathode and to the anode.[7-8,10-11,13-18] At the anode, migrating polysulfides form an insoluble insulating lithium sulfide layer and contribute to the lithium polysulfide shuttle mechanism causing polarization and self-discharge throughout the

cell described in more detail elsewhere.[7,13-15,18-21] Previous works have found that ordered mesoporous carbons have been effective as cathodes as the mesopores offer a balance of surface area to provide diffusion retarding intermolecular forces and short electron diffusion distances to the polysulfides as well as large pore volumes for product storage and electrolyte diffusion.[6,8-10,13,15,18,22-24]

Over the past four years, carbon based interlayers and related structures such as sandwiches or carbon coated separators with graphene, carbon nanotubes, activated carbon, mesoporous carbons, ordered hierarchical carbons, carbon blacks, and biomass based carbons have been shown to improve lithium sulfur capacity in several works.[13-15,20,25-43] Placed between the cathode and the separator, an interlayer is thought to act like a filter for dissolved polysulfides diffusing their way towards the anode and a second current collector in the cathode. In this setup, the majority of the sulfur should be kept in the cathode. However, some diffusion of polysulfides is inevitable even for the most well-made carbon cathodes,[7,14] especially during the first cycle when it is thought that poorly adsorbed polysulfides such as those on a nonporous exterior surface are allowed to migrate.[23] An ideal interlayer would adsorb and trap all polysulfides before they reached the anode. Like the cathode, the interlayer should have a strong affinity for polysulfides and sulfur which has been studied recently by increasing the amount of nitrogen on the surface to improve sulfur and polysulfide adsorption.[43-45] It also has been shown that mesopores and micropores are needed in interlayers for fast diffusion, high surface, and large volumes for lithium sulfide storage.[8-11,13-15,17-19,22,46] Also like a cathode, the interlayer should be conductive so sulfur adsorbed in the interlayer is not wasted in future cycles. Unlike cathodes, interlayers must be a dense enough filter to capture polysulfide but be highly porous as to not block ion access to the cathode.[14] An interlayer should also have its own structural

integrity so it may be stacked on the cathode easily.[13-15] Finally, when combined with a next generation cathode or a simple bulk activated carbon cathode, it is desired that the interlayer will greatly extend the capacity retention of the cell despite being a simple addition.

Previous works on lithium sulfur cathodes have made carbons of all morphologies and pore distributions but tend to rely on a time consuming, hard templating process with silica or a soft templating process that mainly produces thin films with expensive block copolymers or toxic precursors which limits the commercial viability of these carbons.[1,3,13,47] In this work, mesopores are templated by the phase separation of two relatively inexpensive immiscible polymers from a blended homogenous solution of polyacrylonitrile (PAN) and cellulose diacetate (CDA). After mixing, the solution is electrospun into nanofibers where microphase separation occurs. The rapid solvent evaporation during electrospinning and the physical constraints of being stretched into a nanofiber freezes the phase separation into meso- scaled domains within the fiber.[48] With heat treatment and carbonization, the PAN component of the fiber is converted to carbon while the sacrificial CDA component is pryolyzed leaving behind a pore. Several works have created mesoporous nanofibers by a similar electrospinning method for a variety of purposes including interlayers.[32,49-51] Pores made using this approach can be larger (>10nm) than the typical smaller mesopores created from templating (2-10nm).[42]

Even though there are many similarities between cathodes and interlayers, they do not have the same optimal pore distribution. Micropores and small mesopores are desired in a cathode because when the sulfur is loaded, small pores ensure all the sulfur is well adsorbed. However with interlayers, the sulfur is slowly loaded by diffusion until its surfaces are covered so smaller mesopores may not be optimal or necessary, especially at high charge rates. Several successful studies with carbon interlayers have contained mesopores larger than those typical

used in cathodes but were still below 15nm.[29,32-34] A study by J. Song *et al.*[30] achieved both great capacity retention and rate capability with very large mesopores (~45nm). The study achieved ~1000 mAh g^{-1} after a 150 cycles at 0.5C and a high sulfur loading of 4 mg S cm^{-2} and ~950 mAh g^{-1} at 2C and a lower sulfur loading using a Ketjen carbon black interlayer-sandwich structure. From these findings it was desired to investigate how varying the size of large mesopores (10-50nm) can affect the rate performance and capacity retention of an interlayer system as this was not the focus of the previous study or other studies.

In this work, by changing the humidity during the electrospinning process, the average size of the mesopore was adjusted between 17 and 50+ nm to study the effect of mesopore size and microporosity on interlayer performance. Compared to previous works, we find that large mesopores (>15nm) contribute substantially to the rate capability of the battery with little to no loss to capacity retention compared to smaller mesopores. We also demonstrate through a systemic study considering the mass, impedance, surface area, appearance, and cathode material of the interlayer cell that interlayers benefit lithium sulfur batteries by a filtering mechanism and that the benefit of the filtering effect is beyond the effect of lowering the overall sulfur loading from the additional mass of the interlayer, suggesting a potentially scalable process.

2. Materials and Methods

2.1 Tunable Mesoporous Carbon Nanofibers

Polyacrylonitrile (PAN) (M_w=150,000 from Sigma Aldrich) and cellulose diacetate (CDA) (M_n= 50,000, 39.7% acetyl from Sigma Aldrich) was dissolved in dimethylformamide (DMF) to 12.9wt% polymer in a 1:1 ratio of PAN to CDA. The solution was vortexed until fully mixed, and was electrospun immediately at 19kV, 20 cm distance to the collector, and a

0.02mL/min polymer flowrate with an 18 gauge stainless steel needle. More details of the basic setup and theory of electrospinning are discussed elsewhere.[52] The eletrospinning process took place in a humidity controlled box which was necessary for consistency with PAN dissolved in DMF since water is a powerful antisolvent for PAN in DMF.[53] Control of the humidity was also the mechanism to make adjustments to the size of the mesopores.

The spun nanofibers were peeled from the collector and heat treated in air between two ceramic plates at 270°C for 1 hr with a ramp rate of 1°C/min to stabilize the PAN component of the fibers. The fibers were then placed in a nitrogen filled tube furnace at 1000°C for 8 hours with a ramp rate of 10°C/min to carbonize the PAN component and remove the CDA component by thermal degradation to create mesoporous carbon nanofibers (MPCNF). The process and theory of creating PAN based fibers and nanofibers is discussed in more detail in other literature works.[31-32,49,54] Macropores through the nanofiber mat exist naturally as the micron sized spaces between the fibers. Micropores were added to the fibers by heat treatment in air at 350°C for four hours for all fibers tested unless noted. Approximately ~5% burn off was achieved to complete the hierarchical pore system with the micropores. CDA was chosen as the sacrificial component compared to previous works with porous PAN based carbon fibers using polymers such as poly(methyl methacrylate),[10] polyvinylpyrrolidone,[50] or polystyrene[55] because the high melting point (~260°C) of CDA is thought to better preserve the large mesopores during PAN stabilization but still thermally degrade to a low yield at higher temperatures. Nafion was not chosen due the expense of Nafion and only <15nm pores were produced in a previous work.[32] The plates were necessary to prevent curling of the fiber mat during stabilization, and the carbonization treatment was done for eight hours to improve conductivity.

The surface area and pore size distribution analysis was performed on a Micromeritics Gemini VII 2390t in liquid nitrogen with the Brunauer, Emmett and Teller (BET), t-plot, and Barrett-Joyner-Halenda (BJH) methods. Interlayers were washed in deionized water three times with overnight soaks each time. Samples were degassed under nitrogen at 300°C for at least 3 hours. Transmission electron microscope (TEM) images were taken on a Tecnai FEI T12 TEM at 120kV. The samples were embedded in epoxy resin from Electron Microscopy Sciences and microtomed into 100-150 nm sections with a diamond knife for the images. Before embedding interlayers were washed 3 times soaking overnight each time in the electrolyte solvents made from a 1:1 volume ratio of 1,2 dimethoxyethane (DME) and 1,3 dioxolane (DOL) unless noted otherwise. The scanning electron microscope (SEM) image was taken by a Tescan Mira3 Field Emission SEM.

2.2 Battery Testing

Interlayers were punched out from the fiber mat to a 19mm diameter disc and were placed between the cathode and a 25 micron thick Celgard PE separator in a 2032 CR coin cell. Unless stated, the interlayers were between 18mg-19mg (~6.5mg cm^{-2}, ~300µm thick) and were spun at 30% relative humidity (RH) at room temperature. The cathode material contained 90wt% sulfur/carbon composite material and 10wt% poly(vinylidene fluoride) (Mw=534,000 from Sigma Aldrich) binder. The default composite material contained 70% sublimed sulfur from Spectrum Chemical and 30% Super P (conductive carbon black additive from TIMCAL). The sulfur was incorporated into the Super P by melting at 140°C for 12 hrs and vaporizing the excess at 230°C for 1 hr in a closed vessel. The cathode composite material and binder was mixed and suspended in slurry in 1-methyl-2-pyrrolidone (NMP) with at least one hour of

sonication to disperse the Super P. The solvent to Super P ratio was approximately 0.15g Super P to 6g NMP. The slurry was then cast upon to battery grade aluminum foil, spread out with a doctor blade to 25 microns and was allowed to dry. After the active material coating, the foil was punched into a 15mm diameter disc for the 2032 CR coin cell and contained on average ~1.8 mg of sulfur. Cathodes which contained other composite materials were 10% Super P, 20% activated carbon or ground MPCNF, and 70% sulfur. 9% sulfur cathodes were 10% Super P, 81% carbon material, and 9% sulfur. The activated carbon was Norit GSX steam activated acid washed carbon powder. The ground MPCNF powder used in select cathodes was ground in a MTI ball mill for at least a half hour. The anode was 0.25 mm thick lithium metal foil from MTI Corporation and was lightly sanded right before assembly to remove any surface oxides. The electrolyte was 1 M bis(trifluoromethane)sulfonimide lithium salt and 0.1 M lithium nitrate in a 1:1 volume ratio of DME and DOL, all purchased from Sigma Aldrich. This electrolyte was used for all cells unless noted otherwise. The coin cells were assembled in a dry, oxygen-free (1 ppm) argon filled glovebox.

The battery testing was conducted on analyzers from MTI Corporation with 1 mA and 10 mA current maximums at constant current depending on the mass of the battery made. The charge rate (3C, 2C, 1C, 0.5C, 0.25C) is based on the current to charge the theoretical capacity of 1 gram of sulfur in a battery in one hour (1C = 1675mA/g). All of the reported capacities are based on their discharge capacities. The batteries were cycled between the voltage window of 2.8V and 1.7V. The electrochemical impedance spectroscopy (EIS) was conducted with a Princeton Parastat 4000 from ~100kHz to 1 Hz with a 5mV amplitude. For EIS measurements, coin cell batteries were cycled for 10 cycles to their charged state. Cyclic voltammetry (CV) was carried out on the same equipment and the coin cells were cycled from 2.8V to 1.7V vs. lithium

at 0.2mV/sec for five cycles using the same 18mg 30% RH interlayer and 70:30 S:Super P composite material cathode as above.

3. Results and Discussion

3.1 Effectiveness of the Interlayer

By placing a MPCNF interlayer into a lithium-sulfur coin cell battery between the cathode and separator, a stark improvement of ~900mA h g^{-1} is observed in the discharge capacity performance between cells with an interlayer and without an interlayer. (Figure 1a) In Figure 1b, the 1st cycle of the cell with an interlayer shows capacity beyond the theoretical capacity of 1675mAh g^{-1} sulfur. The discharge curve without an interlayer in Figure 1c contains a plateau at 2.3V and at 2.1V corresponding to the high order polysulfides and lower order polysulfides reactions respectfully as discussed in literature.[7,13-15,18] However, when Figure 1b is compared to Figure 1c, it is apparent that the excess capacity is related to an irreversible reaction with the carbon interlayer and predominately occurs in the first cycle. This extra plateau at ~1.85V may be the bulk decomposition of the lithium nitrate in the electrolyte, which has been reported to react at voltages as high as 1.9V with activated carbon.[56] In Figure 1d, an interlayer is used in both cells but one does not contain lithium nitrate in the electrolyte. Without lithium nitrate, the plateau at 1.85V disappears and the discharge capacity is below the theoretical limit supporting that the lithium nitrate added the capacity from decomposition with the interlayer. CV testing also supports this in Figure 1e showing the fifth cycle for with and without an interlayer. Without an interlayer, weak peaks are visible for each plateau in Figure 1c. However with an interlayer, the beginning of additional peak is visible at 1.7V, and since in CV testing the majority of the lithium nitrate would not degrade in a single cycle and was still present in the fifth cycle, a single peak for the charge is observed like in the first cycle charge of Figure 1b.

In Figure 1f, the discharge curves of the 10th cycle for cells with and without interlayers are compared. The instantaneous capacity, as depicted in Figures 1b) and 1c), was normalized by dividing the instantaneous capacity by the total capacity for that cycle with a 1.7V cutoff. With the interlayer, the discharge current operates at predominately higher voltages producing more power but has a longer tail near the end of the discharge. At 0.25 C the capacity loss with the baseline micro- and mesoporous interlayer was 5.2mA h g^{-1}/cycle or 0.34%/cycle and has similar performance to previous interlayers.[13]

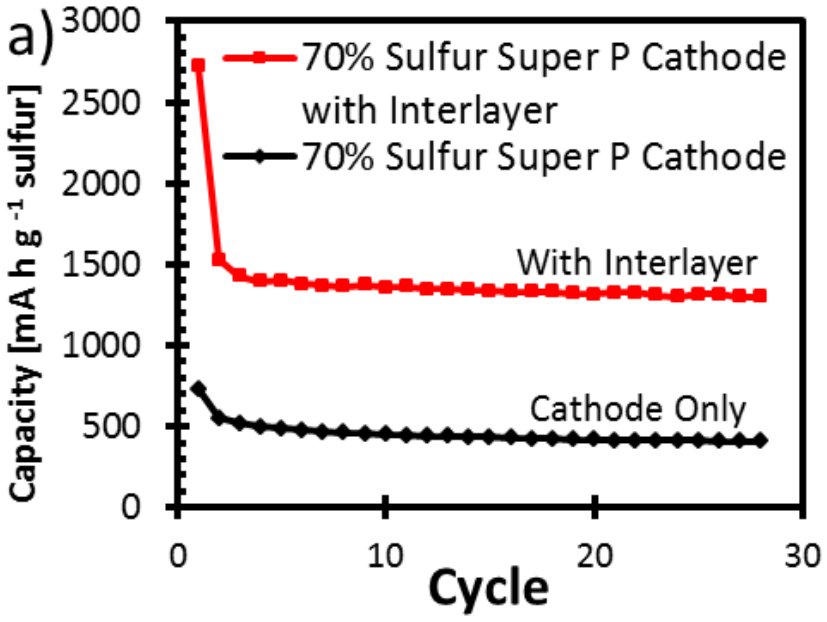

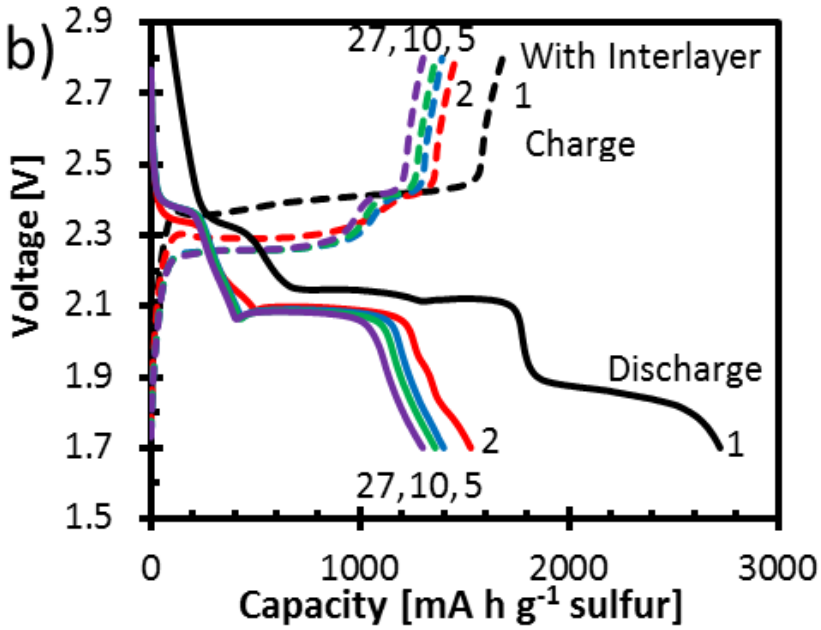
b)
Voltage [V]
2.9
2.7
2.5
2.3
2.1
1.9
1.7
1.5
27,10,5
2
1
With Interlayer
Charge
Discharge
2
1
27,10,5
0
1000
2000
3000
Capacity [mA h g-1 sulfur]

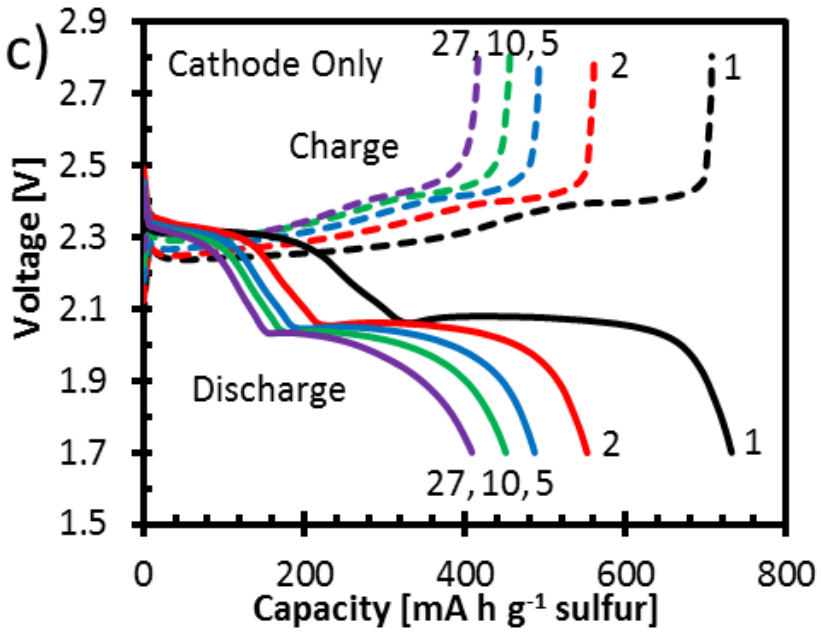
c)
Voltage [V]
2.9
2.7
2.5
2.3
2.1
1.9
1.7
1.5
Cathode Only
27,10,5
2
1
Charge
Discharge
2
1
27,10,5
0
200
400
600
800
Capacity [mA h g-1 sulfur]

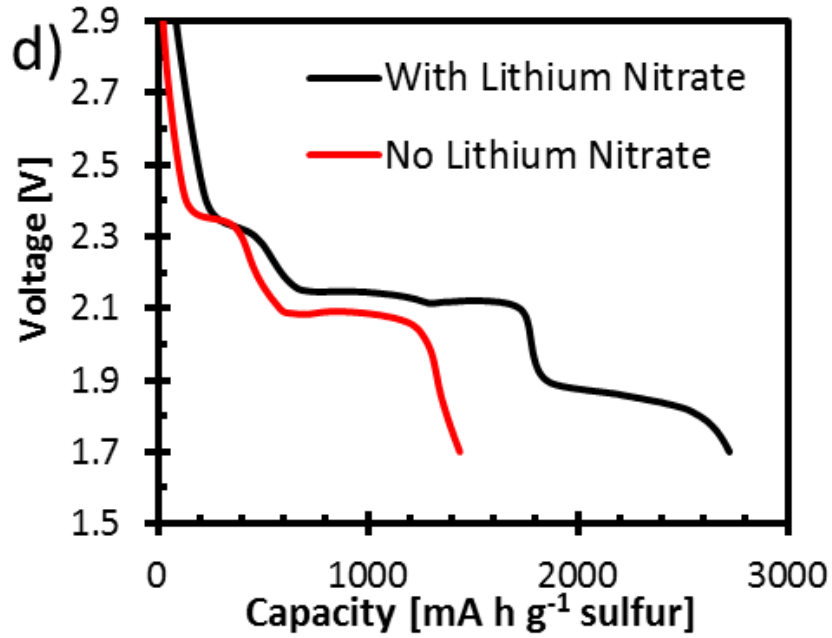
d)
With Lithium Nitrate
No Lithium Nitrate
Voltage [V]
2.9
2.7
2.5
2.3
2.1
1.9
1.7
1.5
0
1000
2000
3000
Capacity [mA h g-1 sulfur]

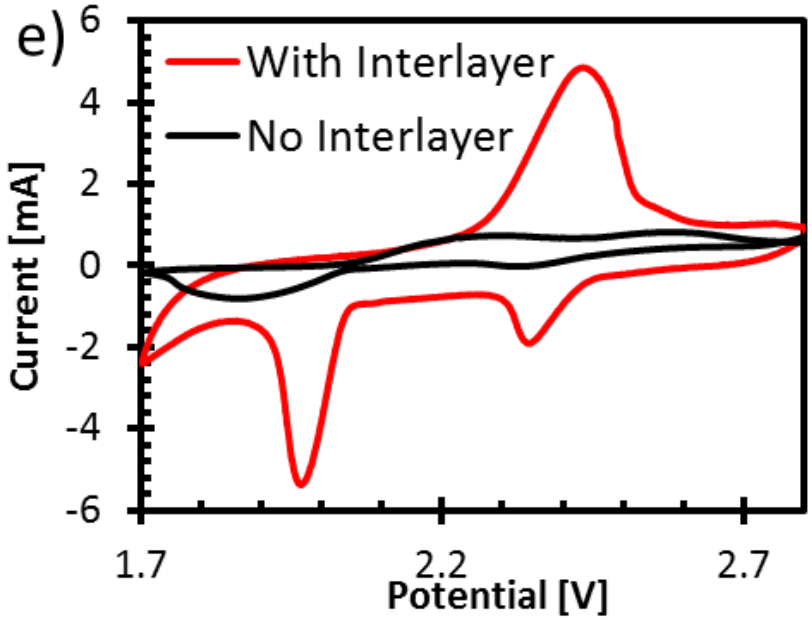
e)
With Interlayer
No Interlayer
Current [mA]
6
4
2
0
-2
-4
-6
1.7
2.2
2.7
Potential [V]

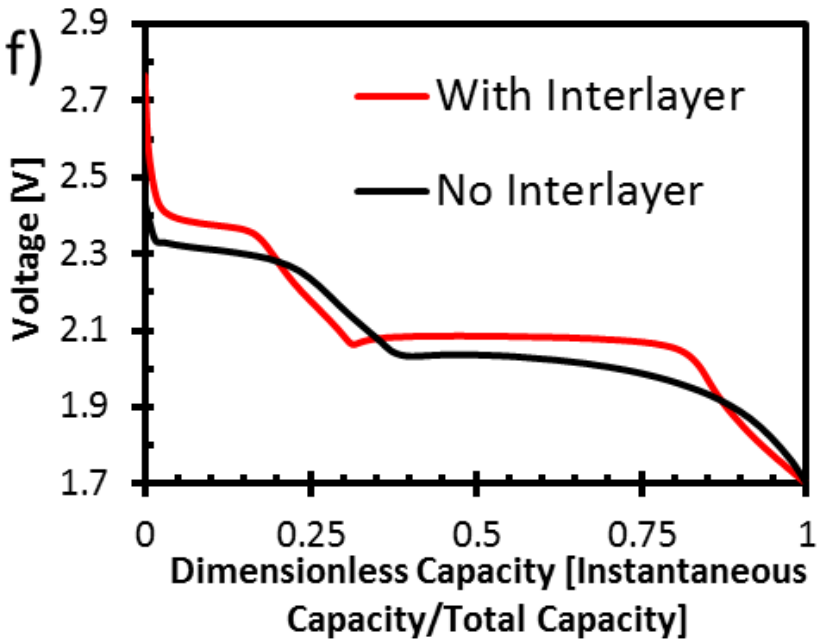

Figure 1: a) Specific discharge capacity performance of a lithium sulfur coin cell with an 18mg MPCNF interlayer vs. no interlayer for 28 cycles at 0.25C. b) Discharge-charge curves for cycles 1, 2, 5, 10, and 27 for the cell with an interlayer and c) without an interlayer. d) Comparison of the first discharge of with and without lithium nitrate in the electrolyte. e) Cyclic voltammograms from 2.8V to 1.7V vs. lithium at 0.2 mV/sec to compare cells with and without an interlayer by showing the fifth cycle. f) Comparison of the discharge curve with an interlayer and with no interlayer from the tenth cycle with a dimensionless capacity.

3.2 Effect of Pores and Pore Size

Next, the size of the mesopores and the presence of micropores were examined against capacity performance. By adjusting the humidity during the initial electrospinning of the nanofibers, the peak mesopore diameter was tunable between 17 and 50 nm as shown in Figure 2a-b with incremental area and volume. Without the sacrificial component, pure PAN did not produce significant amounts of large mesopores. The small mesopores (<10nm) that were measured for all the samples were predominately from activation. It is thought that the higher humidity created larger mesopores because the small increase of water absorption from the

higher humidity caused quicker solidification of the fibers near the surface resulting in thicker fibers as observed through SEM and TEM. Thicker fibers however slowed down the evaporation of DMF in the inner part of the fiber, which allowed more amount time for phase separation to occur within the fiber before complete solidification, creating larger pores after carbonization and activation. The mesopores are not thought to be created by the humidity like in previous works where water or another anti-solvent was added to the polymer solution to create mesopores or else the PAN only fibers would have shown more mesopores as well, since they were also spun at 30% RH.[3,53,57-58]

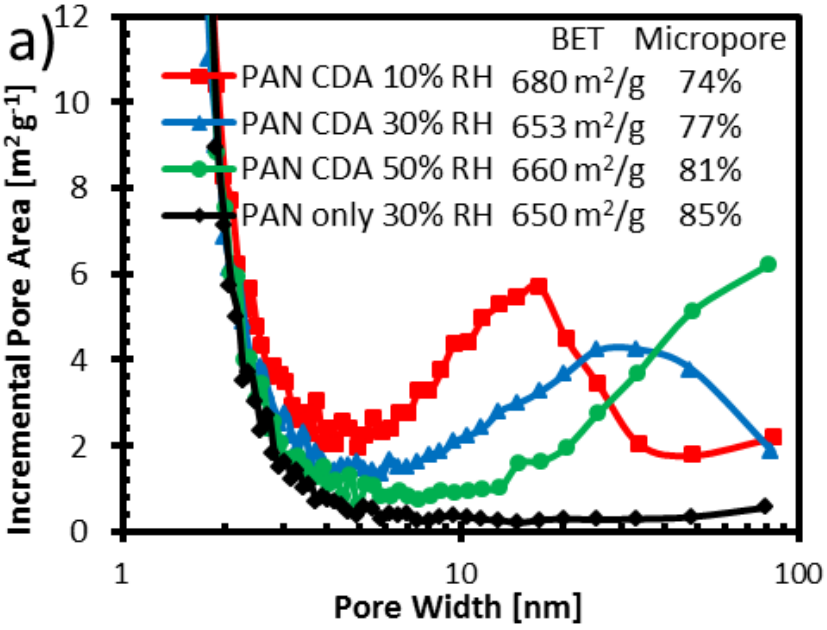

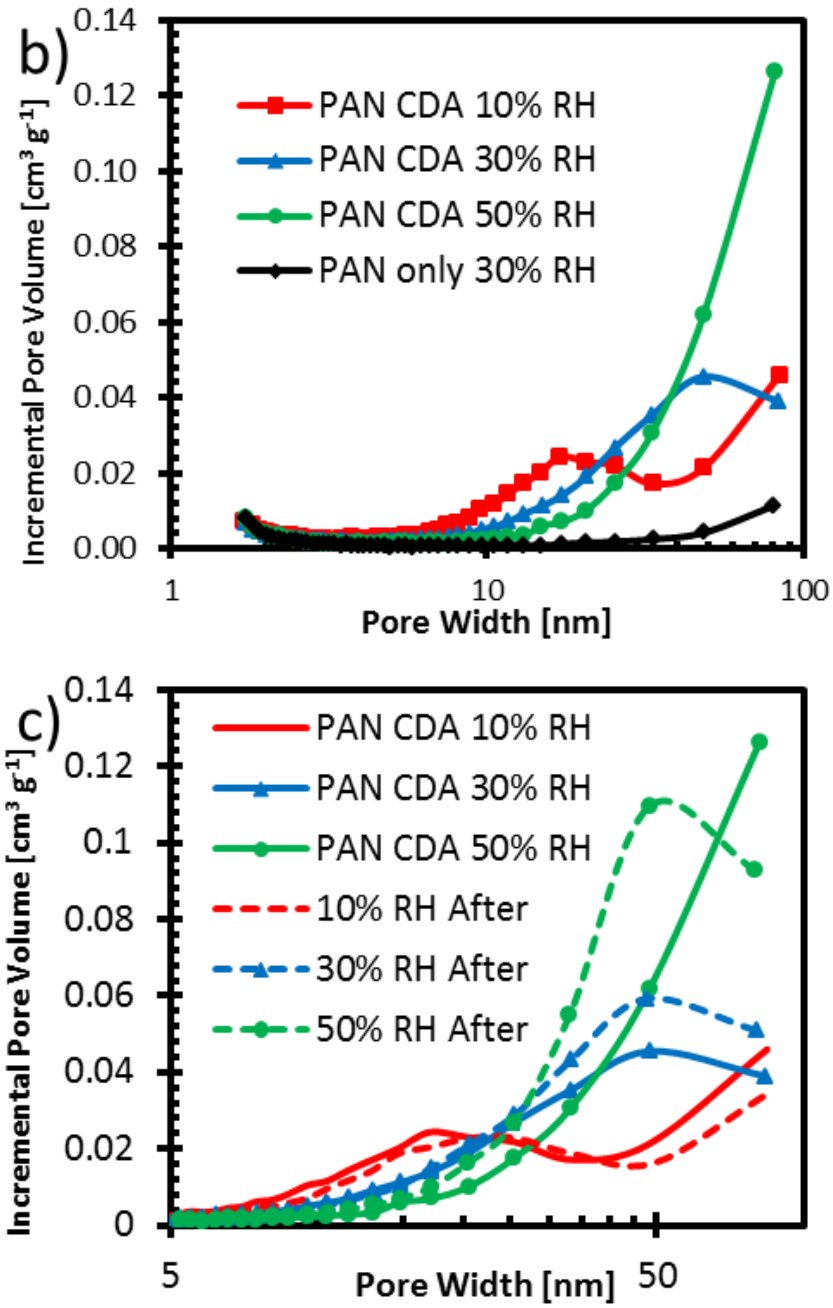

Figure 2: a) Incremental pore area distribution following the BJH method with nitrogen physisorption of four carbonized and activated samples initially electrospun at different relative humidities (RH). The first three samples are 1:1 blends of PAN and CDA and the fourth is PAN only. b) the incremental pore volume distribution of a). c) Includes the incremental pore volume distribution after 28 cycles and washing in DI water.

TEM images of the cross and longitudinal sections of the microtomed carbonized and activated nanofibers are shown in Figure 3. From the cross sections 3a), c), and e), the pores are

irregular as expected. The interconnectivity of the pores seems to increase with increasing pore size. From the longitudinal sections in 3b), d), and f) pores appear to be aligned with the axis of the nanofiber and that few pores lead to the surface, especially for 10% RH. However, since the pores were measurable from nitrogen physisorption, they must be accessible to at least nitrogen gas, though perhaps only through a tortious path requiring diffusion in both the radial and axial directions to find interconnections to the inner pores. The TEM images of the PAN only fibers also show no mesopores like the BJH analysis did. From the SEM images (Figure 4) the pores for PAN CDA samples appear to break through the surface occasionally at the rough regions of the fiber. Breaks to the surface seem more common for the 30% and 50% RH fibers than the 10% RH fibers.

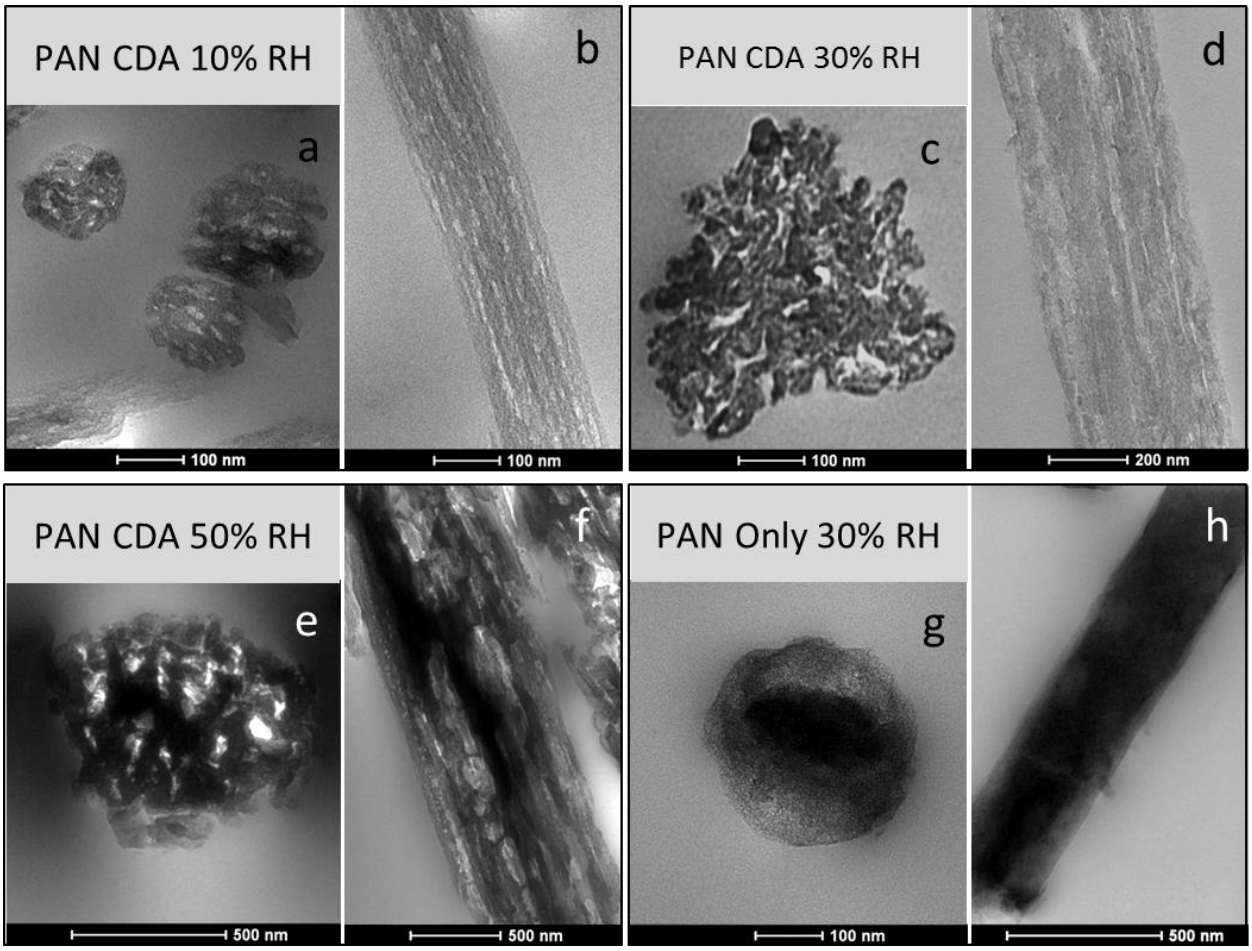

Figure 3: TEM images of the pristine carbonized, activated MPCNF. a-f) are PAN CDA blends electrospun at three different relative humidities. g-h) show PAN only spun at 30% RH. a), c), e), and g) are microtomed sections perpendicular to the fiber axis and b), d), f), and h) are microtomed sections along the fiber axis.

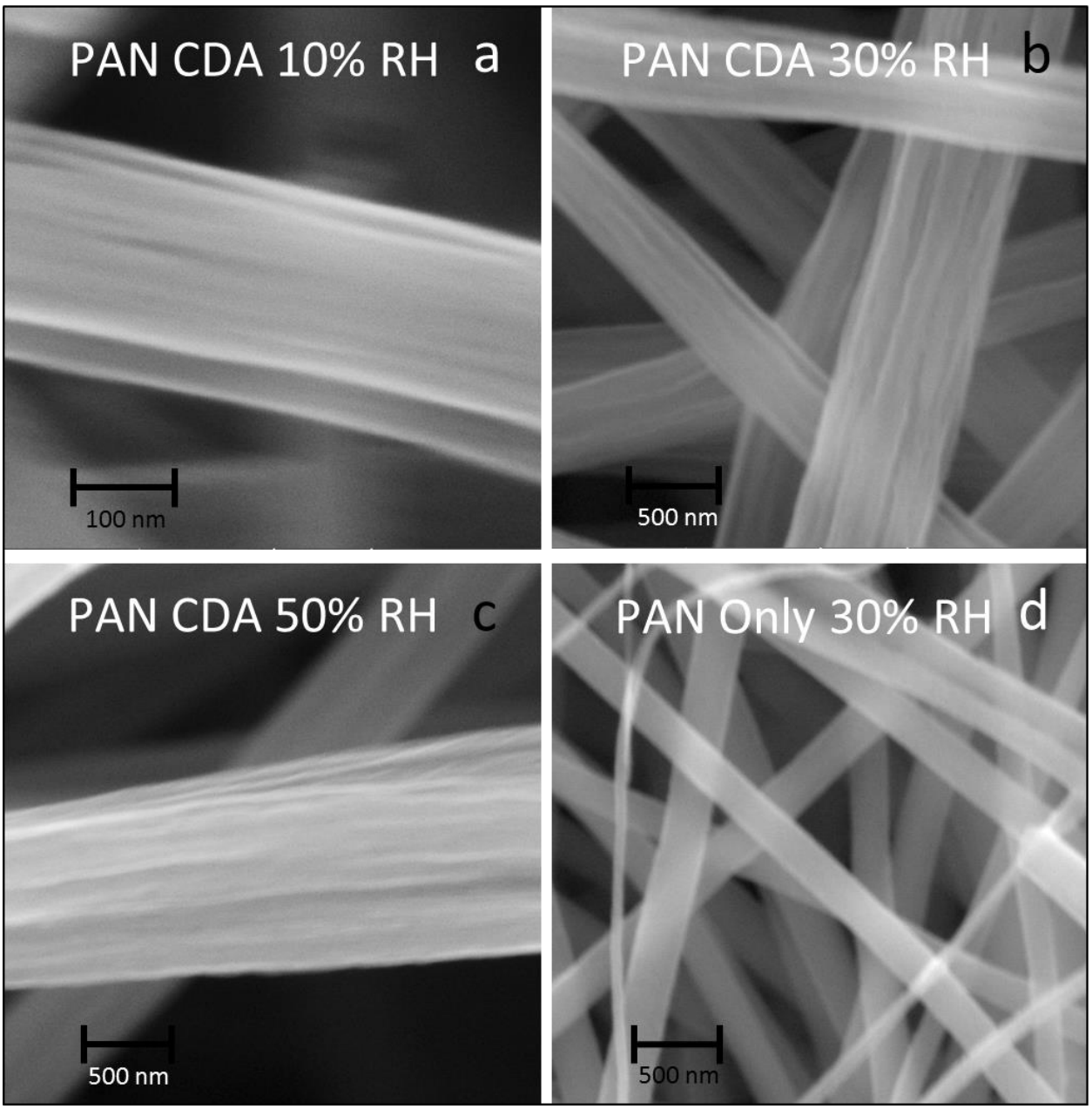

Figure 4: SEM images of the carbonized, activated MPCNF: a) PAN CDA spun at 10% RH, b) PAN CDA spun at 30% RH, c) PAN CDA spun at 50% RH, and d) PAN only spun at 30% RH.

The tortious, ink bottle shaped pores, however, may benefit lithium sulfur interlayers to trap polysulfides inside the pores but still have space to dissolve in the electrolyte and to accommodate the 80% volume expansion in the conversion from sulfur to lithium sulfide.[13-15] In Figure 2c, the interlayers were cycled 28 times and washed in deionized water to remove the

electrolyte salts and lithium sulfide deposits before measuring the pore distribution. The results show that the pore volume of the 30% RH MPCNFs increased after being used as an interlayer. The 10% RH pore peak shifted to slightly larger pores and the 50% RH pore peak shifted to about 50 nm. The TEM images from Figure 5 taken after 28 cycles are supportive of the pore analysis. The cross section of the 30% RH fibers seemed to have their pores cracked apart slightly creating more interconnections perhaps from the volume expansion of sulfur to lithium sulfide. In addition, from the pore size shifts, there seems to be a preference for creating large pores between 20 and 50 nm. 50% RH pores became smaller, 10% RH pores became larger, and 30% RH pores became more numerous, possibly because those pores serve as a balance between the need for surface area and volume for volume expansion through cycling.

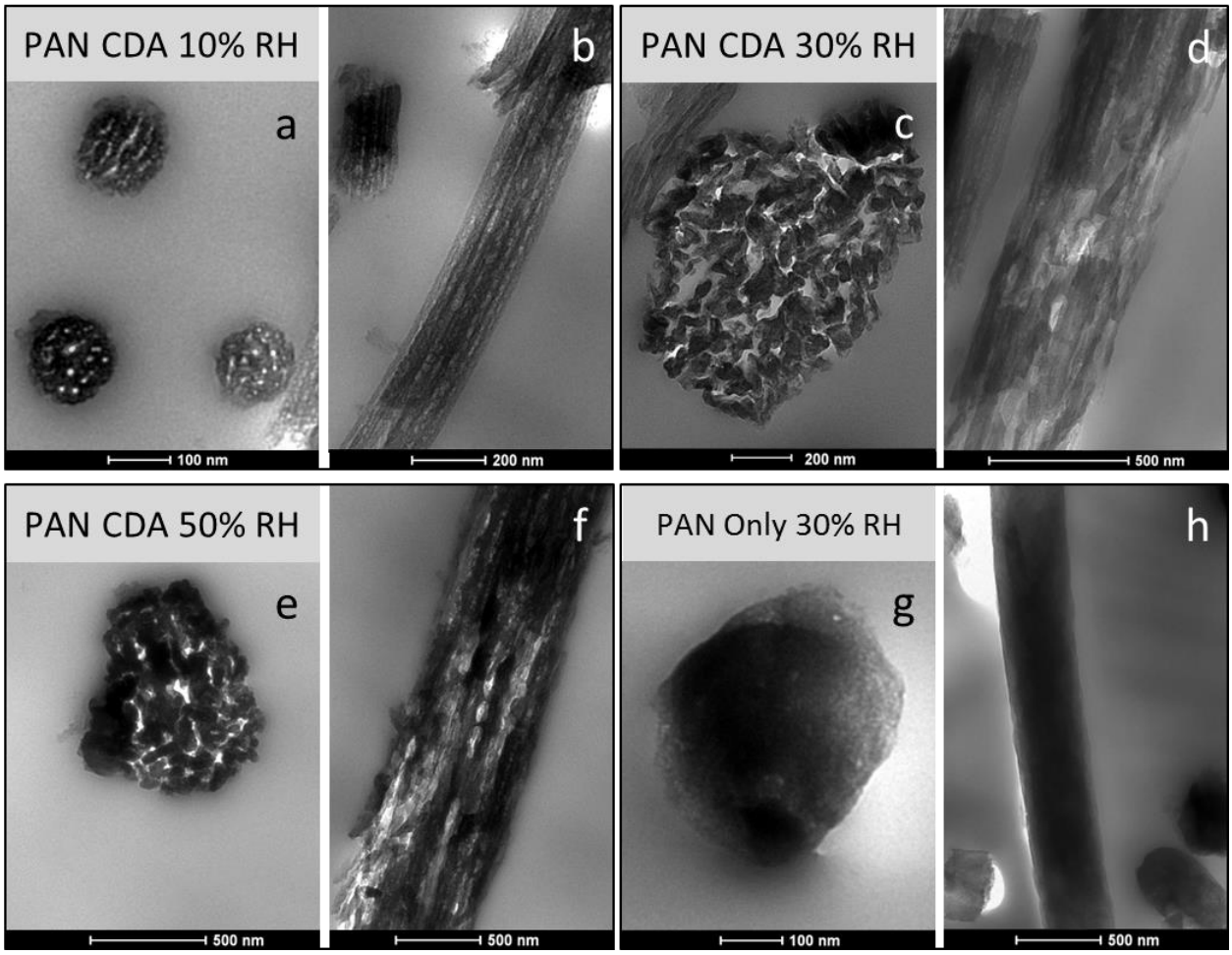

Figure 5: TEM images of the carbonized, activated carbon nanofibers after use as an 18 mg interlayer. a-f) are PAN CDA blends electrospun at three different relative humidities. g-h) show PAN only spun at 30% RH. a), c), e), and g) are microtomed sections perpendicular to the fiber axis and b), d), f), and h) are microtomed sections parallel to the fiber axis.

In Figure 6a and b, the discharge capacity performance was measured for 28 cycles at 0.25C and for over 100 cycles at 0.5C, respectively. The mesoporous samples created at 10%, 30%, and 50% RH clearly show higher performance than the PAN only interlayer, which has micropores but does not contain mesopores. Over 100 cycles the activated mesoporous samples spun at 30% RH and 50% RH still maintained over 1000 mAh g^{-1} capacity which is comparable to other mesoporous carbon interlayers.[32-33] The last sample was spun at 10% RH and has mesopores but was not activated like the others so there was only 30 m^2 g^{-1} of micropores,

obtained from a t-plot analysis, compared to over 400 m^2 g^{-1} for the other samples. By comparing the activated PAN only and the unactivated 10% RH performance, it is concluded that the lack of micropores hinders the performance roughly as much having no mesopores meaning both are useful for high capacity. The initial performance of the unactivated sample was as high as the 10% RH sample with micropores in Figure 6b, but the unactivated sample was not as able to retain its capacity as well without micropores. This supports the conclusion that micropores and small mesopores are important towards trapping polysulfides which was also found by numerous sources.[13-15,31] However, the improvement caused by "adding" large mesopores cannot be explained by an enhanced trapping mechanism since very little surface area was added to the interlayer (<30m^2/g) though an improvement to rate capabilities may.

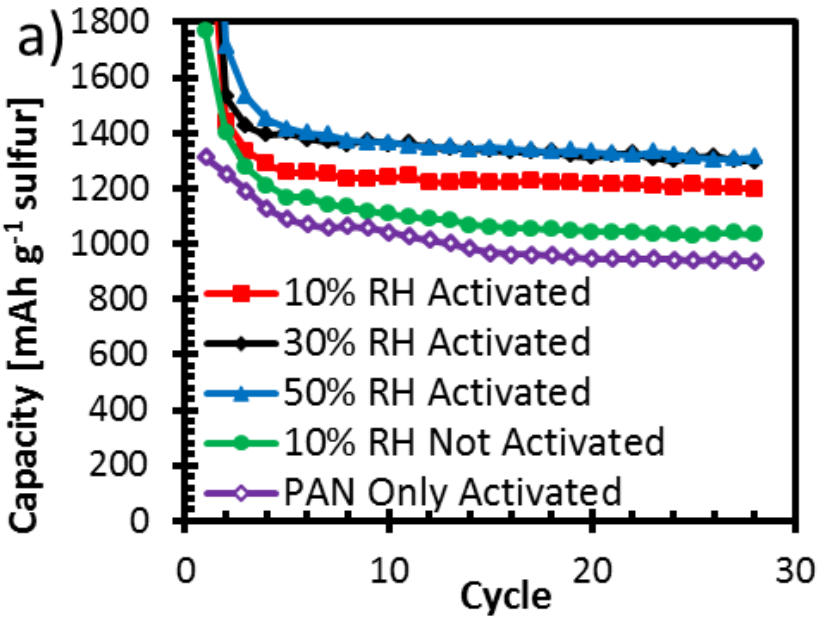

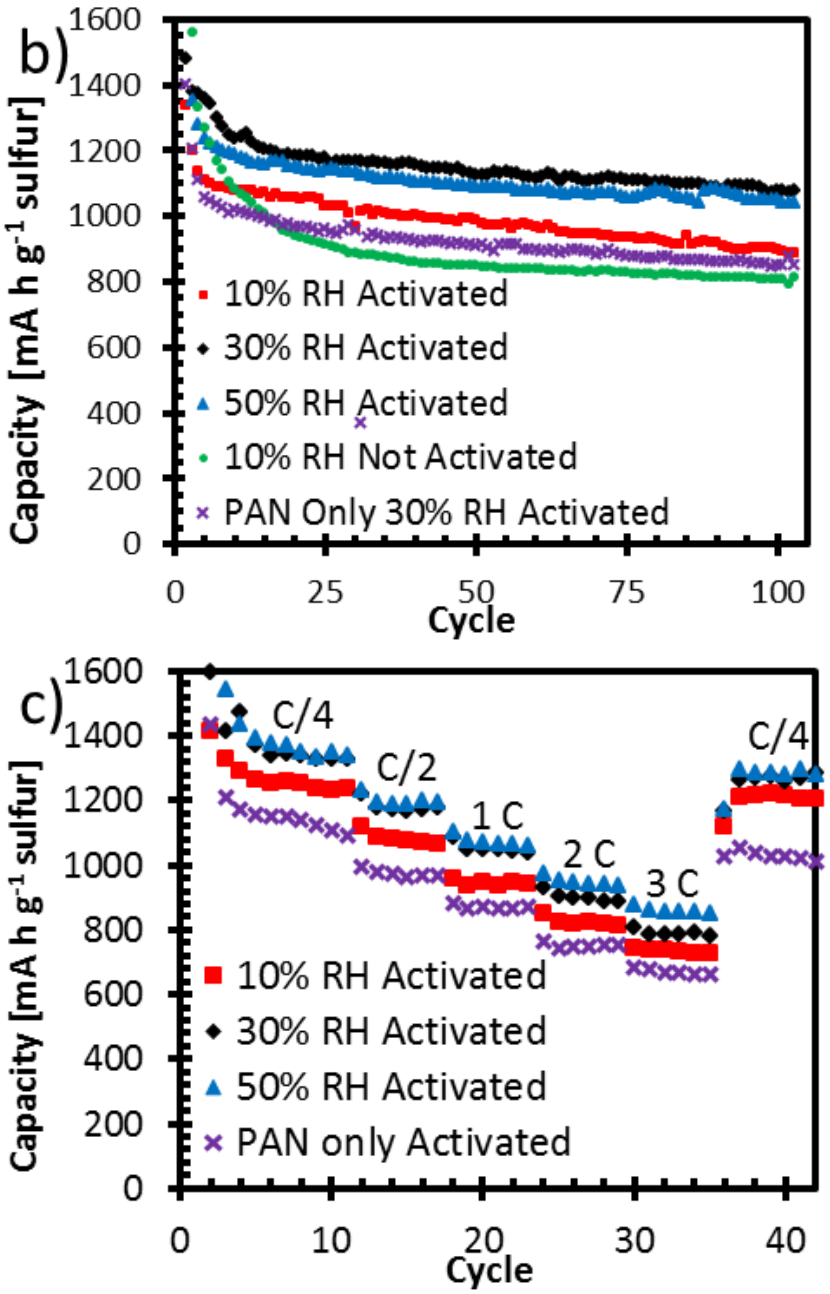

Figure 6: Specific capacity performance for: a) 28 cycles at 0.25C, b) 103 cycles at 0.5C, and c) 10 cycles at 0.25C and 5 cycles at 0.5 C, 1C, 2C, 3C, and 0.25C of cells with 18 mg interlayers of different mesopore and micropore distributions and 1.8mg sulfur cathodes.

To first consider the effect of the mesopore size, notice that there is little difference in performance at 0.25C and 0.5C between the different sizes of mesopores for 30% and 50% RH.

However, the 10% RH sample with the smallest mesopores did not perform as well at 0.25C and performed closer to the microporous PAN only sample at 0.5C than to its larger mesopore counterparts. This could be caused by either long tortious pore interconnectivity or a lithium ion diffusion limitation caused by narrow pore openings to reach the polysulfides trapped inside the interlayer even within the first few cycles. If the adsorption rate of polysulfides on mesoporous carbon from high surface area was the predominate factor for the success of the mesoporous interlayers then there should be little effect from the charging rate since the diffusion rate of polysulfides to and from the anode should not be significantly affected by the rate of the redox reaction.

Figures 6c illustrates the effect of mesopore size on the rate capability further. The batteries were cycled 10 times at 0.25C and then 5 times at 0.5C, 1C, 2C, 3C, and 0.25C again. First, charging at high C rates does not seem to damage the batteries since the capacity at 0.25C seems to be recovered after the 3C cycling, especially after considering the natural loss of capacity after 30 cycles, which has been observed in multiple works.[30-32,36-38] The size of the mesopores has a significant effect with high C rates, supporting that polysulfide adsorption is not the main effect of the mesopore size change. 50% RH, which had the largest pores, retained the most capacity at 1C, 2C, and 3C, approximately 850mA h at 3C. Despite having performance similar to 50% RH at 0.25C and 0.5C, 30% RH did not perform as well at high C rates over 1C presumably because of the smaller pore size. As seen previously in Figure 5c, after being used as an interlayer, the 30% RH pores are interconnected very well, and thus tortuosity should not be a concern. 10% RH which had the smallest mesopores also had the lowest capacity at high C rates and was beginning to approach the performance of the PAN only interlayer with no mesopores.

Unlike micropores, it is thought that mesopores are large enough to prevent diffusion limitations at fast charge rates.

Because the pore size does affect capacity, the system must be diffusion limited rather than kinetically limited at high C rates. Also, since the capacity loss from charging quickly is recoverable when the C rate is return to 0.25C, the polysulfides must be inaccessible at high C rates but accessible at lower C rates. From Figure 6 and TEM images Schematic 1 was created. At low C rates lithium ions are able to diffuse throughout the pore before reacting at the surface. At low C rates the eventual narrowing of the pore entrance is not as critical to meet the current needs of the C rate. At high C rates, however, polysulfides lithiate as soon as the lithium ion enters the pore narrowing and perhaps blocking the entrance of the pore. Narrowing the pore prevents other polysulfides from lithiating since lithium ion diffusion is limited through the small opening to an extent that there are insufficient lithium ions in the pore to maintain the required current, ending the cycle early. Larger pores with larger pore openings reduce the effect. A similar effect of diffusion limited deposit growth was observed by Cheon, *et al.* with Super P cathodes at high C rates between 0.5C and 3C where lithium sulfide buildup seem to block access to the polysulfides with thicker and thicker cathodes.[59]

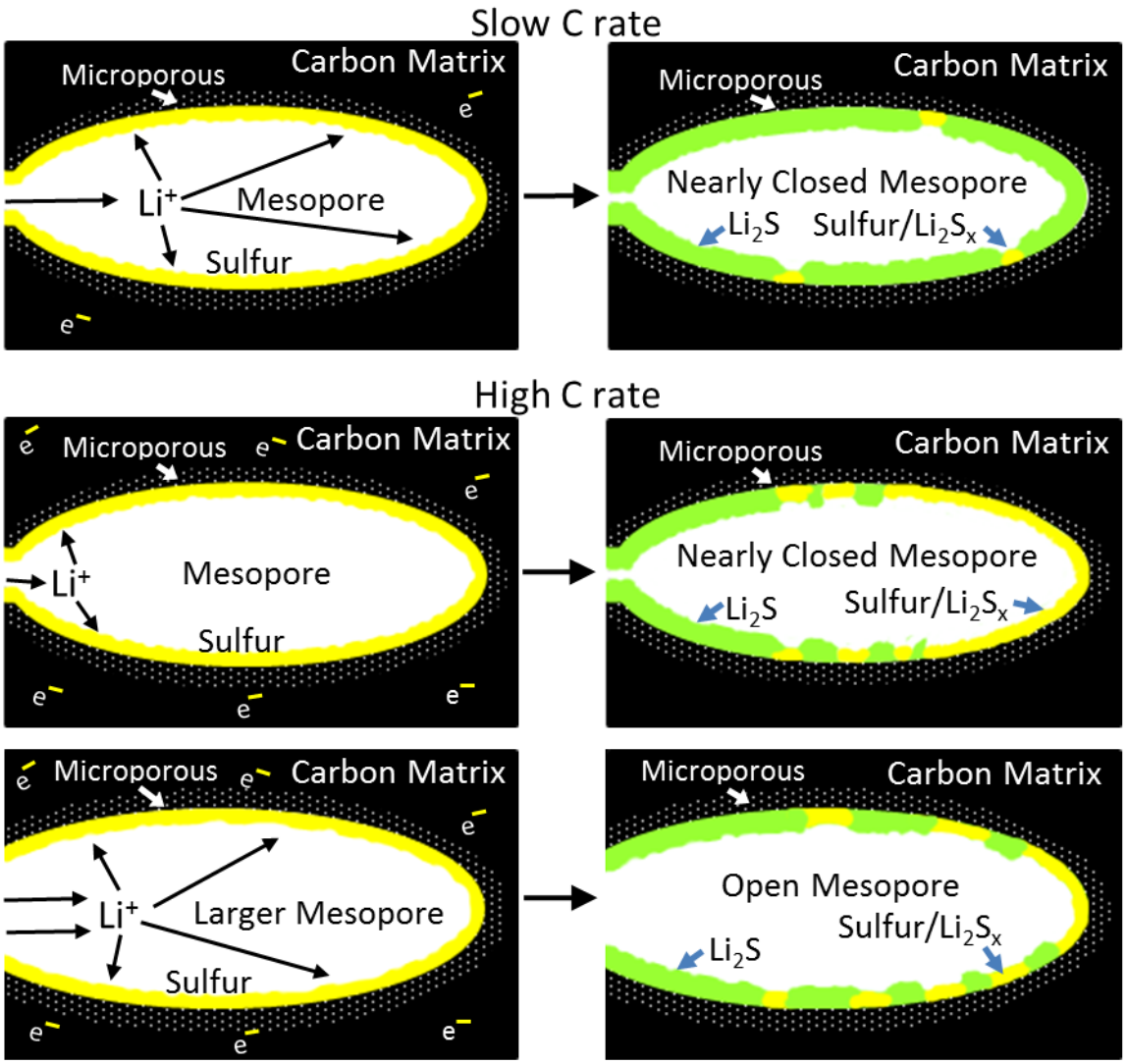

Schematic 1: Illustrates the potential effect of the charging rate. At slow charging rates lithium ions can enough time to diffuse throughout the pore before reacting while at higher charging rates, the ion does not diffuse as far which nearly blocks the pore more quickly before all the sulfur is lithiated. Larger mesopores tend to have larger openings which prevent diffusion limitations.

3.3 Effect of Interlayer Mass

In the previous section, it was shown that adding an interlayer provided a clear benefit to the capacity performance and that large mesopores greatly enhanced the rate capabilities. However, such an improvement in the rate capabilities with an interlayer is only possible if a significant portion of the sulfur left the Super P cathode and was deposited in the interlayer. As

such, the ratio of the mass of the interlayer to the cathode (and thus sulfur loading) is an important variable to consider. In literature it is well known that lowering the overall sulfur loading of a cathode can improve the capacity performance on a sulfur mass basis since more surface area would become available for the same mass of sulfur,[4,10-11,13,22] and that this is a fundamental concern for interlayers since adding an interlayer would lower the overall sulfur composition of the cell.[13,31-32] More significant improvements occur in cathodes when the sulfur loading is lowered enough so that the micropores and mesopores are not completely filled with sulfur.[4,10-11] Without an interlayer, the sulfur composite material used in the current study was 70% sulfur and 30% Super P. If the mass of the interlayer is considered with the mass of the Super P and sulfur then the overall sulfur mass is only ~9wt%, since only 1.8mg of sulfur is contained on the cathode. Therefore it is important to consider how the mass of the interlayer affects the capacity retention.

For carbon interlayers in Li-S batteries to be effective in highly loaded, larger scale batteries, the interlayer must operate like a filter which can trap slowly diffusing polysulfides on their way to the lithium anode. If all the sulfur quickly relocates and evenly distributes itself between the cathode and the interlayer during cycling, then the interlayer effectively acts as a mere extension of the cathode and could be improving performance only by lowering the overall loading of sulfur in the cathode, which is not scalable. Carbon interlayers would not pose much benefit to batteries much larger than coin cells as a thin interlayer would only have a very limited carrying capacity and thicker interlayers would add more weight, lowering the gravimetric energy density. In work by S. Chung and A. Manthiram,[33] a multilayer interlayer of controllable thickness was created and a gradient of sulfur from the cathode to the anode in the interlayer was observed by elemental mapping which strongly supports the idea of a filter. However, it was not

shown whether this mechanism improved the capacity retention beyond the effect of merely lowering the overall sulfur composition. Coin cells with varying masses of interlayers and overall sulfur loading were made to explore this hypothetical problem.

First, the mass of the cathode was held constant to contain 1.8mg of sulfur and the mass of the interlayer was varied from 0 to 34mg (0-12mg cm^{-2}). The mass of the interlayer was controlled by spinning the initial fiber mat thicker or thinner and layering multiply interlayers together. There was no significant difference in performance between multiple layers of interlayers and a single layer interlayer if the total mass was the same. The performance of the tenth cycle is given in Figure 7a to compare fairly stable capacities after the rapid decrease in capacity from the initial cycles.

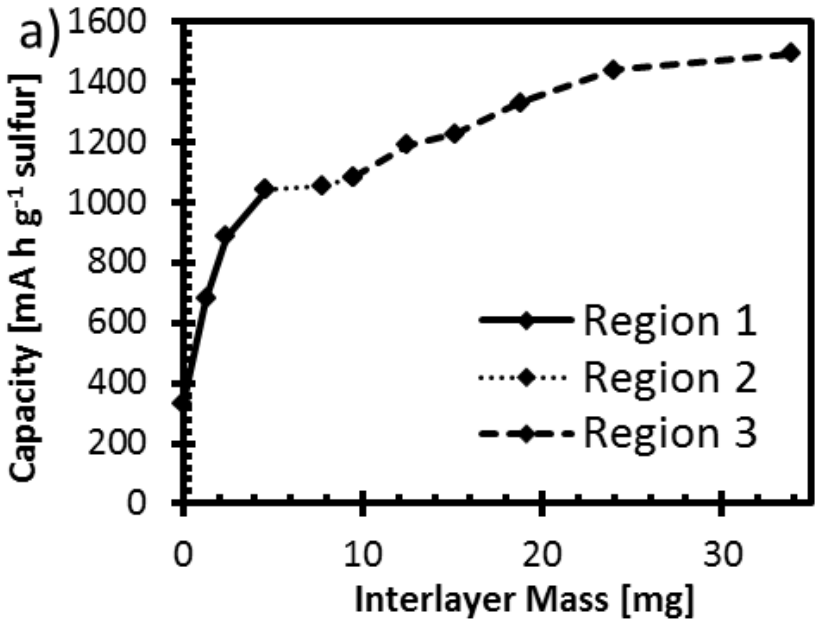

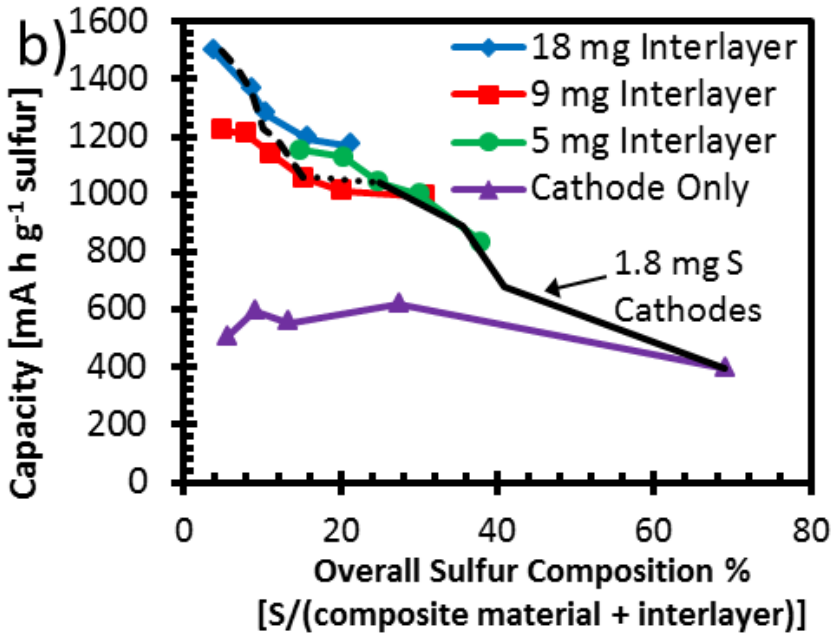

Figure 7: a) The specific capacity of lithium sulfur batteries with increasing interlayer mass and a constant cathode mass containing 1.8 mg sulfur taken at the 10th cycle and ran at 0.25 C. The three regions are displayed for analysis purposes. b) Different masses of interlayers are compared across their overall sulfur composition by manipulating the amount of active materials on the cathode at 0.25 C. The black line connects results with 1.8 mg S on the cathode current collector taken from a) broken into the same three regions for analysis.

Overall heavier, thicker interlayers with more total surface area are more effective interlayers. With increasing interlayer mass, there appears to be three regions. From no interlayer (0 mg) to 1, 2, and 5 mg interlayers there is a rapid improvement in performance (region 1) and reaches a small plateau (region 2). Afterwards the curve increases again and appears to start leveling off with thick enough interlayers to around 1500mA h g^{-1} sulfur (region 3). Such behavior would be expected for a filter, since as the filter grows thicker, less of the filtrate should penetrate through. However as stated earlier, the overall sulfur composition decreases as the interlayer grows in mass.

In a second set of experiments (Figure 7b), the overall sulfur composition is held constant by adjusting the amount of sulfur in the cathode with 5mg, 9mg, and 18mg interlayers. This was accomplished by casting a thicker or thinner composite material layer on the cathode current collector using the same 30% Super P, 70% sulfur composite recipe with binder. In particular, Super P which lacks large amounts of micropores was chosen as the cathode carbon so that the effects of partial micropore filling would not influence the results if the sulfur does redistribute itself. The "Cathode Only" experiments used specially made cathodes where less sulfur was loaded into the Super P to make the desired overall sulfur composition comparable to the other experiments where interlayers were used. The black dashed, dotted, and solid line connects the data from Figure 7a which all have a constant 1.8mg loading of sulfur.

We note that all samples with interlayers performed better than having no interlayer at all despite having the same overall sulfur composition. Looking at the 18mg and 9mg interlayers alone, lowering the overall sulfur loading increased the capacity and raising the overall sulfur loading hindered the performance. At the same overall sulfur composition, a more massive 18mg interlayer improved performance over a 9mg interlayer suggesting a filter mechanism where the polysulfides could not penetrate through as quickly thus preventing the buildup of nonconductive lithium sulfides on the anode and the polysulfide shuttling mechanism. Considering the curves for 9mg and 18mg interlayers individually, each starts with a higher capacity at a lower sulfur loading and seems to level out at the highest sulfur loading which was possible to test given the experimental cell coin setup. When the 5 mg sulfur composition was too high, its performance is similar to a thinner interlayer. When comparing the 5mg interlayer and the 9mg interlayer with the line for the 1.8mg sulfur loading which corresponds to the small plateau in Figure 7a, 5mg and 9mg interlayers had similar performance despite the 9mg interlayer having a lower overall

sulfur composition until higher sulfur composition are reached. When the actual sulfur loadings are considered the 9mg interlayer always performed roughly as well but slightly better than the 5 mg interlayer. Since the actual sulfur loading matters between 5 and 9 mg interlayers rather than just the overall sulfur composition, it is thought that the amount of weakly adsorbed sulfur on the Super P cathode outer surfaces increases with the larger cathodes used to increase the sulfur composition for the 9 mg interlayer. Comparing 18mg and 5mg interlayers, the 18mg interlayer approaches the higher plateau of capacity for the 5mg interlayer at the highest sulfur loadings for 18mg. The 18mg interlayer was always better than the 5mg interlayer at a particular sulfur composition or sulfur loading.

To explain these results, the results of Figure 7a (constant 1.8 mg S cathodes) are considered in three hypothetical regions. Between 0 and 5mg of interlayer mass (above 25% overall sulfur shown in the solid line), before the first, small plateau, all the mesopores and micropores throughout the interlayer are completely saturated or blocked to the lithium polysulfides diffusing from the Super P cathode which the cathode could not hold in place with its surface area. The interlayer cannot hold any more polysulfides, and so the polysulfides quickly reach the anode to lower the capacity. Between 5mg and 9mg of interlayer mass (15 – 25% overall sulfur, shown in the dotted line), or the first plateau, not all of the mesopores are saturated or blocked with deposits but some or most are. The mesopores can continue to hold more polysulfides and the varying degrees of a partially filled or blocked pore does not significantly change performance as some polysulfides have already broken through the filter but the majority of the sulfur is prevented from participating in the shuttle mechanism. At and above 9mg of interlayer mass (less than 15% overall sulfur), more micropores become available to trap

diffusing polysulfides so few can diffuse and break through the interlayer improving performance by preventing the nonconductive layer on the anode.

When more sulfur is loaded into a 18mg interlayer cell to match the overall sulfur composition of a 5mg interlayer cell, more sulfur is available to leave the cathode. With 1.8mg sulfur in the cathode, the 18mg interlayer can use its micropores to store the polysulfides but at higher sulfur loadings, its mesopores start to fill or close from the excess of sulfur causing its performance drop to a level similar to that of a 5mg interlayer loaded with 1.8mg sulfur in the cell. However, thicker, more massive interlayers with unblocked pores such as 9mg and 18mg interlayers with the same 1.8mg of sulfur decreases the chance that polysulfides diffuse completely through the inter-fiber spaces without interacting with them. In thin, less massive interlayers, all the strongly adsorbing micropores are filled early on, but the interlayer still provides some barrier to polysulfide diffusion as mesopores are filled. A 5mg or smaller interlayer still provides a large benefit to the capacity retention disproportionate to the amount it lowers the sulfur composition. Therefore, it is concluded that for a sufficiently large battery cathode to have a decent overall sulfur loading, a cell which relies purely on a carbon interlayer for decent performance would have a maximum such as ~1000mAh/g at 5mg as the optimal balance between sulfur loading and capacity for this system. This would correspond to the point where enough sulfur would be diffusing out of cathode to saturate the interlayer's small pore volume of micropores and begin filling or blocking the mesopores. Beyond that, increasing the mass of the interlayer would have diminishing returns to capacity retention and would further lower the overall sulfur composition.

To explore the idea of pore filling or pore closing, microtomed cross-sectional TEM images of the interlayers were taken perpendicular to the axis of the fiber (Figure 8). The images

were taken after being used as an interlayer in a lithium sulfur battery for 28 cycles, left in the discharged state, and washed overnight three times in the electrolyte solvents. The 2mg interlayer (Figure 8a) shows some rough deposits within the mesopores and both the 2mg and 5mg interlayer (Figure 8b) appear to have its pores enclosed, and blocked from reaching the surface rather than being completely filled with reaction products. The 18mg interlayer (Figure 8c) shows some deposits but many pores seem to reach the surface. The 32mg interlayer (Figure 8d) looks the closest to the original unused MPCNF given in Figure 8e. The interlayers were washed in electrolyte solvents to remove the electrolyte salts but leave behind the sulfur and lithium sulfide deposits. Figure 8g shows a used 18mg interlayer with no solvent wash. The presence of the salts in the seemingly blocked, unwashed pores suggests that the majority of the pores are reachable for the electrolyte, at the start of cycling at the least, and that the solvent wash was effective in removing the salt, meaning that the pores cannot be completely closed. However, to measure the surface area and pore distribution, the electrolyte solvent wash did not seem effective. All samples appeared to have similar and rather small pore volume distributions despite the TEM images.

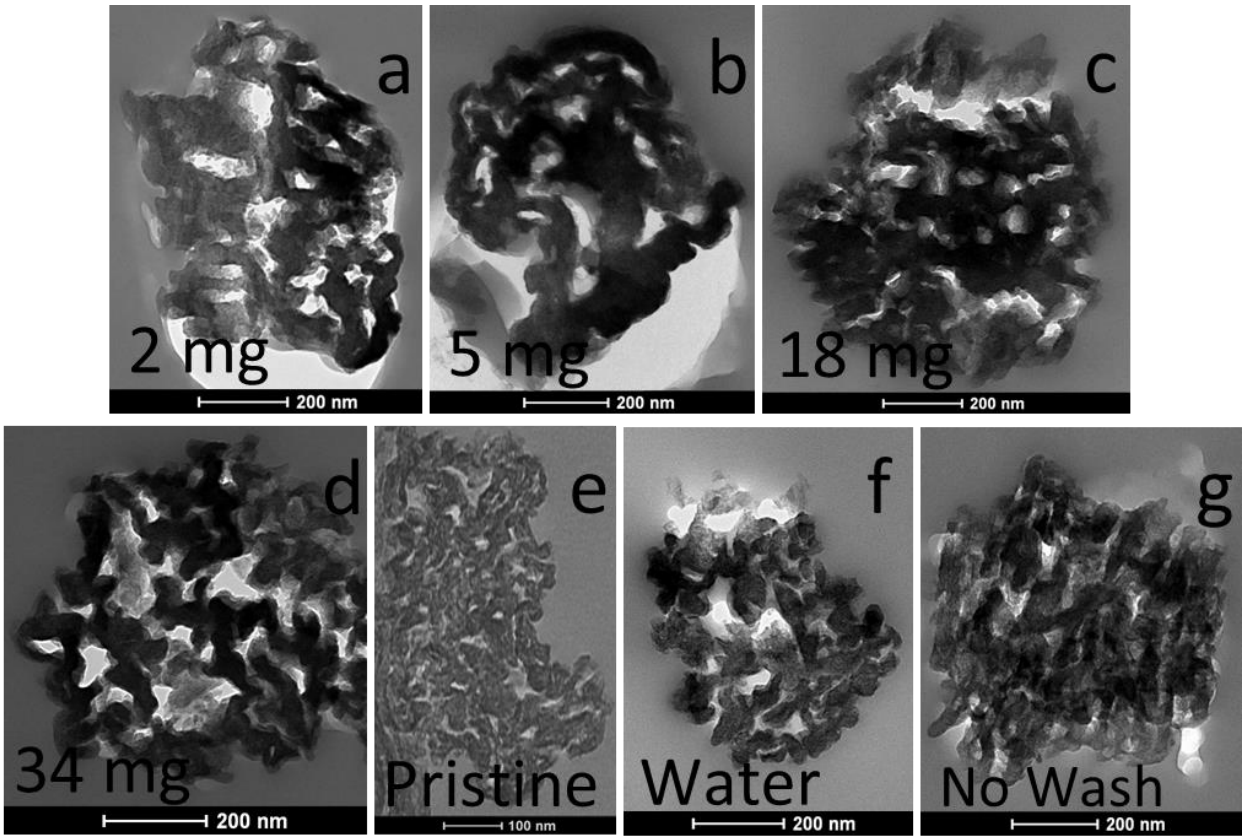

Figure 8: Microtomed cross sectional TEM images perpendicular to the axis of the fiber embedded in epoxy. a)-d) were used in as a 2, 5, 18, and 34 mg interlayer respectively for 28 cycles and were washed in the electrolyte solvents e) before use as an interlayer. f) a used 18 mg interlayer but washed in deionized water. g) a used 18 mg interlayer without any wash before imaging.

In Figure 9, the interlayers were washed with deionized water and the resulting distributions are more representative of the TEM images (Figure 8f). Since lithium sulfide is soluble in water, only sulfur or sulfur covered deposits should remain. The 2 mg interlayer has major mesopore blockages and the 5 mg interlayer has significant pore blocking compared to the pore distribution of the pristine MPCNF. Since the blockage remains after washing with water, it is thought that the shuttle mechanism trapped sulfur deposits from participating in the redox reactions by blocking direct access to lithium ions with a lithium sulfide coating. The 9, 18, and 32mg interlayers also showed more mesoporous volume from volume expansion cracking which

supports the observation from the TEM images in Figure 5. The pore distribution for the 32 mg interlayer nearly matches the pristine MPCNF distribution suggesting it was relatively unused. The 32, 18, and 9 mg interlayers also had a substantially larger microporous area free from insoluble deposits than the 2 and 5 mg interlayers obtained from the BET and t-plot analysis which would be available during normal cycling.

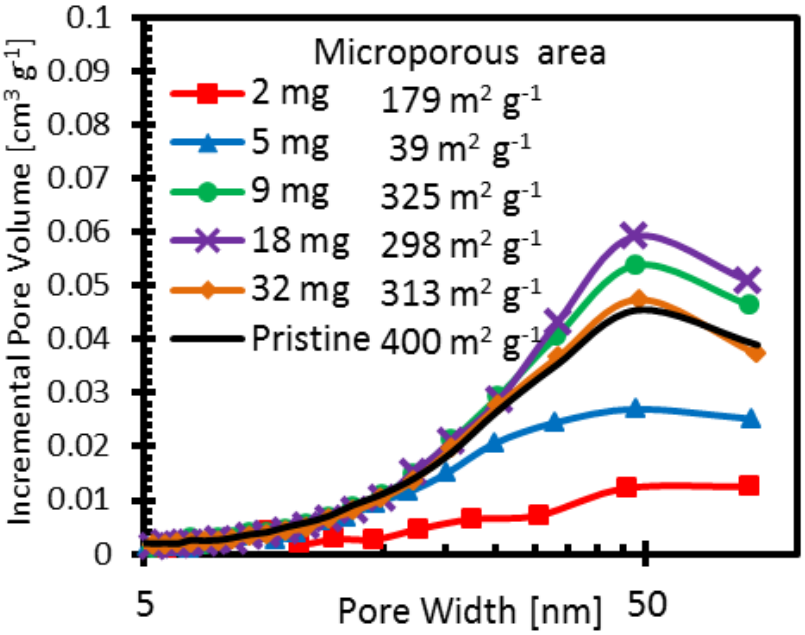

Figure 9: An incremental pore volume distribution of the various masses of used interlayer and the pristine MPCNF material using the BJH method with nitrogen physisorption. Supporting info: raw data

3.4 Effect of Cathode Material

However, there are still two factors to consider. One is the nature of the carbon in the cathode. Super P stores the sulfur on external surfaces rather than pores, so it does not store the sulfur as well as an activated carbon (AC) with unfilled micropores. Super P was chosen to test the interlayers in that regard, since it does not hold sulfur as tightly providing a better stress test. In addition, Super P would not have effects related to pore filling in the cathode. None the less, a MPCNF interlayer is more of an activated carbon in surface chemistry and surface area than a

carbon black like Super P. A comparison of different cathode materials is given in Figure 10. Even at the low loading of 9wt% sulfur in an activated carbon cathode, where sufficient pores should be available, performance is similar to Super P without an interlayer in Figure 10a. Sulfur was loaded to 9wt% sulfur in the composite material of the cathode to match the overall sulfur loading of the 70wt% sulfur cathode with an 18mg interlayer. Also given in Figure 10a, the same activated mesoporous carbon from the interlayers was ground up, made into a cathode, and tested without an interlayer. The capacity for the 9wt% sulfur MPCNF cathode was around 200 mA h g^{-1} sulfur less than the 9wt% sulfur AC and Super P cathodes, showing that the increase in performance is not strictly related to the mere presence of the MPCNF material or from lowering the sulfur loading but when the material acts as an interlayer in the cell.

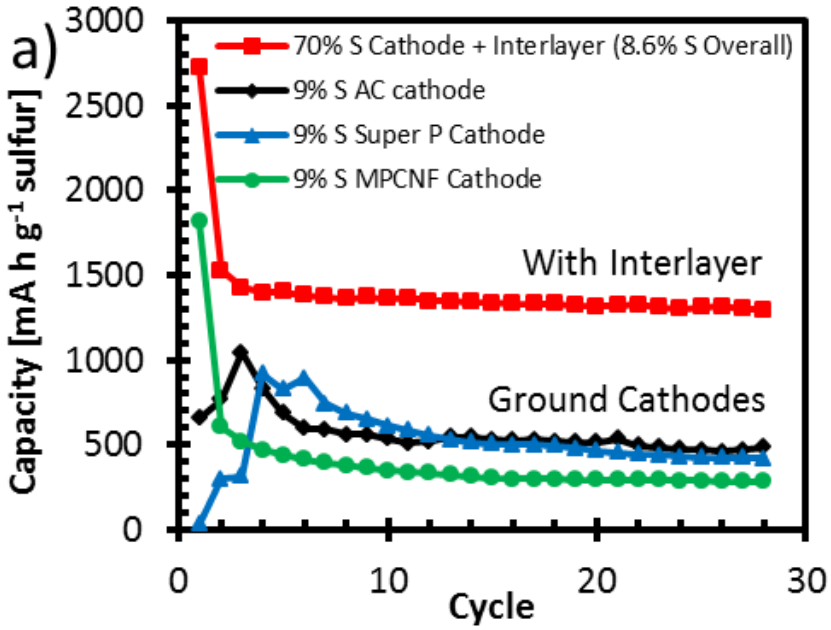

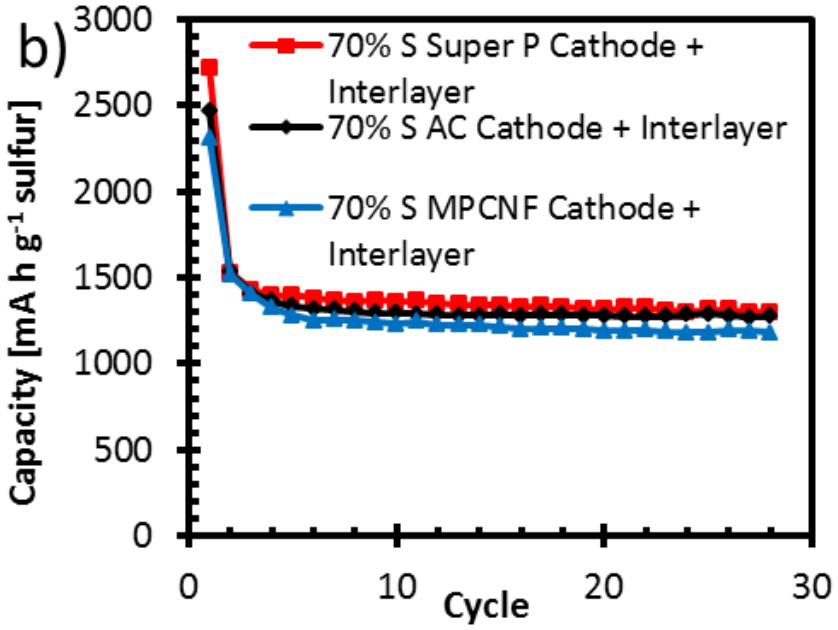

Figure 10: a) Compares the same overall loading of sulfur of an 18 mg interlayer cell to cathode only cells made with activated carbon (AC), Super P, and MPCNF at 0.25C. b) All the samples have 18 mg MPCNF interlayers and 1.8 mg sulfur in the cathode but the cathode material was varied. All three cathodes were 70wt% sulfur.

Unlike a cathode, interlayers do not start with sulfur evenly dispersed throughout them and would retain lower polysulfide concentrations than a cathode near the membrane and anode. If sulfur was quickly and evenly redistributed from the cathode to the interlayer to effectively make one a large cathode in the first few cycles, there should be no difference between the sample with an interlayer and the 9wt% sulfur cathodes. Both Figure 7b and 10a support the opposite. Since the 2 and 5mg BJH pore distributions from Figure 9 support that polysulfides do enter and remain in the interlayer and that interlayers do improve the lithium sulfur capacity beyond the effects of lowering the sulfur loading, a filter mechanism such as in a fixed adsorption bed is a reasonable conclusion as previously reported. In Figure 10b, all the cathodes, now with 70% sulfur composite materials, are effective cathodes when paired with an interlayer

showing the robustness of the interlayer even with the simplest of cathode materials such as activated carbon.

3.5 Effect on Conductivity

One last factor to consider is the effect that interlayers can add more conductivity to the cell as an additional current collector as originally shown by Su and Manthiram.[25] Having a conductive carbon above the cathode could help the cathode in transferring electrons to the current collectors. However, if the thickness of the composite material on the cathode increases to store more sulfur during scale up, then the benefit of the extra current collector on the top layer of the active material would not scale with the battery. In Figure 11a-b, impedance spectroscopy is given for before cycling and after 10 cycles both at the fully charged state of the battery. Comparing the impedance from the cell with interlayers and without interlayers, the interlayers lower the resistance of the cell even before cycling which supports the idea that the interlayer acts like an additional current collector. From literature, it is known that lithium sulfur battery Nyquist plots can be modelled in part by a combination of two semicircles from their associated resistance and capacitance.[60-61] It is thought that at high frequencies the resistance and capacitance is from the interphase contact between the current collector and the reaction sites, and at medium frequencies that the resulting semicircle is from the charge transfer resistance transferring the ionic charge from the sulfur into the electrolyte and the double layer capacitance.

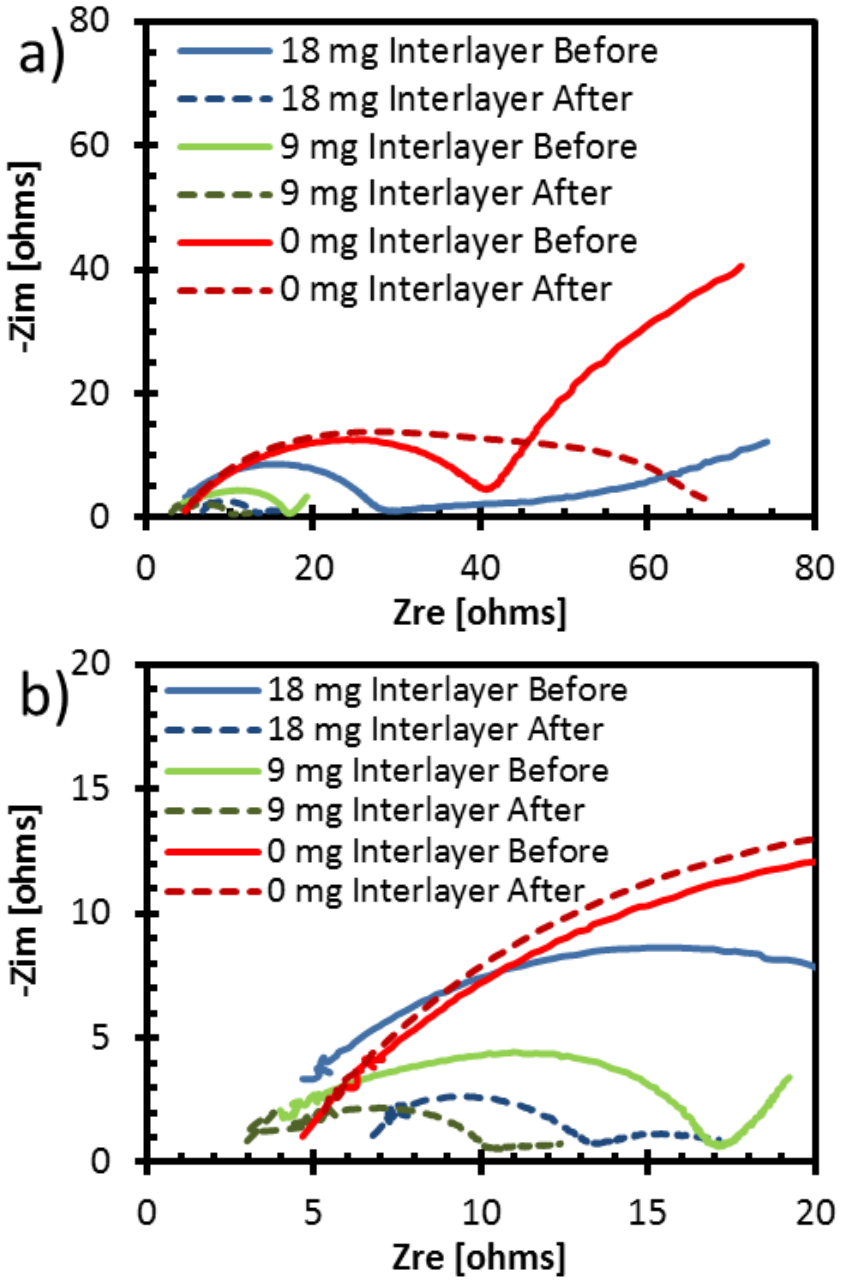
a)
18 mg Interlayer Before
18 mg Interlayer After
9 mg Interlayer Before
9 mg Interlayer After
0 mg Interlayer Before
0 mg Interlayer After
-Zim [ohms]
Zre [ohms]
0
20
40
60
80
b)
18 mg Interlayer Before
18 mg Interlayer After
9 mg Interlayer Before
9 mg Interlayer After
0 mg Interlayer Before
0 mg Interlayer After
-Zim [ohms]
Zre [ohms]
0
5
10
15
20

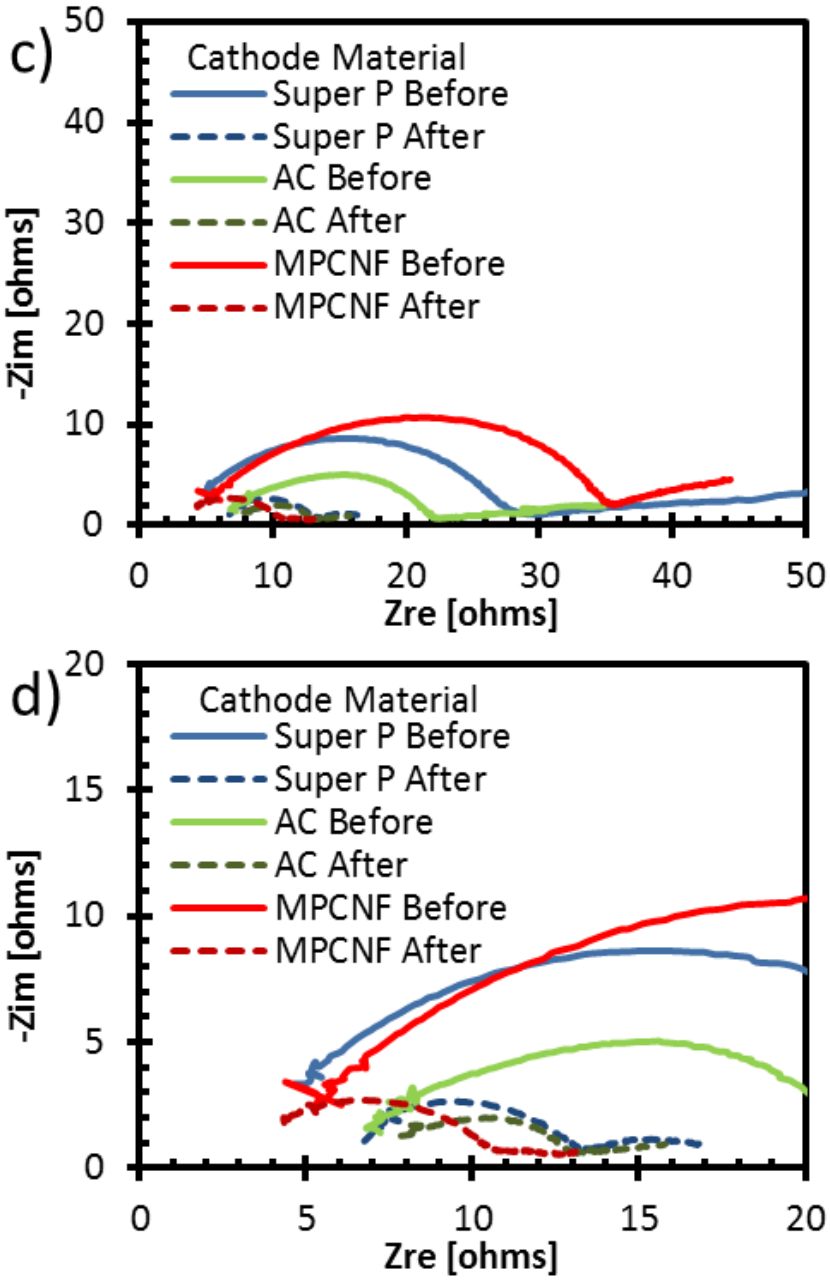

Figure 11: Impedance spectroscopy comparing: a-b) the difference between different masses of interlayers and c-d) the difference between different cathode materials of 70% sulfur cathodes with an 18mg MPCNF interlayer before and after 10 cycles. All batteries were measured fully charged.

Before cycling, the two components appear to be lumped together and are not visually distinguishable. Comparing to work by Deng, *et al.*, the combined single semicircle and tail is

consistent with a fully charged lithium sulfur battery and the resistance is mainly from charge transfer.[60] After 10 cycles without an interlayer, the impedance increases and the two components to the impedance start to become visible. This is thought to be mainly charge transfer resistance from agglomerations of insulting lithium sulfides on the cathode surface.[60] With an interlayer, however, the impedance of the cell decreases after cycling. In Deng, *et al*., it was shown that within the first cycle upon partially discharging the cell that the charge transfer and interphase resistances greatly decrease as well. It was suspected that this is due to the initial sulfur aggregates reacting and dissolving into polysulfides allowing for easier access for Li ions.[57] On further charges the sulfur is more evenly distributed within the cathode and interlayer to reduce resistance by not blocking diffusion.[15] In the case of an interlayer, the impedance decreases from the sulfur dissolving and distributing itself in the cathode but maintains low impedance by limiting the polysulfide shuttle mechanism and avoiding a nonconductive layer on the anode.

Comparing the 9mg and 18mg interlayer, the thicker interlayer provided more resistance before cycling, but after 10 cycles, judging from the width of the semicircles, the total resistance is approximately the same. The slight shift to the right for 18mg interlayer is thought to be a small increase in the electrolyte resistance.[60] Since 18mg and 9mg have similar impedances but the 18mg interlayer still creates better performance within the cell, it supports that its effect as a filter dominates over its effect as an extra current collector though both effects may still be important. In Figure 11c-d, cathodes made from Super P, AC, and MPCNF are paired with an 18mg MPCNF interlayer and are shown to have similar impedances after 10 cycles. Since the capacity retention is similar as well for these cathodes it supports that the observed improvements are not related to the cathodes but to the interlayer.

4. Conclusions

The potential of interlayers for lithium sulfur batteries is that they can be a simple addition to a cell but greatly improve capacity. Adsorbing the polysulfides from before they reach the lithium anode prevents electrically insulating lithium sulfides from forming on the anode surface and prevents them from participating in the polysulfide shuttle mechanism while still participating in cycling. Conductive mesoporous carbon nanofibers with large mesopores pores from immiscible blended polymers were created as a cost efficient way to make an effective interlayer with a significant improvement to capacity and rate capabilities over a plain cathode cell or a purely microporous interlayer. By controlling the size of the large mesopores, diffusion limitations were observed with large $\sim$30nm mesopores above 1C but were alleviated with an interlayer with even larger ($\geq$50nm) mesopores. While effective as an interlayer regardless of the cathode material, for the effect of the interlayer to scale with the size and loading of the battery the interlayer must act like a filter rather than an additional cathode. To study this further, it was shown that the capacity increased with more massive interlayers and that more massive interlayers would provide better capacity despite having the same overall sulfur composition. Impedance spectroscopy showed that interlayers lowered the resistance of the cell, especially after some cycling. Thicker and thinner interlayers resulted in similar charge transfer resistances but thicker, more massive interlayers still have better capacity retention meaning that the current collector effect is not the dominating mechanism for better capacity retention with interlayers. While sulfur will inevitably diffuse out of the cathode and into the interlayer and eventually to the anode limiting the long term cyclability, interlayers still appear to be a simple method to improve the capacity retention of lithium sulfur batteries and may work well in conjunction with an advanced, highly loaded cathode to obtain superior performance.

Acknowledgements

The authors would like to acknowledge the Cornell Center for Materials Research Shared Facilities which are supported through the NSF MRSEC program (DMR-1120296) and Axium Nanofibers for funding.

Supporting Information

SEI: Figure 2

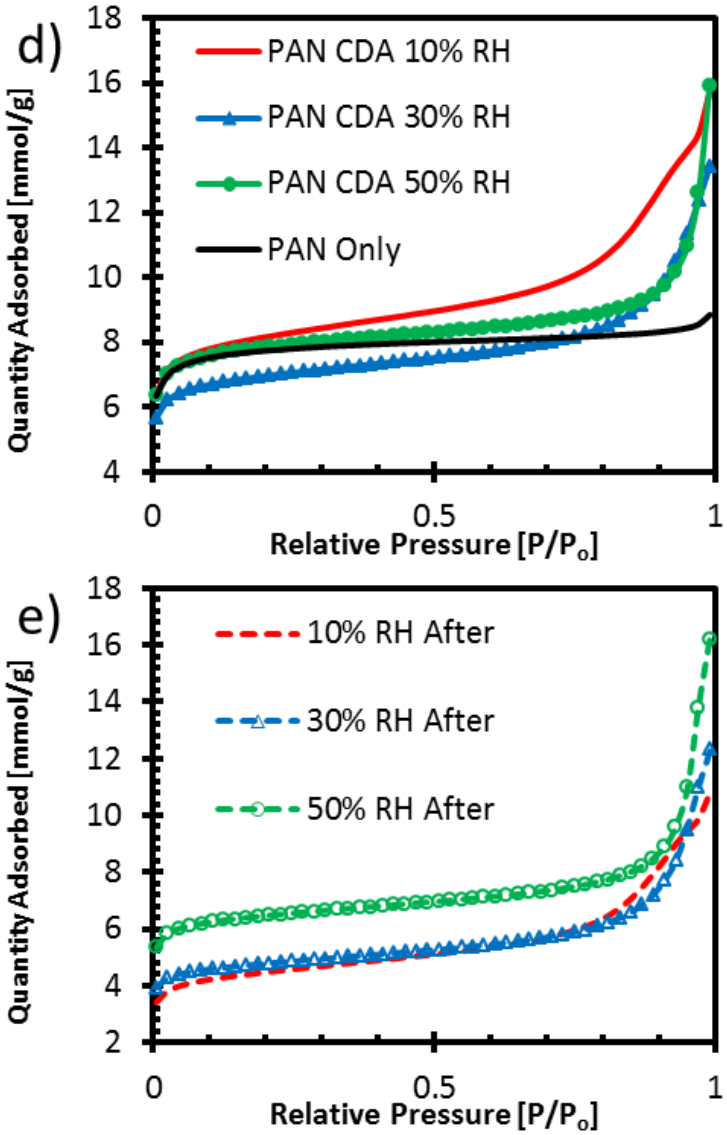

SEI Figure 2: Nitrogen physisorption absorption isotherm data d) for 2a and 2b and e) for 2c

SEI: Figure 9

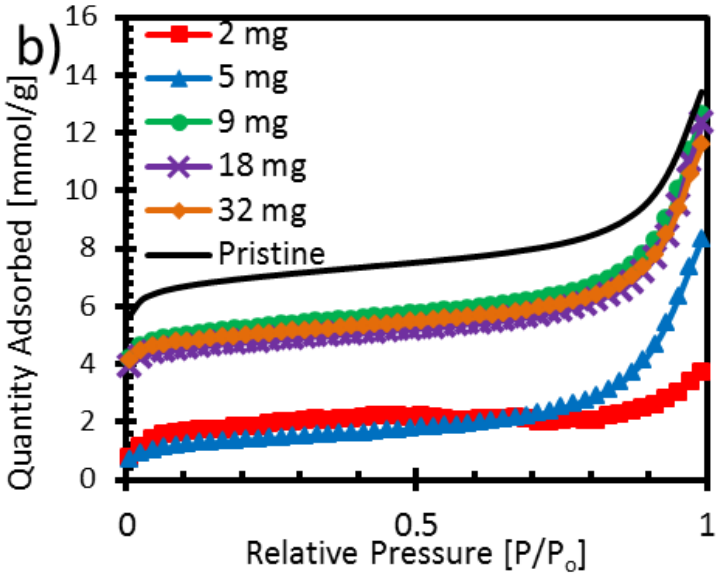

SEI Figure 9: b) Nitrogen physisorption absorption isotherm data

REFERENCES

1. C. Liang, Z. Li, S. Dai, Mesoporous carbon materials: synthesis and modification, Angew. Chem. Int. Ed. Engl., **47**, 3696 (2008).
2. R. Ryoo, S. H. Joo, M. Kruk, M. Jaroniec, Ordered Mesoporous Carbons, Adv. Mater., **13**, 677 (2001).
3. J. Lee, J. Kim, T. Hyeon, Recent Progress in the Synthesis of Porous Carbon Materials, Adv. Mater., **18**, 2073 (2006).
4. X. Li, Y. Cao, W. Qi, L. V. Saraf, J. Xiao, Z. Nie, J. Mietek, J.-G. Zhang, B. Schwenzer, J. Liu, Optimization of mesoporous carbon structures for lithium–sulfur battery applications, J. Mater. Chem., **21**, 16603 (2011).
5. G. Girishkumar, B. McCloskey, A. C. Luntz, S. Swanson, W. Wilcke, Lithium−Air Battery: Promise and Challenges, J. Phys. Chem. Lett., **1**, 2193 (2010).
6. G. He, X. Ji, L. Nazar, High "C" rate Li-S cathodes : sulfur imbibed bimodal porous carbons, Energy Environ. Sci., **4**, 2878 (2011).
7. M. Barghamadi, A. S. Best, A. I. Bhatt, A. F. Hollenkamp, M. Musameh, R. J. Rees, T. Ruther, Lithium–sulfur batteries—the solution is in the electrolyte, but is the electrolyte a solution?, Energy Environ. Sci., **7**, 3902 (2014).
8. C. Liang, N. J. Dudney, J. Y. Howe, Hierarchically Structured Sulfur/Carbon Nanocomposite Material for High-Energy Lithium Battery, Chem. Mater., **21**, 4724 (2009).
9. A. Manthiram, Y. Fu, Y. Su, Challenges and Prospects of Lithium-Sulfur Batteries, Acc. Chem. Res., **46**, 1125 (2013).
10. L. Ji, M. Rao, S. Aloni, L. Wang, E.J. Cairns, Y. Zhang, Porous carbon nanofiber–sulfur composite electrodes for lithium/sulfur cells, Energy Environ. Sci., **4**, 5053 (2011).
11. B. Zhang, X. Qin, G. R. Li, X. P. Gao, Enhancement of long stability of sulfur cathode by encapsulating sulfur into micropores of carbon spheres, Energy Environ. Sci., **3**, 1531 (2010).
12. S. Cheon, K. Ko, J. Cho, S. Kim, E. Chin, Rechargeable Lithium Sulfur Battery I. Structural Change of Sulfur Cathode During Discharge and Charge, J. Electrochem. Soc., **150**, A796 (2003).
13. J. G. Wang, K. Xie, B. Wei, Advanced engineering of nanostructured carbons for lithium-sulfur batteries, Nano Energy, **15**, 413 (2015).
14. J. Q. Huang, Q. Zhang, F. Wei, Multi-functional separator/interlayer system for high-stable lithium-sulfur batteries: Progress and prospects, Energy Storage Mater., **1**, 127 (2015).
15. A. Manthiram, Y. Fu, S. Chung, C. Zu, Y. Su, Rechargeable Lithium − Sulfur Batteries, Chem. Rev., **114**, 11751 (2014).
16. G. R. C. Li, S. H. Ye, X. P. Gao, A Polyaniline-coated sulfur/carbon composite with an enhanced high-rate capability as a cathode material for lithium/sulfur batteries, Adv. Energy Mater., **2**, 1238 (2012).

17. G. Zheng, Y. Yang, J. J. Cha, S. S. Hong, Y. Cui, Hollow Carbon Nanofiber-Encapsulated Sulfur Cathodes for High Specific Capacity Rechargeable Lithium Batteries, Nano Lett., **11**, 4462 (2011).
18. M. Song, J. Cairns, Y. Zhang, Lithium/sulfur batteries with high specific energy: old challenges and new opportunities, Nanoscale, **5**, 2186 (2013).
19. X. Ji, K. T. Lee, L. F. Nazar, A highly ordered nanostructured carbon-sulphur cathode for lithium-sulphur batteries, Nat. Mater., **8**, 500 (2009).
20. C. Zu, Y. S. Su, Y. Fu, A. Manthiram, Improved lithium–sulfur cells with a treated carbon paper interlayer, Phys. Chem. Chem. Phys., **15**, 2291 (2013).
21. S. S. Zhang, Liquid electrolyte lithium/sulfur battery: Fundamental chemistry, problems, and solutions, J. Power Sources, **231**, 153 (2013).
22. S. R. Chen, Y. P. Zhai, G. L. Xu, Y. X. Jiang, D. Y. Zhao, J. T. Li, L. Huang, S. G. Sun, Ordered mesoporous carbon/sulfur nanocomposite of high performances as cathode for lithium–sulfur battery, Electrochim. Acta, **56**, 9549 (2011).
23. J. Schuster, G. He, B. Mandlmeier, T. Yim, K. T. Lee, T. Bein, L. F. Nazar, Spherical Ordered Mesoporous Carbon Nanoparticles with High Porosity for Lithium–Sulfur Batteries, Angew. Chem. Int. Ed. Engl., **51**, 3591 (2012).
24. J. Song, T. Xu, M. L. Gordin, P. Zhu, Y. B. Jiang, Y. Chen, Y. Duan, D. Wang, Nitrogen-doped Mesoporous carbon promoted chemical adsorption of sulfur and fabrication of high-Areal-capacity sulfur cathode with exceptional cycling stability for lithium-sulfur batteries, Adv. Funct. Mater., **24**, 1243 (2014).
25. Y. S. Su, A. Manthiram, Lithium–sulphur batteries with a microporous carbon paper as a bifunctional interlayer, Nat. Commun., **3**, 1 (2012).
26. Y. S. Su, A. Manthiram, A new approach to improve cycle performance of rechargeable lithium–sulfur batteries by inserting a free-standing MWCNT interlayer, Chem. Commun., **48**, 8817 (2012).
27. X. Wang, Z. Wang, L. Chen, Reduced graphene oxide film as a shuttle-inhibiting interlayer in a lithium–sulfur battery, J. Power Sources, **242**, 65 (2013).
28. S. H. Chung, P. Han, R. Singhal, V. Kalra, A. Manthiram, Electrochemically Stable Rechargeable Lithium-Sulfur Batteries with a Microporous Carbon Nanofiber Filter for Polysulfide, Adv. Energy Mater., **5**, 1 (2015).
29. S. H. Chung, A. Manthiram, A natural carbonized leaf as polysulfide diffusion inhibitor for high-performance lithium-sulfur battery cells, Chem. Sus. Chem., **7**, 1655 (2014).
30. J. Song, Z. Yu, T. Xu, S. Chen, H. Sohn, M. Regula, D. Wang, Flexible freestanding sandwich-structured sulfur cathode with superior performance for lithium– sulfur batteries, J. Mater. Chem. A, **2**, 8623 (2014).
31. J. Wang, Y. Yang, F. Kang, Porous carbon nanofiber paper as an effective interlayer for high-performance lithium-sulfur batteries, Electrochem. Acta, **168**, 271 (2015).
32. R. Singhal, S. H. Chung, A. Manthiram, V. Kalra, A free-standing carbon nanofiber interlayer for high-performance lithium-sulfur batteries, J. Mater. Chem. A, **3**, 4530 (2015).

33. J. Balach, T. Jaumann, M. Klose, S. Oswald, J. Eckert, L. Giebeler, Mesoporous carbon interlayers with tailored pore volume as polysulfide reservoir for high-energy lithium - Sulfur batteries, J. Phys. Chem. C, **119**, 4580 (2015).
34. S. H. Chung, A. Manthiram, A hierarchical carbonized paper with controllable thickness as a modulable interlayer system for high performance Li-S batteries, Chem. Commun., **50**, 4184 (2014).
35. J. Q. Huang, Z. L. Xu, S. Abouali, M. Akbari Garakani, J. K. Kim, Porous graphene oxide/carbon nanotube hybrid films as interlayer for lithium-sulfur batteries, Carbon, **99**, 624 (2016).
36. Z. Zhang, G. Wang, Y. Lai, J. Li, A freestanding hollow carbon nanofiber/reduced graphene oxide interlayer for high-performance lithium-sulfur batteries, J. Alloys and Compounds, **663**, 501 (2016).
37. Z. Cao, C. Ma, Y. Yin, J. Zhang, Y. Ding, M. Shi, S. Yang, Carbonized non-woven fabric films as adsorbing interlayers to enhance electrochemical performance of lithium–sulfur batteries, New J. Chem., **39**, 9659 (2015).
38. Y. S. Su, Y. Fu, B. Guo, S. Dai, A. Manthiram, Fast, reversible lithium storage with a sulfur/long-chain-polysulfide redox couple, Chem. Eur. J., **19**, 8621 (2013).
39. L. Qie, C. Zu, A. Manthiram, A High Energy Lithium-Sulfur Battery with Ultrahigh-Loading Lithium Polysulfide Cathode and its Failure Mechanism, Adv. Energy Mater., **6**, 1 (2016).
40. J. Y. Hwang, H. M. Kim, S. K. Lee, J. H. Lee, A. Abouimrane, M. A. Khaleel, I. Belharouak, A. Manthiram, Y. K. Sun, High-Energy, High-Rate, Lithium-Sulfur Batteries: Synergetic Effect of Hollow TiO2-Webbed Carbon Nanotubes and a Dual Functional Carbon-Paper Interlayer, Adv. Energy Mater., **6**, 1 (2016).
41. J. Balach, T. Jaumann, M. Klose, S. Oswald, J. Eckert, L. Giebeler, Functional Mesoporous Carbon-Coated Separator for Long-Life, High-Energy Lithium-Sulfur Batteries, Adv. Funct. Mater., **25**, 5285 (2015).
42. H. J. Peng, D. W. Wang, J. Q. Huang, X. B. Cheng, Z. Yuan, F. Wei, Q. Zhang, Janus Separator of Polypropylene-Supported Cellular Graphene Framework for Sulfur Cathodes with High Utilization in Lithium–Sulfur Batteries, Adv. Sci. **3**, 1500268 (2016).
43. J. Balach, T. Jaumann, M. Klose, S. Oswald, J. Eckert, L. Giebeler, Improved cycling stability of lithium-sulfur batteries using a polypropylene-supported nitrogen-doped mesoporous carbon hybrid separator as polysulfide adsorbent, J. Power Sources. **303**, 317 (2016).
44. Y. Qu, Z. Zhang, X. Zhang, G. Ren, Y. Lai, Y. Liu, J. Li, Highly ordered nitrogen-rich mesoporous carbon derived from biomass waste for high-performance lithium–sulfur batteries, Carbon, **84**, 399 (2015).
45. L. B. Xing, K. Xi, Q. Li, Z. Su, C. Lai, X. Zhao, R. V. Kumar, Nitrogen, sulfur-codoped graphene sponge as electroactive carbon interlayer for high-energy and -power lithium-sulfur batteries, J. Power Sources. **303**, 22 (2016).
46. P. Bruce, S. Freunberger, L. Hardwick, J. M. Tarascon, Li-O2 and Li-S batteries with high energy storage, Nat. Mater., **11**, 19 (2011).

47. L. Fu, G. Qi, R. Sahore, R. Sougrat, F. J. DiSalvo, E. P. Giannelis, Facile synthesis and application of a carbon foam with large mesopores, Phys. Chem. Chem. Phys., **15**, 19134 (2013).
48. M. Peng, D. Li, L. Shen, Y. Chen, Q. Zheng, H. Wang, Nanoporous structured submicrometer carbon fibers prepared via solution electrospinning of polymer blends, Langmuir, **22**, 9368 (2006).
49. J. E. Panels, J. Lee, K. Y. Park, S. Y. Kang, M. Marquez, U. Wiesner, Y. L. Joo, Synthesis and characterization of magnetically active carbon nanofiber/iron oxide composites with hierarchical pore structures, Nanotechnology, **19**, 455612 (2008).
50. Z. Zhang, X. Li, C. Wang, S. Fu, Y. Liu, C. Shao, Polyacrylonitrile and Carbon Nanofibers with Controllable Nanoporous Structures by Electrospinning, Macromol. Mater. Eng., **294**, 673 (2009).
51. L. Ji, A. J. Medford, X. Zhang, Fabrication of Carbon Fibers with Nanoporous Morphologies from Electrospun Polyacrylonitrile/Poly (L -lactide) Blends, J. Polym. Sci. Part B Polym. Phys., **47**, 493 (2008).
52. A. Greiner, J. H. Wendorff, Electrospinning: a fascinating method for the preparation of ultrathin fibers, Angew. Chem. Int. Ed. Engl., **46**, 5670 (2007).
53. X. Yu, H. Xiang, Y. Long, N. Zhao, X. Zhang, J. Xu, Preparation of porous polyacrylonitrile fibers by electrospinning a ternary system of PAN/DMF/H2O, Mater. Lett., **64**, 2407 (2010).
54. M. S. Rahaman, F. Ismail, A. Mustafa, A review of heat treatment on polyacrylonitrile fiber, Polym. Degrad. Stab., **92**, 1421 (2007).
55. S. Moon, J. Choi, R. J. Farris, Highly porous polyacrylonitrile/polystyrene nanofibers by electrospinning, Fibers Polym., **9**, 276 (2008).
56. A. Rosenman, R. Elazari, G. Salitra, E. Markevich, D. Aurbach, A. Garsuch, The Effect of Interactions and Reduction Products of LiNO3, the Anti-Shuttle Agent, in Li-S Battery Systems, J. Electrochem. Soc., **162**, A470 (2015).
57. K. Nayani, H. Katepalli, C. S. Sharma, A. Sharma, S. Patil, R. Venkataraghavan, Electrospinning combined with nonsolvent-induced phase separation to fabricate highly porous and hollow submicrometer polymer fibers, Ind. Eng. Chem. Res., **51**, 1761 (2012).
58. K. Okada, M. Nandi, J. Maruyama, T. Oka, T. Tsujimoto, K. Kondoh, H. Uyama, Fabrication of mesoporous polymer monolith: a template-free approach, Chem. Commun., **47**, 7422, (2011).
59. S. Cheon, K. Ko, J. Cho, S. Kim, E. Chin, H. T. Kim, Rechargeable Lithium Sulfur Battery: II. Rate Capability and Cycle Characteristics, J. Electrochem. Soc., **150**, A800 (2003).
60. Z. Deng, Z. Zhang, Y. Lai, J. Liu, J. Li, Y. Liu, Electrochemical Impedance Spectroscopy Study of a Lithium/Sulfur Battery: Modeling and Analysis of Capacity Fading, J. Electrochem. Soc., **160**, A553 (2013).
61. M. Rao, X. Song, E. J. Cairns, Nano-carbon/sulfur composite cathode materials with carbon nanofiber as electrical conductor for advanced secondary lithium/sulfur cells, J. Power Sources, **205**, 474 (2012).

CHAPTER 4

Metal Oxide Coatings on Carbon Electrodes with Large Mesopores for Deeply Charged Zinc Bromine Redox Flow Batteries

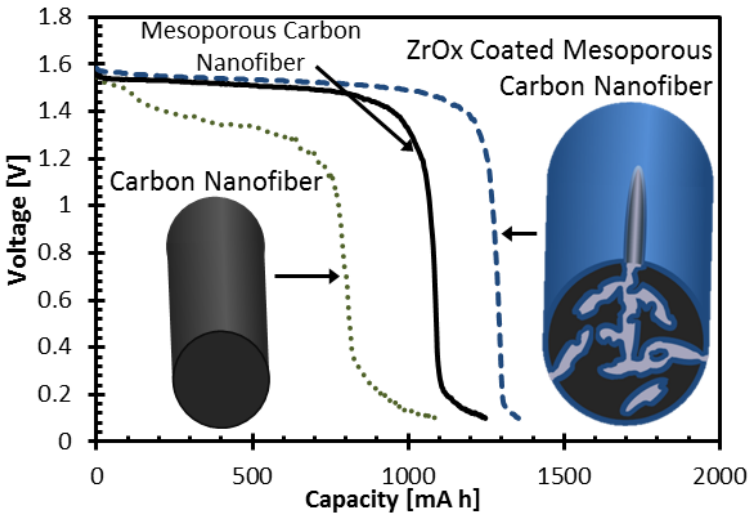

Abstract

Carbon nanofibers with three sizes of large mesopores were made and tested as a cathode material for zinc bromine redox flow batteries. The largest mesopores showed improvements over activated carbon in coulombic efficiency and well as in rate capabilities to 30mA/cm^2. Afterwards, the mesoporous carbon nanofibers are coated with four amorphous metal oxides formed from precursors to form a protective coating and their protective nature is examined in deep and shallow charges. The effect of the coating on battery performance is then analyzed through galvanostatic testing, cyclic voltammetry, and electrochemical impedance spectroscopy. It is determined that the metal oxide coatings improved performance by adsorbing the bromine complex more strongly while the large mesopores aide performance from a combination of adsorption and quicker diffusion.

1. Introduction

In recent years redox flow batteries (RFBs) are growing in popularity as a means to store electrical energy for large scale applications.[1-5] The active materials in RFBs are soluble in the electrolyte so they can be stored in external tanks and pumped into the cell when needed from a closed loop.[1-5] Grid scaled applications such as storing intermittent renewable energy sources and diminishing the peak-demand power generation requirements are considering RFBs for their potentially high overall capacity to store energy. Creating the large capacity needed for these applications with RFBs at the appropriate scale is predicted to be more cost effective than traditional methods.[1-6] Using external storage tanks is advantageous towards scaling up capacity because traditional batteries, where the active materials are stored on or around the electrode, are subject to volume changes and diffusion limitations for active material storage.[1-4] In a RFB the overall capacity scales with the volume of electrolyte and thus the size of the storage tank.[1-4] External storage would also limit potential self-discharge and limit runway reactions, in the event of a failure, to the material remaining in the cell.[4] RFBs are known to have lower energy densities compared to Li ion and other battery technologies, but the grid based applications pursuing RFBs would be stationary applications so large volumes and weights are acceptable.[2-5] However, at the current time RFBs are not cost effective enough to more mature, low risk technologies, and a large proportion of that is due the capital costs for the cell.[1-5,7]

In particular, zinc bromine redox flow batteries (ZBB) are a form of hybrid flow batteries being considered for grid scale energy storage due to its relatively high discharge voltage, inexpensive and abundant active materials, ambient operating temperature, and aqueous electrolyte.[1,8-11] During charging in a ZBB, Zn^{2+} cations from aqueous zinc bromide are reduced to zinc metal at the anode and the Br^{-} anions are oxidized to elemental bromine.[1,8-11] Typically in

modern systems, quaternary ammonium bromide salts then complex with the bromine which phase separates from the aqueous phase to reduce the volatility of the bromine and minimize self-discharge from bromine diffusion through the membrane to the zinc anode.[13-17] Unlike a pure RFB, the zinc metal is stored on the electrode though the bromine complex is removed with the flow.[1,3] A typical working current density for a ZBB is about 20mA/cm^2.[8,10,12] In a simple setup the cathode is coated with activated carbon or connected to carbon felt to increase the surface area of the electrode to aid the sluggish kinetics of bromine.[8,10-12,18] Br^- adsorption and desorption are thought to be the rate limiting steps and thus are primarily the focus of research.[7,19-21] However recent work has also considered the zinc plating aspects such as the effect of the complexing agent, zinc bromine purity, and the supporting electrolyte on plating quality.[22-25] Like other RFBs, to charge and discharge at the desired currents with low overpotentials, the area of the electrode of the ZBB cell is increased by constructing larger cells leading to higher capital costs. Because of the corrosive bromine environment, carbon and graphite are the traditional but more costly materials of choice.[18]

While appreciably conductive and acceptably chemically inert, the cost of machining and producing graphite electrodes is a near unchangeable barrier to lowering costs. One common strategy is to replace the graphite plate electrode with a less expensive conductive carbon plastic composite.[10-11,18,26-27] In addition to carbon plastic, another common strategy would be to modify the electrode's surface such as adding activated carbon to increase surface area.[10-11,18,26] Likewise a more reactive surface could be used to reduce overpotentials and thus increase the effective usable current density to reach higher charge rates with the same spatial area for the cell.[5] Initial attempts to do so include functionalizing the carbon surface with oxygen containing functional groups with acid and air.[18] More recently, single wall and multiple wall carbon nanotubes and

mesoporous carbon have been shown to increase the reactivity of the surface and the surface area respectively.[21,28-29] Mesopores carbons (2-50nm) are useful in a heterogeneous reaction surface because the pores are large enough to prevent diffusion limitations unlike micropores but still have relatively large surface areas.[30-33] Macroporous carbon cyrogels have also been tested which have to report to increase bromine storage in a no flow scenario.[33]

In this report hierarchical pores were created within a macroporous carbon nanofiber mat with large mesopores (>10nm) and micropores within the fibers. Previous work by C. Wang *et al.*[21] implemented small mesopores (2-10nm) for zinc bromine batteries, but large mesopores, which have been shown to beneficial in other applications such lithium sulfur batteries,[34] supercapacitors,[35] and supports for catalysts and adsorbents,[36-37] are thought to be helpful towards accommodating the bulky bromine complex. While the bromine and complexing agent themselves such as 1-ethyl-1-methylpyrrolidinium bromide, are small molecules they are known to phase separate which would need to overcome a surface tension factor in water to fit in a small pore. Work by J. Yang *et al.* showed that using a surfactant to break the complex phase into smaller domains improved performance.[38] Increasing the size pore with large mesopores may have similar effect. In addition to examining the rate capabilities and coulombic efficiencies of cathodes with large mesopores through galvanostatic testing, this work also investigates the effect of adding metal oxide coatings on the carbon. Coatings were added to prevent the degradation of the carbon electrode, which is thought to be a potential problem over many cycles and in deep charging conditions. Alternatively, the coating is desired to prevent side reactions with the complexing agent at higher voltages which may occur at high current densities or in deep charges. Short 1000 cycle galvanostatic experiments along with cyclic voltammetry and electrochemical impedance spectroscopy were conducted to investigate the degradation,

adsorption, and catalytic effects with metal oxide coatings. Finally, the effects of large mesopores and metal oxides coatings were observed together.

2. Materials and Methods

2.1 Carbon Nanofibers with Large Mesopores

Polyacrylonitrile (PAN) (M_w=150,000 from Sigma Aldrich) and cellulose diacetate (CDA) (M_n= 50,000, 39.7% acetyl from Sigma Aldrich) was dissolved in dimethylformamide (DMF) to 12.9wt% polymer in a 1:1 ratio of PAN to CDA. The solution was vortexed until fully mixed, and was electrospun immediately at 19kV, 20 cm distance to the collector, and a 0.02mL/min polymer flowrate with an 18 gauge stainless steel needle. The spinning took place in a humidity controlled box which was necessary for consistency. Control of the humidity was used a mechanism to make adjustments to the size of the mesopores.

The spun nanofibers were peeled from the collector and heat treated in air between two ceramic plates at 270°C for 1 hr with a ramp rate of 1°C/min to stabilize the PAN component of the fibers. The fibers were then placed in a nitrogen filled tube furnace at 1000°C for 8 hours with a ramp rate of 10°C/min to carbonize the PAN component and remove the CDA component by thermal degradation to create mesoporous carbon nanofibers (MPCNF). Macropores through the nanofiber mat exist naturally as the micron sized spaces between the fibers. Micropores were added to the fibers by heat treatment in air at 350°C for four hours for all fibers. Approximately ~5% burn off was achieved to complete the hierarchical pore system with the micropores. The plates were necessary to prevent curling of the fiber mat during stabilization, and the carbonization treatment was done for eight hours to improve conductivity. The surface area and pore size distribution analysis was performed on a Micromeritics Gemini VII 2390t in liquid nitrogen with the Brunauer, Emmett and Teller (BET), t-plot, and Barrett-Joyner-Halenda (BJH)

methods. Samples were degassed under nitrogen at 300°C for at least 3 hours. More details on the creation and characterization through scanning and transmission electron microscopy, BET, and BJH for the nanofibers were released in a recent publication on lithium sulfur carbon interlayers.[39]

2.2 Electrode and Cell Assembly

Samples were attached to a machined graphite electrode with a binding solution. The binder solution, which was 4wt% polyvinylidene fluoride (from Sigma Aldrich M_w=534,000), 2wt% Super P (conductive carbon black additive from TIMCAL) and 94wt% 1-methyl-2-pyrrolidone (NMP), was sonicated for at least 3 hours. After which it was poured on a graphite plate and spread to a thickness of 20 μm with a doctor's blade. The MPCNF samples were placed on the binding solution film and were allowed to dry at 80°C overnight. The sample area was then cut to a 5cm x 7cm rectangle (~.15g) and the excess material was removed. Activated carbon (AC) samples were prepared in a similar way. A solution that was 24wt% AC, 4wt% PVDF, and 72wt% NMP was cast to a 50 μm thickness on the graphite plate and allowed to dry. No Super P binder solution was used.

The overall cell assembly is similar to that depicted in several previous works with a single cell and two reservoirs for electrolyte.[10,16] Flow comes through a hole in the endplate and electrode to a machined flow channel plate where electrolyte flows across the active material in between the electrode and the membrane and then back out. Flow was generated by a dual head peristaltic pump using Tygon tubing. The distance between the electrodes was 4.5mm. Each reservoir contained 75 mL of electrolyte. Each glass reservoir drained from the bottom to capture as much complex as possible. The membrane was a silica filled polyethylene microporous Asahi SF-600 membrane.

Samples with metal oxides had the coating added after activation but before being adhered to the electrode. The coatings were formed from a ~15wt% precursor solution of alkyl carboxylic acid metal salts in a ~2:1 mixture of 1-methoxy-2-propanol acetate and 1-methoxy-2-propanol solvent from EMD Performance Materials. The precursor creates an amorphous metal oxide film when heat treated to the appropriate temperature as described in a work by Padmanaban *et al.*[40] The four metal oxides considered were ZrO_x, TiO_x, WO_x, and AlO_x and were heat treated for an hour in air at 250°C, 250°C, 350°C, and 350°C respectively. Samples that were diluted to obtain thinner coatings were diluted with the mixed solvent.

2.3 Electrochemical Testing

Galvanostatic tests were conducted on a system with a 10 A, 50V maximum from MTI, Corporation. The cell was oriented with the electrode plates in the vertical axis and oriented so complex would not drain into the tubing leading to the cell from gravity. The flow rate was 2mL/sec., and the tubing size was ¼ in. For all current densities, the battery was charged to 40mA h cm^{-2} with 35cm^2 of active material or 1400mA h. All capacity data shown is from the second cycle since a significant proportion of the bromine complex is lost from coating the tubing and glass reservoirs during the first cycle. The electrolyte was 2.25 M zinc bromide, 0.5 M zinc chloride, 0.8 M 1-ethyl-methylpyrrolidinium bromide, and 0.1 M hydrochloric acid. For the 1000 cycle tests with a high SOC, the cell was charge to 2.06V with no flow then discharged for 1 minute and then recharged again to 2.06V for 1000 cycles. For the 1000 cycle tests with a low state of charge (SOC), the first cycle was charged at 20mA/cm^2 with no flow to 200mA h (around 20% SOC) so the electrode would be coated in bromine. The battery was then discharged to 1.45V and recharged for 1 minute for 1000 cycles. Fourier transform infrared spectroscopy (FTIR) was performed on the aqueous portion of the electrolyte with a Nicolet

Magna-IR 560 spectrometer equipped with an attenuated total reflection diamond and averaged over at least 64 scans with a deionized water background.

Cyclic voltammetry (CV) and electrochemical impedance spectroscopy (EIS) testing was performed on a Princeton Parastat 4000. The CV testing used a three electrode system with an Ag/AgCl reference electrode using 1M KCl. The working electrode was polished glassy carbon a 3 mm diameter circular end exposed. Samples were punched out to a 3mm diameter disc and attached to the electrode with the binding solution described above using 3µL of solution. For AC samples, about 0.6mg of AC after drying the solution was deposited on the electrode. The counter electrode was a graphite rod. The electrolyte was 0.05 M zinc bromide and 1.0 M perchloric acid. The EIS used a two electrode system using the same working electrode as the CV testing but used the full concentration electrolyte used in battery testing. The distance between electrodes was 12mm and the sample and was tested from 10^5 Hz to 10^{-1} Hz with a 10mV amplitude. When bromine was added to the electrolyte to generate a phase separated bromine complex, 0.1g of bromine was added to 20mL of electrolyte.

3. Results and Discussion

3.1 Effect of Cell Orientation

First, small aspects of the cell assembly were considered for consistency. Most notably, the orientation of the cell mattered significantly. The difference between the vertical and horizontal orientation are shown in Figure 1a-b. Figure 1c shows the difference in the charge and discharge capacity curves for an AC coated electrode produced by Lotte Chemical. From visual observation, the horizontal orientation has better performance because the heavy viscous bromine complex can drain out of the cell and the flow was not quite strong enough to push the complex back into the cell. Also in the horizontal position, some complex would always remain

in contact with the electrode as it sinks to the bottom of the cell below the flow entry points. It is apparent that for discharge the bromine complex phase should be in direct contact with the electrode.

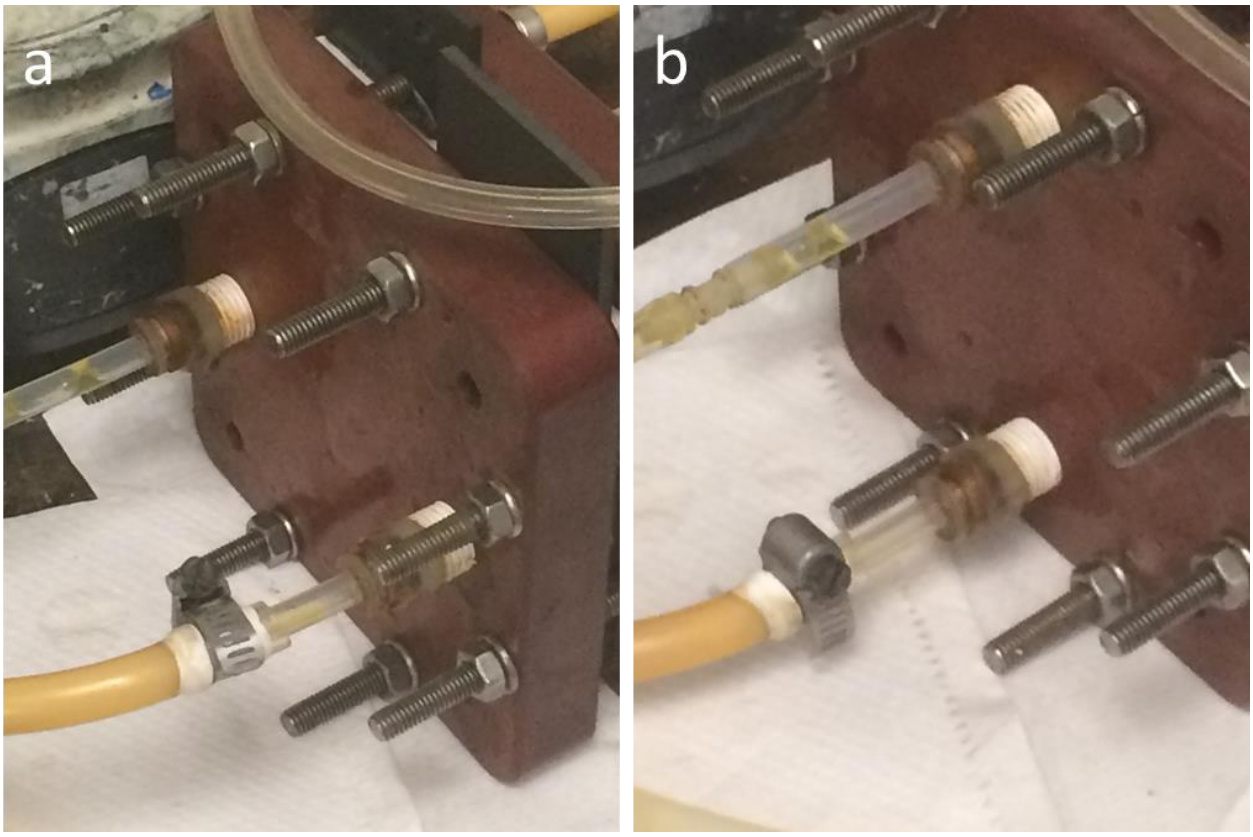

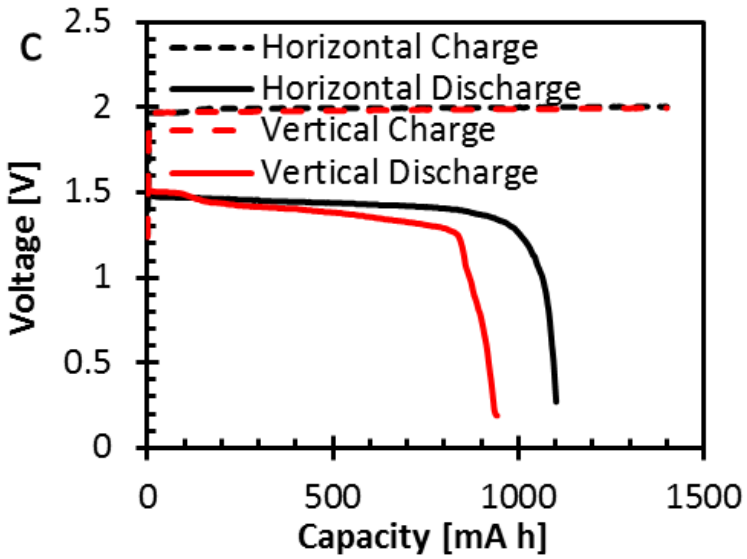

Figure 1: Picture of the ZBB cell in the a) default horizontal position and b) in the vertical position. c) The second cycle charge and discharge capacity vs. voltage for an AC coated electrode charged at 20mA/cm^2 to 1400mA h.

3.2 Effect of Pore Size

Next MPCNF samples were attached to clean graphite electrodes to compare against AC coated electrodes made in the lab with PVDF. The BJH incremental pore volume and pore area distributions of the carbonized and activated PAN CDA MPCNFs electrospun at three different relative humidities (RH) and the "PAN only" nanofibers electrospun at 30% RH are given in Figure 2. Described in more detail in a previous work, large mesopores were created while electrospinning PAN and CDA at high RH such as 50% RH by increasing the thickness of the nanofiber and allowing more time for phase separation until the solvent evaporated. "PAN only" did not contain any significant amount of mesopores as there was no phase separation from the blend and the mesoporosity is not initially created by the humidity.

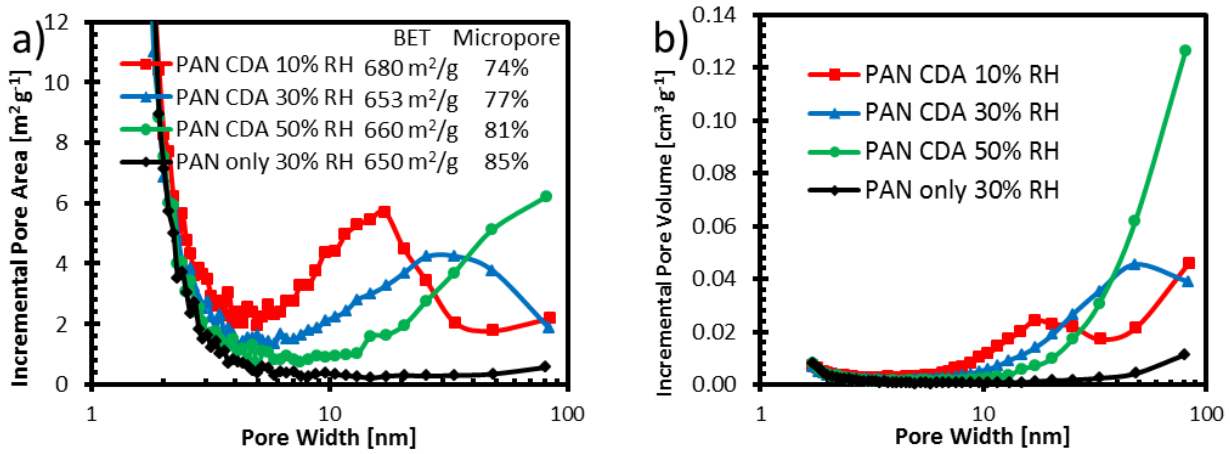

Figure 2: BJH analysis of nitrogen physisorption showing a) the incremental pore area distribution, b) the incremental pore volume distribution.

In Figures 3a, the discharge capacity between AC and 10% RH, 30% RH, and 50% RH MPCNFs, charged to 1400mA h at 20mA/cm^2, are compared. The initial discharge voltage was very similar for the four samples and AC performed well, achieving 71% coulombic efficiency. 30% RH and 50% RH, which contained a peak of 30nm and 50nm+ by area of interconnected pores, had an efficiency of 78% and 88% respectively. Larger mesopores were more effective at 20mA/cm^2. 10% RH was not very effective as a cathode but had the smallest and least interconnected pores. In Figure 3b, the standard activated 30% RH MPCNF sample is compared against 30% RH MPCNFs which had not been activated but still has mesopores and "PAN only" nanofibers which were activated but had no mesopores. The standard 30% RH MPCNF sample performed better than both of them, but at 20mA/cm^2, both micropores and mesopores were useful to improving coulombic efficiency. In Figure 3c, each charge curve with different mesopores and micropores was very similar and overlapped each other. In Figure 3d after the constant current discharge, the anode electrode was stripped by continuing the discharge at the highest possible current until 0.1V was reached. When the stripping is considered, most samples which perform reasonably well have around the same coulombic efficiency at 91%. The samples

which dropped to lower voltages earlier just cannot provide the energy at the desired rate, but most of the energy was not lost except for when diffusion based self-discharge starts to dominate in longer time scales.

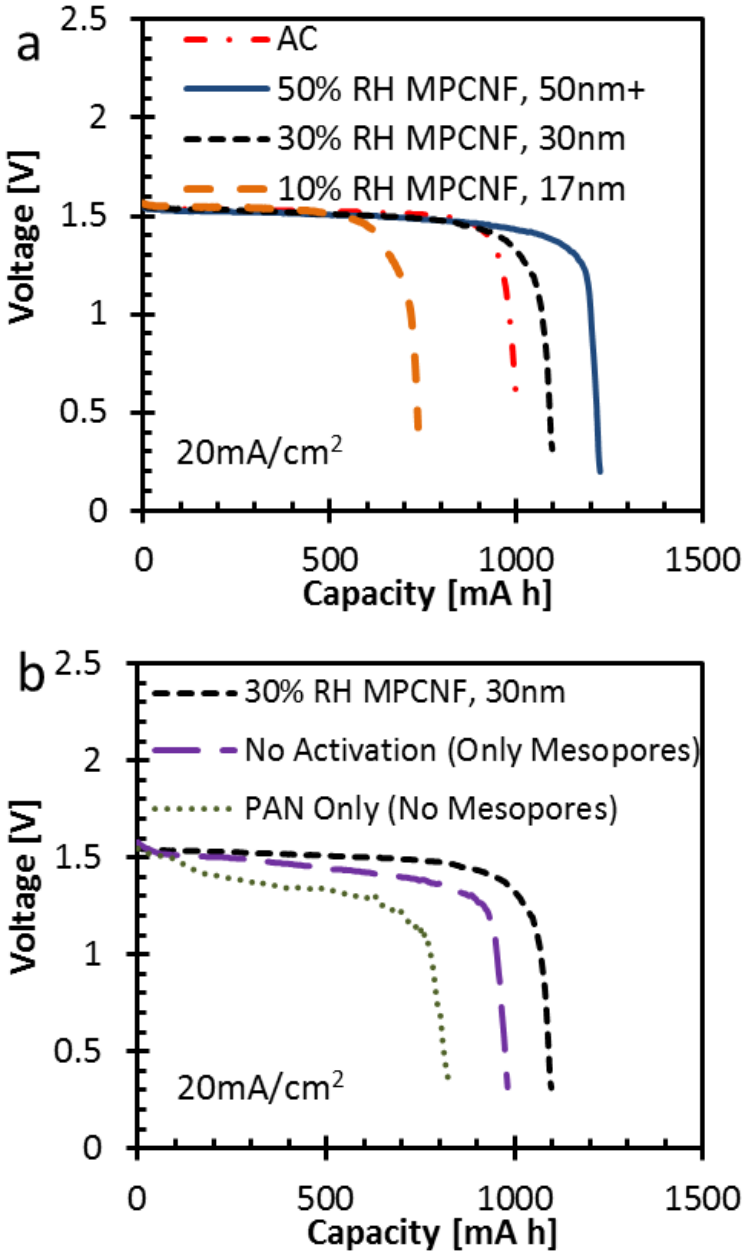

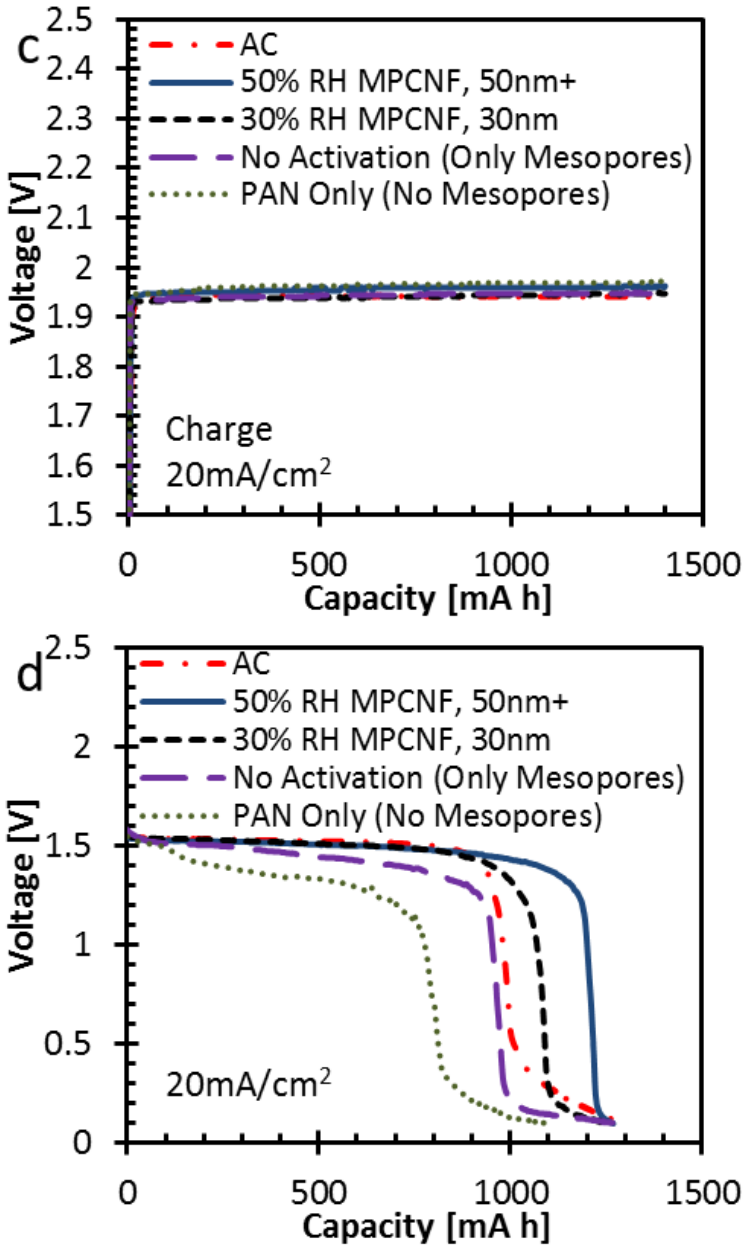

Figure 3: Capacity discharge curves where cells where charged to 1400mA h and discharged at 20mA/cm^2 to a) compare samples spun different relative humidities and AC, b) check the effect of micropores and mesopores. c) Compares the capacity curves during charging. d) After discharging at constant current, samples are stripped at the highest possible current until 0.1V.

In Figure 4, the charge and discharge rate is varied. At 30mA/cm^2, 50% RH performs the best showing little difference between 20 and 30mA/cm^2 except for a 0.1V drop in the discharge

voltage. 10% RH and AC perform the worst but with the stripping, the coulombic efficiency ends up being almost the same. The effectiveness of large mesopores is best observed between the 30%RH sample with 30nm mesopores and the 50% RH with 50nm+ mesopores where the 30% RH sample performs similarly to AC and the 50% RH sample is relatively unchanged. At 10mA/cm^2, samples which did not perform well at higher charge rates, performed much better at discharging at the slower rate.

It is thought that the larger mesopores would better adsorb the phase separated complex so those samples can retain higher concentrations of bromine at the surface and reactive sites to meet the current demands by saturating the sites. If there were diffusion limitations which the mesopores or surface area could affect, it would be expected that there would be a larger change in discharge and charge plateau voltages. During discharge electrodes coated in complex use the complex "stored" in their pores and must then adsorb more from the flow or it will be depleted. If adsorption is not strong enough to replenish the complex, then the voltage would drop from the low concentration at surface though the complex still remains in the electrolyte and would be adsorbed and used eventually. All the MPCNFs had similar surface areas so the number of active reaction sites should be similar. If diffusion to the active sites from the bulk after depletion was the limitation resolved by pores then the charge curves would be affected too, and it would be expected that there would be a smaller difference between 30nm and 50nm pores in 30mA/cm^2 discharge but a larger one between AC micropores and 30nm pores.

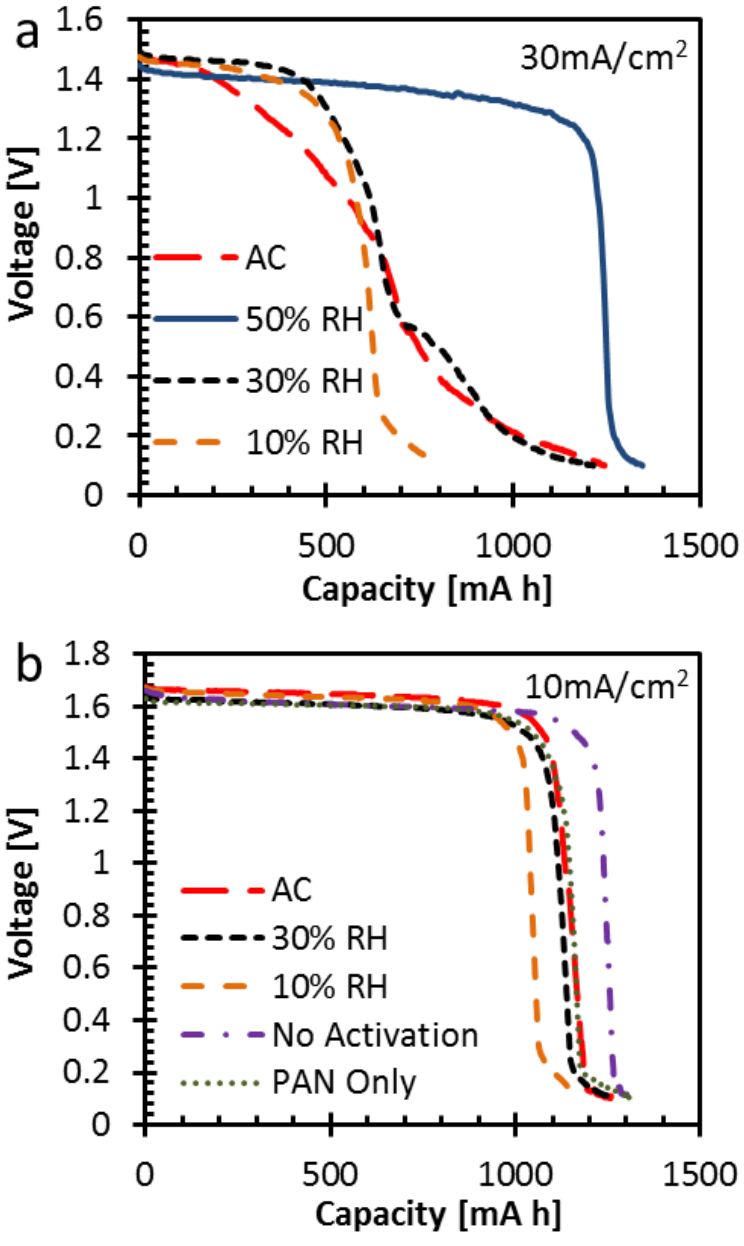
a
30mA/cm2
Voltage [V]
Capacity [mA h]
AC
50% RH
30% RH
10% RH
b
10mA/cm2
Voltage [V]
Capacity [mA h]
AC
30% RH
10% RH
No Activation
PAN Only

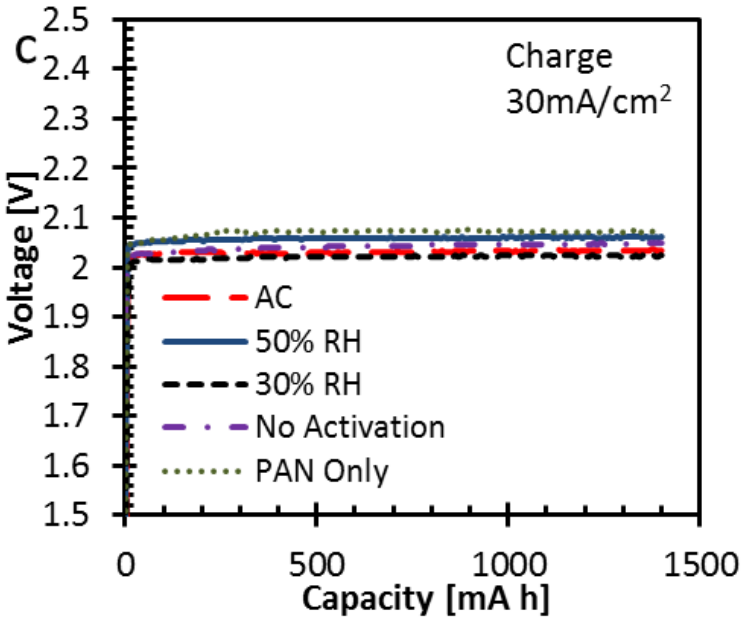

Figure 4: Capacity discharge curves comparing samples charged to 1400mA h and discharged at a) 30mA/cm^2 and b) 10mA/cm^2 with the stripping included. c) Capacity charge curves at 30mA/cm^2 for samples in a) and b).

3.3 Effect of Metal Oxide Coatings

In this section, metal oxide coatings were added to activated 30% RH MPCNF samples and adhered to the electrode. Four metal oxides were tested: ZrO_x, WO_x, TiO_x, and AlO_x. The primarily goal was to create a robust barrier to carbon electrode degradation. It is known that through cycling bromine based batteries, oxygen containing functional groups are added to the surface.[11,29,41] Several reports conclude a slow degradation process with bromine and show evidence of C-Br bonds forming.[11,29,42] First, it was considered what protection the coatings would provide if the battery was charged too deeply, possibly revealing small side reactions with the bromine, bromine complex, and the carbon electrode during deep charges.

In Figure 5a-b, samples were charged to 2.5V at 20mA/cm^2 in a filled but non-flowing cell containing approximately 5 mL of electrolyte. In general MPCNFs and metal oxide coated samples charged for about 1000mA h and would rise in voltage when the last of the $ZnBr_2$ in the

electrolyte is consumed with a slight shoulder. Ideally the voltage should rise smoothly until hydrolysis dominates. The extra unknown capacity source observed in AlO_x is not desired either. For the AC electrode, the voltage jumped to a higher voltage first but has the largest high voltage shelf between 2.2V and 2.4V looking like a peak suggesting a stronger side reaction with the complexing agent. Figure 5c shows absorbance from a FTIR scan where the electrolyte after charging to 2.5V with AC has minimal signal for the complex peaks at 1470cm^{-1} and between 900cm^{-1} and 1200cm^{-1}. This is compared against a used electrolyte which was used for the 20mA/cm^2 AC test in Figure 3 to show that the complexing agent is not damaged by normal cycling. The red line for the complexing agent contained the complex agent by itself in deionized water to indicate the appropriate peaks. ZrO_x coated AC also had stronger complex peaks compared to the uncoated AC. This shows that with the ZrO_x coating on AC, charges can go deeper or at higher current densities without damaging the complexing agent.

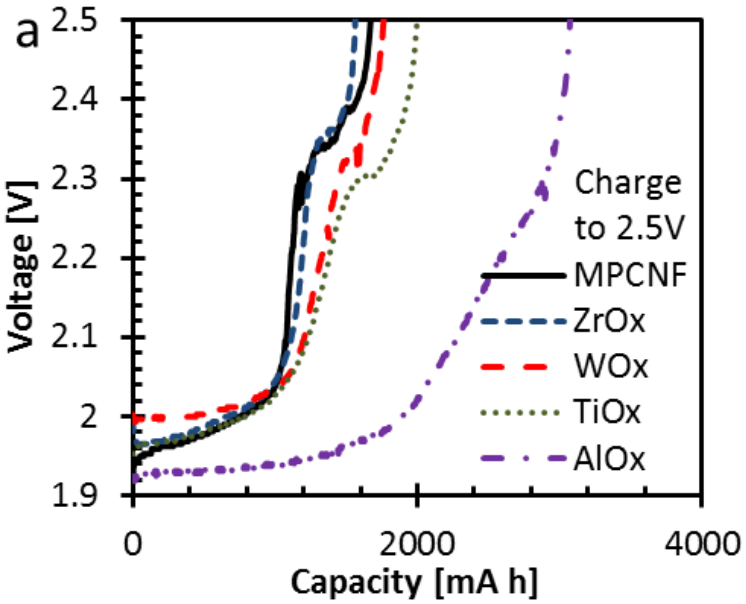

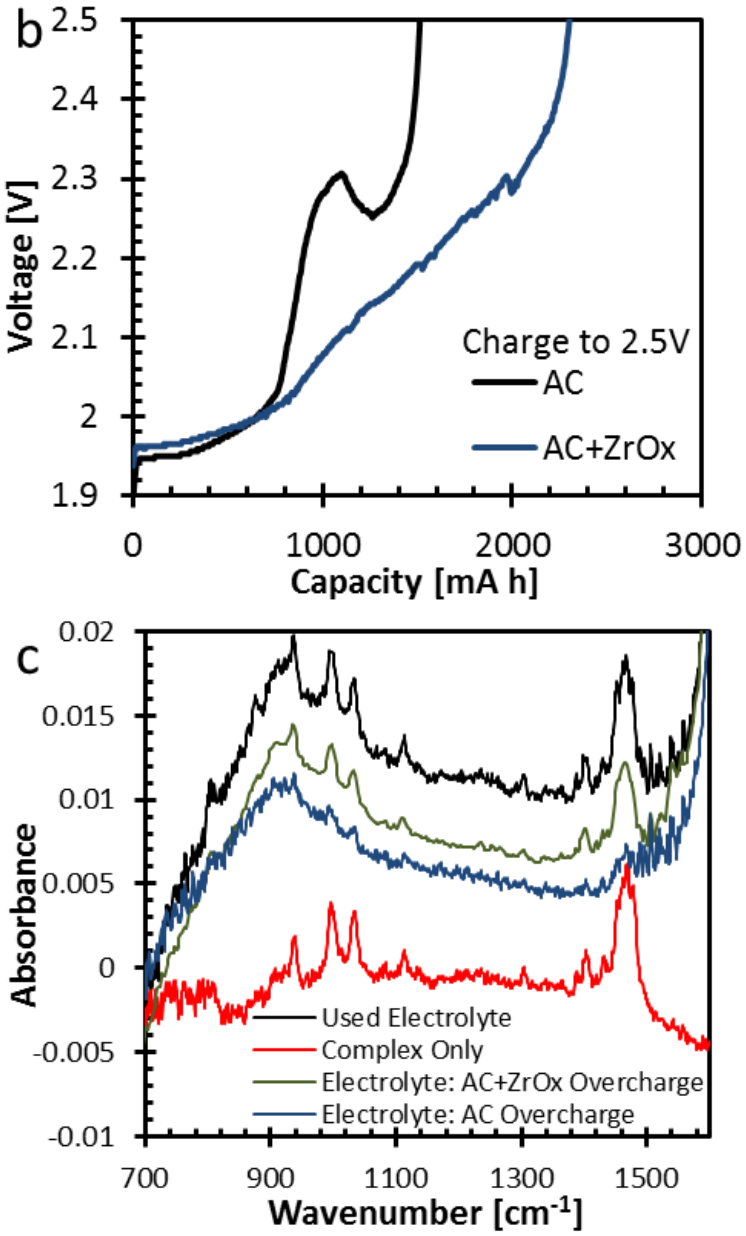

Figure 5: A no flow cell charged to 2.5V at 20mA/cm^2 a) with 30% RH MPCNFs and metal oxide coated 30% RH MPCNFs, and b) with AC and ZrO_x coated AC. c) FTIR of the electrolyte, complex, and electrolyte after charging to 2.5V with the AC sample on a deionized water background.

To test the effect of deep charge cycling with the knowledge of the SOC and voltage from Figure 5a for ZrO_x, WO_x, and TiO_x, the same no flow cell as above was charged to 2.06V and cycled 1000 times at 20mA/cm^2 for each sample. In Figure 6a, the AC carbon sample had a

decline in the initial discharge voltage after 300 cycles which lead to the cell being unable to discharge at the specified rate. When ZrO_x was coated on the AC, no sudden decline in discharge voltage was observed. In Figure 6b, a similar experiment was carried out with 30% RH MPCNF coated with the four metal oxides. After 1000 cycles MPCNFs were starting to show decline and could not discharge at the specified rate while ZrO_x coated MPCNF were not showing any rapid decline in initial discharge voltage. For coulombic efficiency, MPCNF reached about 71% until failure while ZrO_x reached 95% with no failure. AlO_x, TiO_x, and WO_x however all showed rapid decline in voltage. In Figure 5a, ZrO_x and MPCNF performed the most closely together as well. It thought that the decline in voltage in the 1000 cycle study was related to degradation of the electrolyte perhaps with the electrode. As shown in Figure 6c, after replacing the electrolyte and testing the electrode again, the performance was the about the same or better after the 1000 cycles. The other samples were similar in this regard.

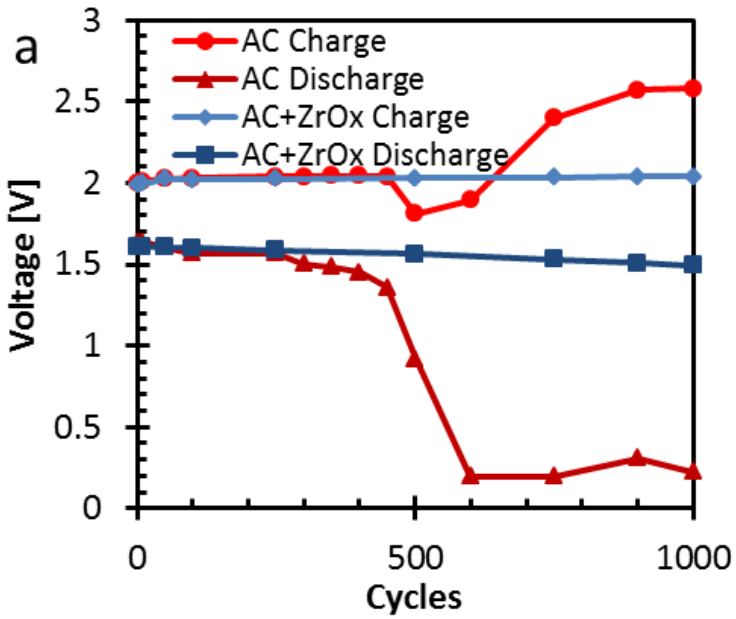

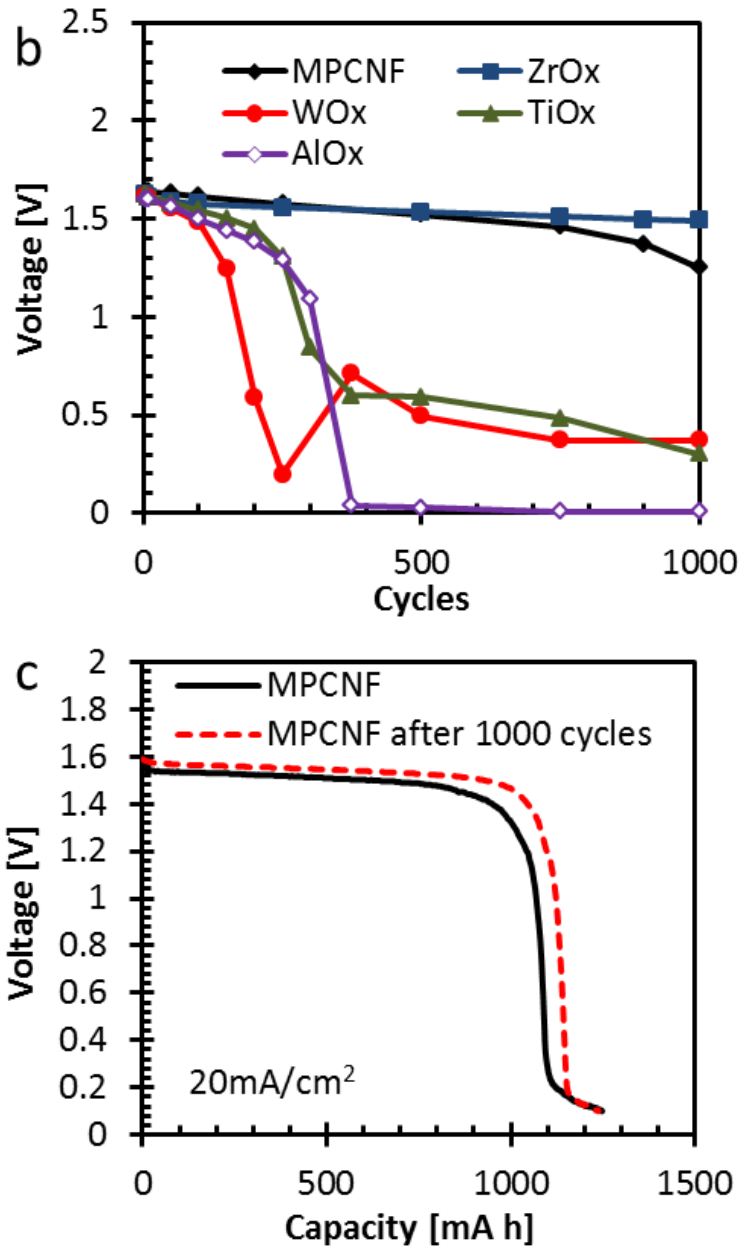

Figure 6: Initial charge and discharge voltages of a) AC and ZrO_x coated AC, and b) metal oxide coated 30% RH MPCNF for 1000 cycles charged to 2.06V and discharged for 1 min at 20mA/cm^2. c) 20mA/cm^2 discharge profile for MPCNF before and after 1000 deep cycles.

To continue exploring the effects of the metal oxides over many cycles, filled cells with no flow were charged 200mA h or about 20% SOC and then cycled 1000 times where the cell discharged to 1.45V and charged for 1minute at 20mA/cm^2. In Figure 7a, AC has only about

67% coulombic efficiency while ZrO_x coated AC was 95%. The inefficiency of AC is not related the disconnected nature of the particles as ground MPCNF, which were MPCNFs that were ground into a powder in a ball mill, did not show a low efficiency like AC. In Figure 7b, 30% RH MPCNFs without and with ZrO_x and WO_x coatings were tested. MPCNFs are not as inefficient as AC despite both being a type of activated carbon. This is perhaps due to different amounts and ratios of oxygen containing surface groups or the mesopores promote better diffusion when the concentration of the electrolyte becomes low from stagnant conditions. After about 300 cycles, both ZrO_x and WO_x obtained similar coulombic efficiencies as the MPCNF.

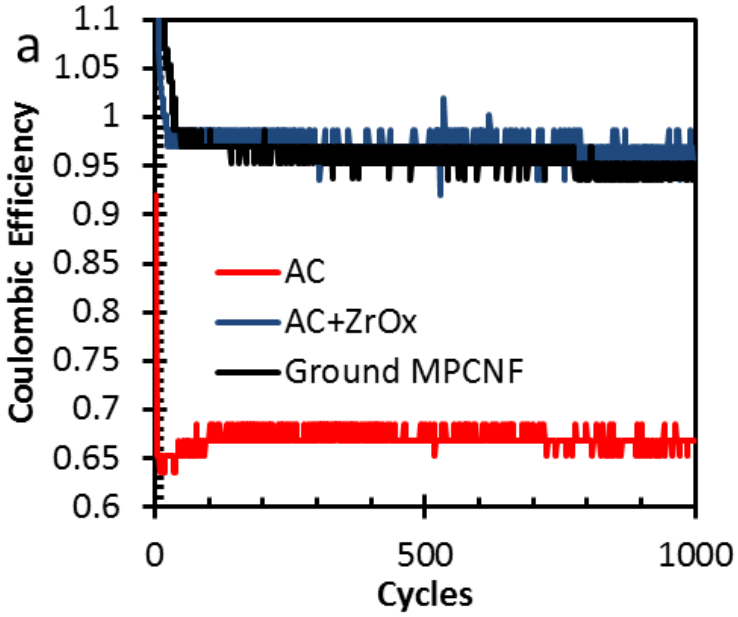

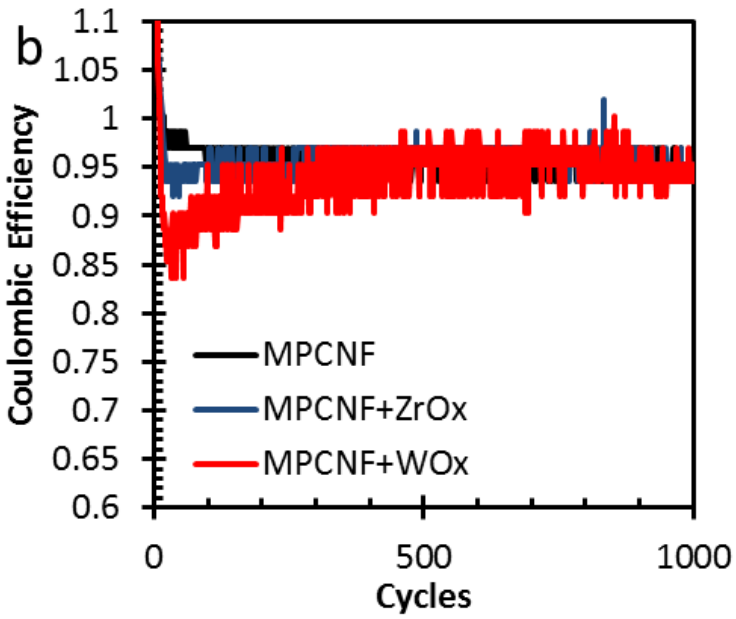

Figure 7: No-flow tests charged to ~20% SOC and then discharged for 1.45V and recharged for 1 minute 1000 times at 20mA/cm^2 for a) AC, ZrO_x coated AC, and ground MPCNF and b) MPCNF, ZrO_x coated MPCNF, and WO_x coated MPCNF.

Next the discharge capacity of the coated MPCNFs and AC are compared in Figure 8 by charging to 1400mA h at 20mA/cm^2 with flow again. Again TiO_x and AlO_x showed poor performance compared to the uncoated MPCNF. AlO_x has its discharge plateau dip down early though it provides the necessary current at a slightly lower voltage, and TiO_x ended with an overall low capacity. ZrO_x did not provide as high of a capacity at the specified current as the uncoated MPCNFs. However WO_x exceeded the performance of the MPCNF despite the fundamental drawback that the WO_x coating provides an additional barrier for charge transfer. ZrO_x coated AC performed roughly the same as AC as well. However, the ZrO_x coating for AC only comprised of about 11wt% of the sample after heat treatment. For the coated MPCNF samples the coating was about a third of the weight of the sample. While AC and MPCNF have similar surface areas per gram, MPCNF samples are light and macroporous so wetting the MPCNF samples with the same concentration of precursor as AC created thicker coatings. The

problem of thick coatings was addressed by diluting the precursor with solvent before dispersing it on the samples.

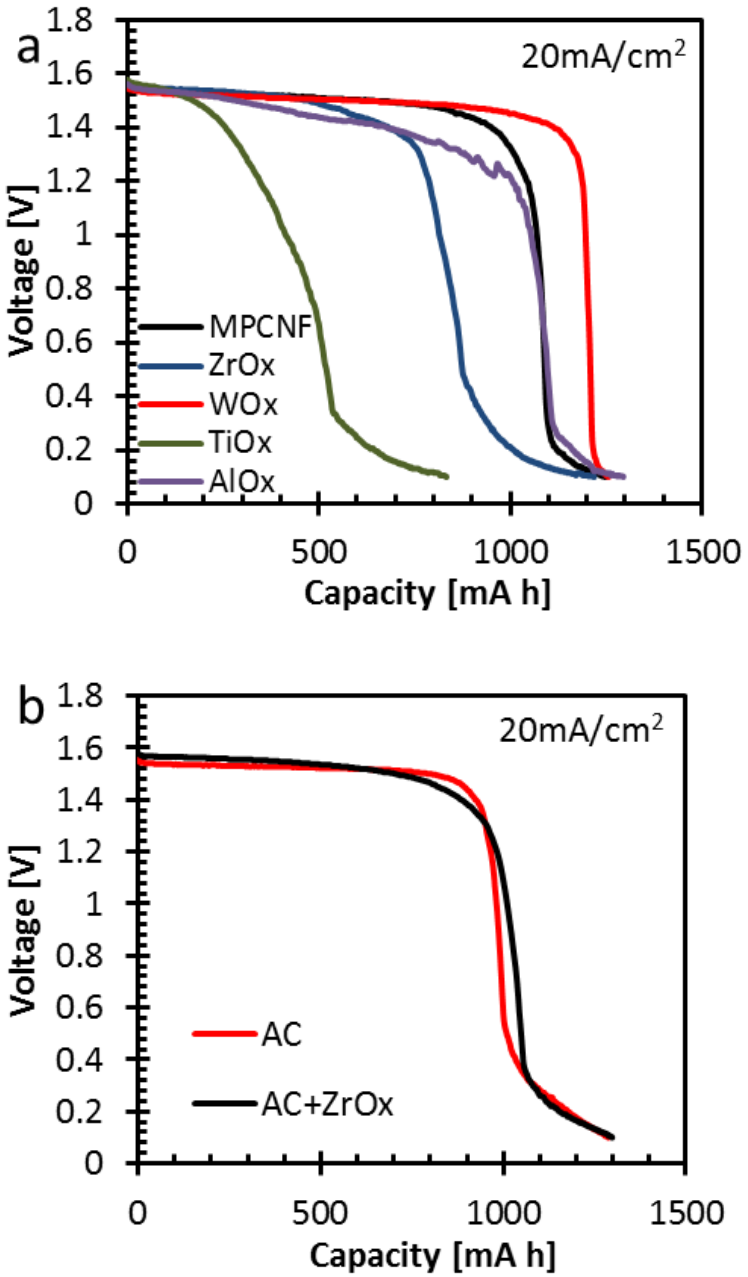

Figure 8: Discharge capacity profiles charged to 1400mA h at 20mA/cm^2 for a) metal oxide coated 30% RH MPCNFs and b) ZrO_x coated AC.

In Figure 9a, 30% RH MPCNF samples were coated with diluted ZrO_x and WO_x precursors and heat treated. At one tenth the concentration of ZrO_x precursor, the coating after heat treatment was only 5wt% of the sample. By decreasing the amount of coating, both ZrO_x and WO_x improved and are better than the original MPCNF. A similar scenario is observed in Figure 9b at 30mA/cm^2 especially for 1/10th WO_x. However, the coatings are not the only factor responsible for the improvement. The 1/10th ZrO_x coated PAN only sample with no mesopores does not perform well either at 30mA/cm^2. Therefore both mesopores and the coatings are used to improve the dischargeable capacity at 30mA/cm^2. In Figure 9c, it is seen that a majority of the mesopores are preserved with 1/10th ZrO_x and WO_x coatings though 1/10th WO_x is closer in pore volume to the original MPCNF. However, for a coated sample to surpass the original performance of the MPCNF, it was thought that the coating must either provide a catalytic or more reactive surface or aides the adsorption of the bromine complex to increase the concentration near the surface. For coated samples, especially WO_x, the performance does not seem strictly related to the pores volume. WO_x with no diluted precursor starts with a low pore volume and only improves only slightly in discharge capacity with significant increases in pore volume while ZrO_x improves significantly in discharge capacity but with little increase in pore volume.

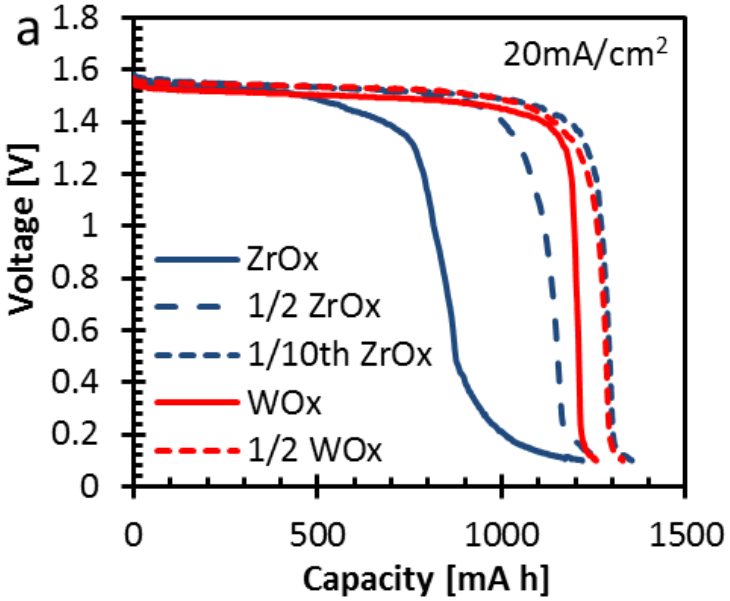
a
20mA/cm2
Voltage [V]
Capacity [mA h]
ZrOx
1/2 ZrOx
1/10th ZrOx
WOx
1/2 WOx
0
0.2
0.4
0.6
0.8
1
1.2
1.4
1.6
1.8
0
500
1000
1500

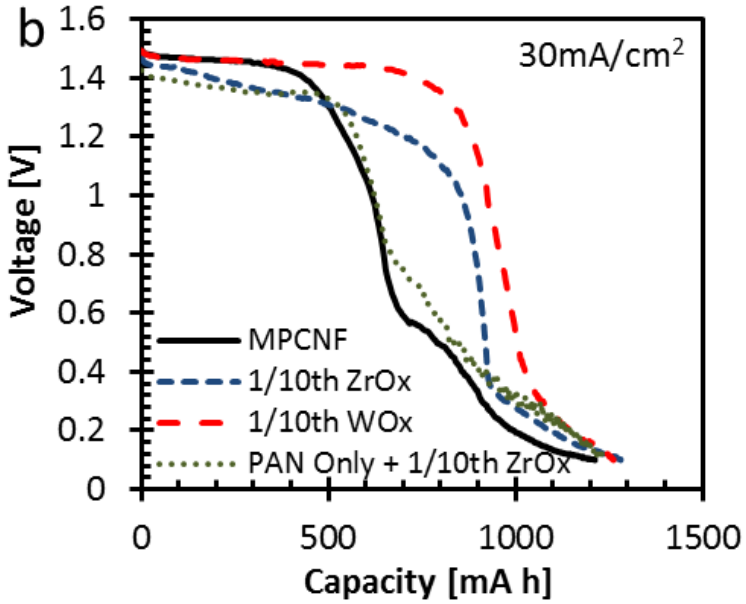
b
30mA/cm2
Voltage [V]
Capacity [mA h]
MPCNF
1/10th ZrOx
1/10th WOx
PAN Only + 1/10th ZrOx
0
0.2
0.4
0.6
0.8
1
1.2
1.4
1.6
0
500
1000
1500

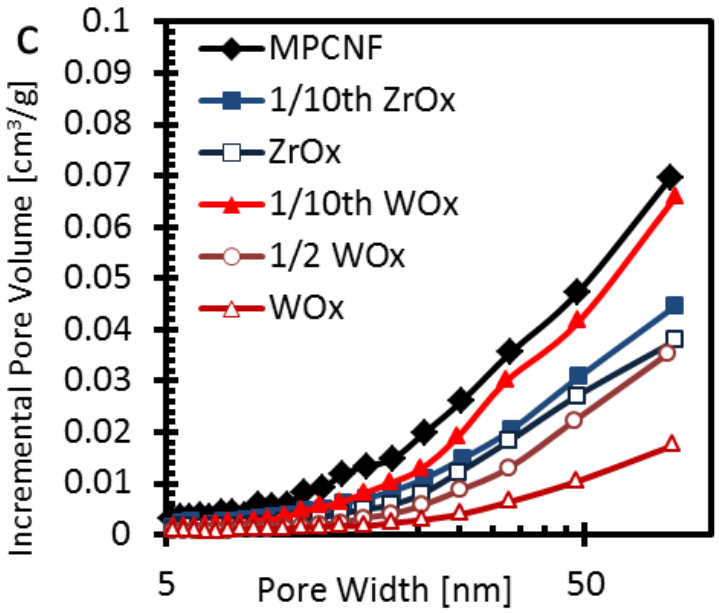

Figure 9: Discharge capacity profiles charged to 1400mA h at 20mA/cm^2 for a) metal oxide coated 30% RH MPCNF and b) ZrO_x coated AC using diluted precursors. c) The incremental pore volume distribution using nitrogen physisorption and BJH method.

To explore the difference in mechanisms, EIS and CV testing was conducted. Figure 10, gives Nyquist plots to compare the impedance of the samples. The charge transfer resistance is taken from the diameter of the semicircles if formed. Small shifts right or left of the semicircle supposedly correspond to small changes in the resistance of the electrolyte.[43] Figure 10a compares difference in impedance when the electrolyte contains bromine and when it does not. The drastic decrease in charge transfer confirms an earlier report by J. Jeon *et al.* where charged bromine complex lowered charge transfer resistance on a activated carbon surface. It was reported that this occured from the complex adsorbing to the surface and directly transfering adsorbed bromine from the complex to the surface.[16] In Figure 10b-d, impedance is seen to decrease with increasing pore size for the samples spun with increasing humidity. The metal oxide coatings lower resistance compared to the 30% RH MPCNF as well despite adding an additional barrier. And by comparing ½ WO_x and 1/10th WO_x, it is seen that a thinner coating has

a smaller resistance as expected. A similar affect is observed for AC and ZrO_x coated AC. Putting together the idea that bromine complex adsorbs to surfaces to lower charge transfer resistance and that the coatings lowered resistance, it is supported that the coating promoted complex adsorption.

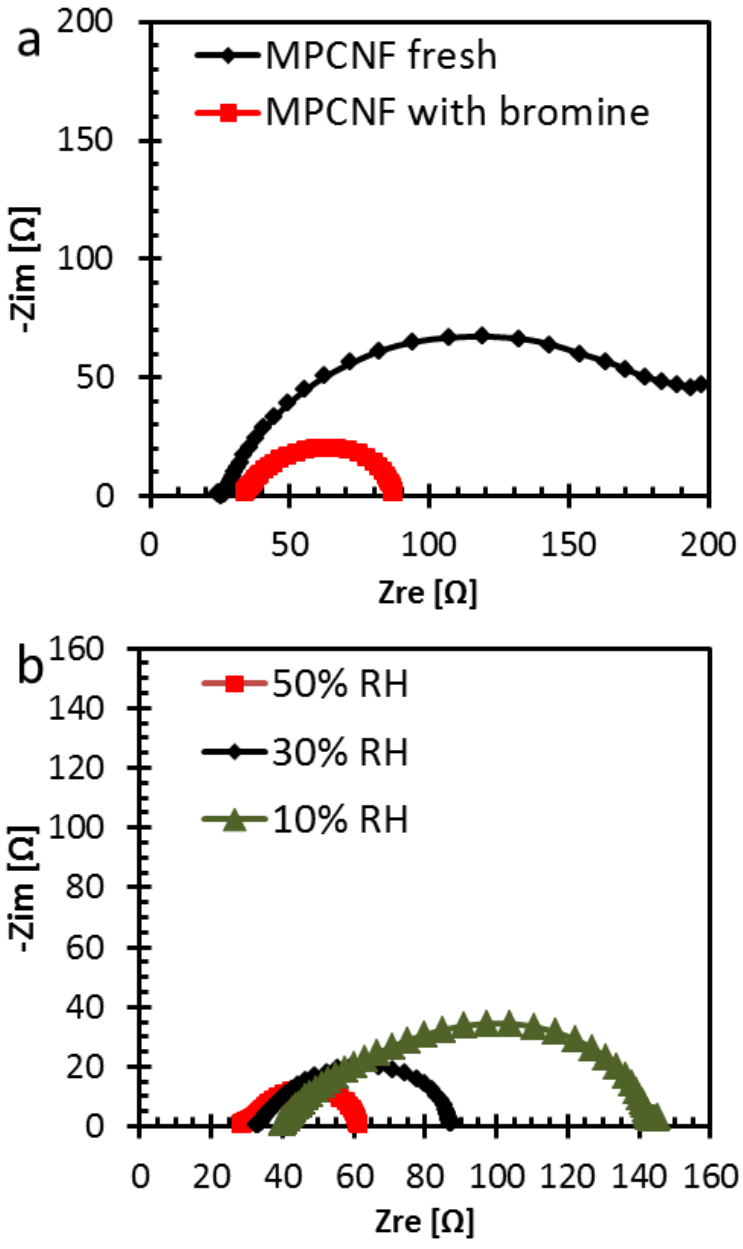

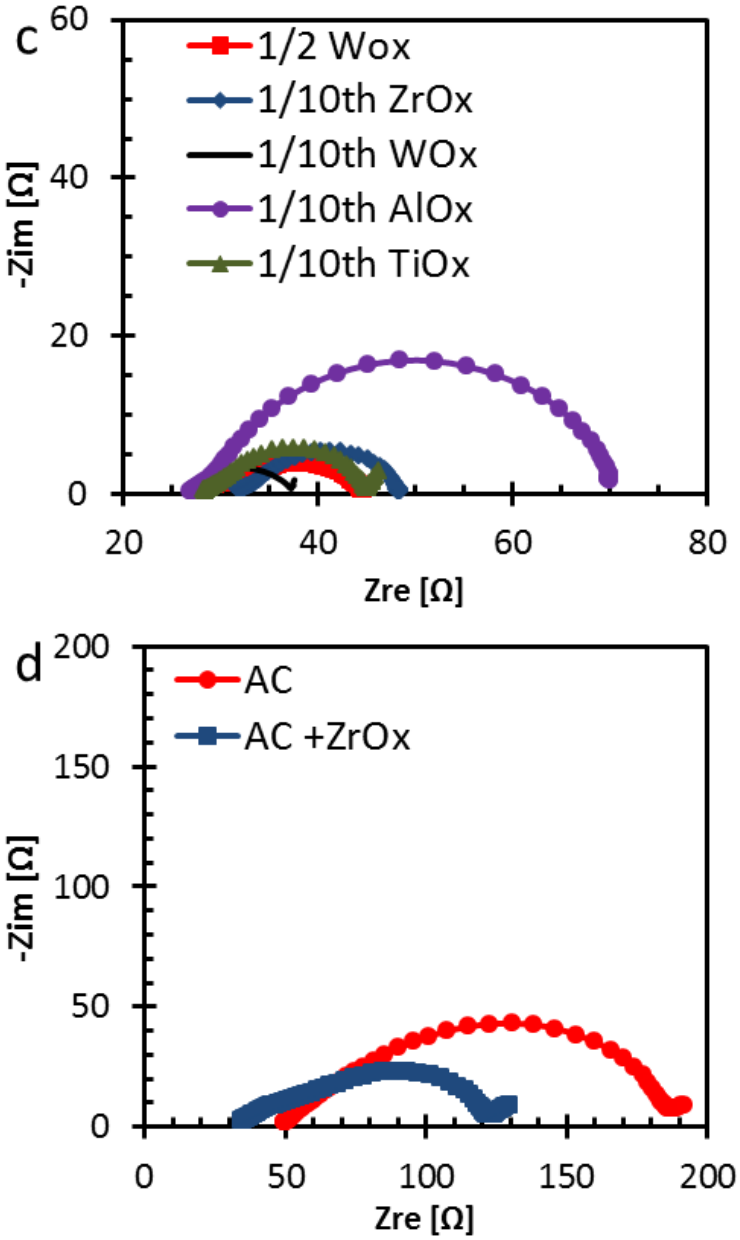

Figure 10: Nyquist plots comparing: a) 30% RH MPCNF with and without bromine, b) MPCNFs spun at 50% RH, 30% RH, and 10% RH, c) metal oxide coated 30% RH MPCNFs with diluted precursors, d) AC and ZrOx coated AC.

Lastly CV tests were considered. Figure 11 compares CV sweeps between 0.05V and 1.4V at 10mV/sec. Both the anodic and cathodic peaks are visible. 50% RH and ½ WO_x have the highest peak currents and a low degree of peak separation. AC, 10% RH, PAN only, and the

Super P binder all perform poorly in these regards. The 1/10th metal oxides perform roughly as well as the base 30% RH MPCNF. Then the scan rate was varied from 5mV/sec to 100mV/sec to compile anodic and cathodic peak currents and separation voltages. According to Randles-Sevcik equation, the peak current should be proportional to square root of the scan rate.[44-45] Assuming approximately constant surface area between samples, the proportionality constant should depend on the bulk concentration or the square root of the diffusion constant. In Figure 12a-b), there are good linear fits to the Randles-Sevcik model. 50% RH has the largest slope and may be from a combination of improved diffusion from larger pores or a higher concentration from better adsorption. The other mesoporous samples also had larger slopes than AC and Super P. With coated samples, each sample had a higher slope than the 30% RH MPCNFs. Since each sample should have similar or more limited pores than the starting MPCNFs then the effective diffusion constant soon remain constant. The conclusion then should be for in an increase in bulk concentration.

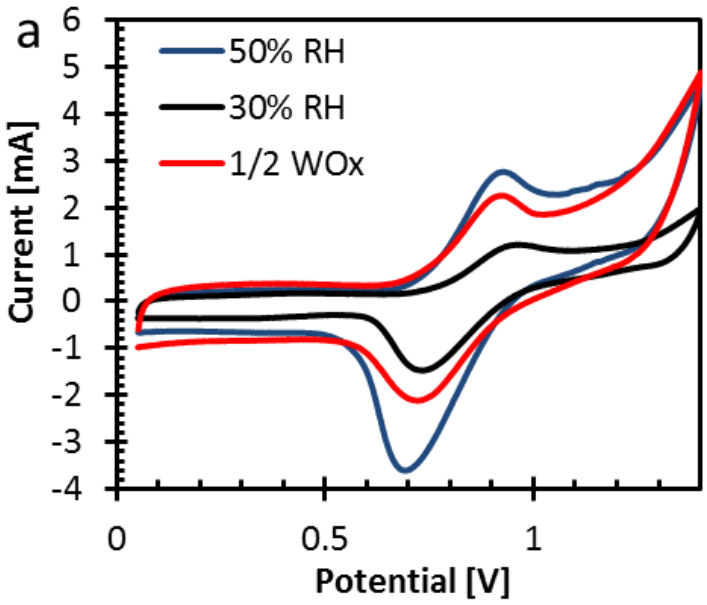

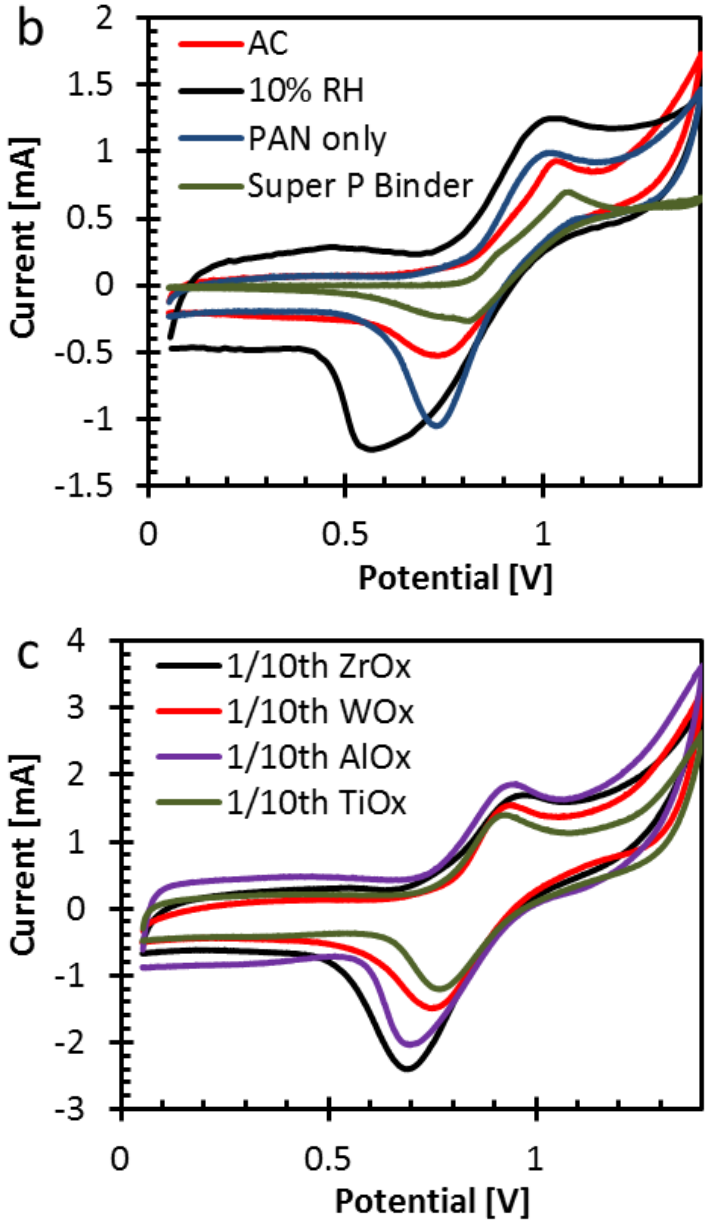

Figure 11: CV testing with Ag/AgCl reference electrode with 1M KCl at 10mV/sec of a) 50% RH MPCNF, 30% RH MPCNF, and one half diluted WOx coated MPCNF, b) AC, 10% RH MPCNF, PAN only nanofibers, and the Super P with PVDF binder, and c) diluted to one tenth metal oxide coated MPCNF.

Figures 12c-d), plot the voltage separation between the anodic and cathodic current peaks and the natural logarithm of the square root of the scan rate according to the Klingler and Kochi method.[44] The reaction rate constant for the reaction and surface should be proportional to the

inverse of the y-intercept, so the separation between peaks should be minimized as in an ideal reversible reaction for faster kinetics. Overall the peak separation at the lowest scan rate is mostly the same for all samples and a projection of the curves would lead to the conclusion that the reaction constant is relatively the same for all the samples.

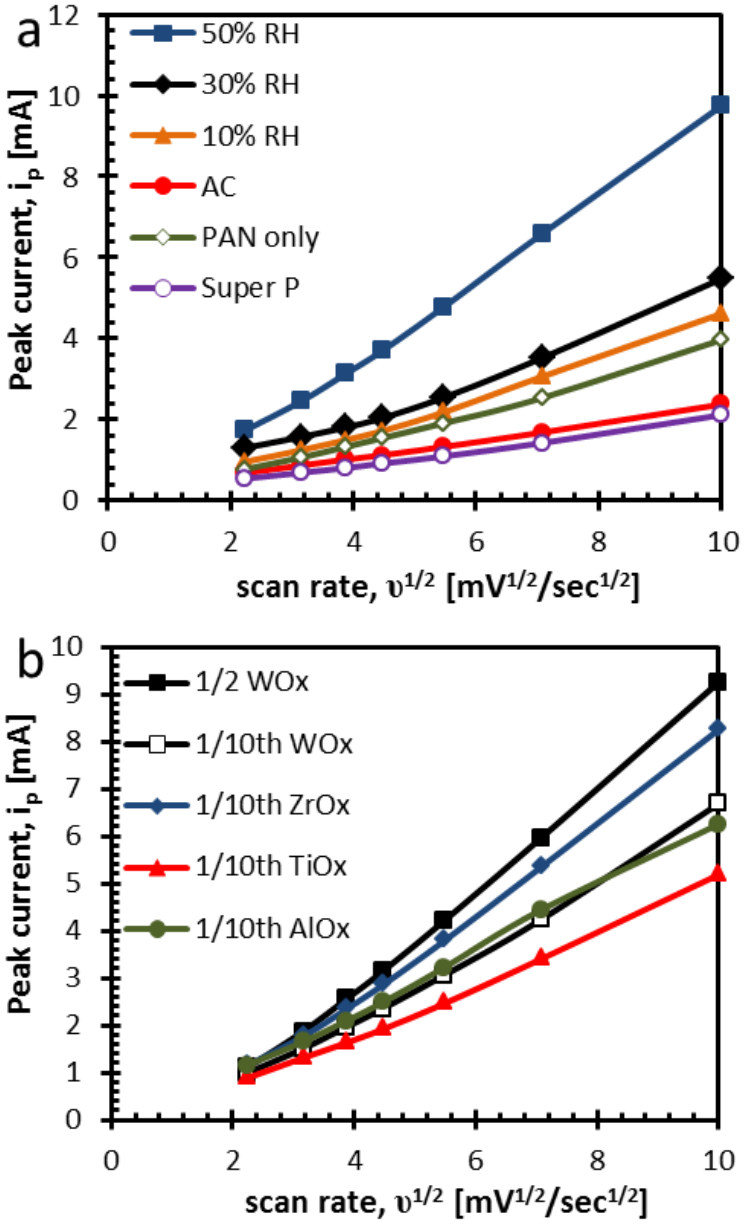

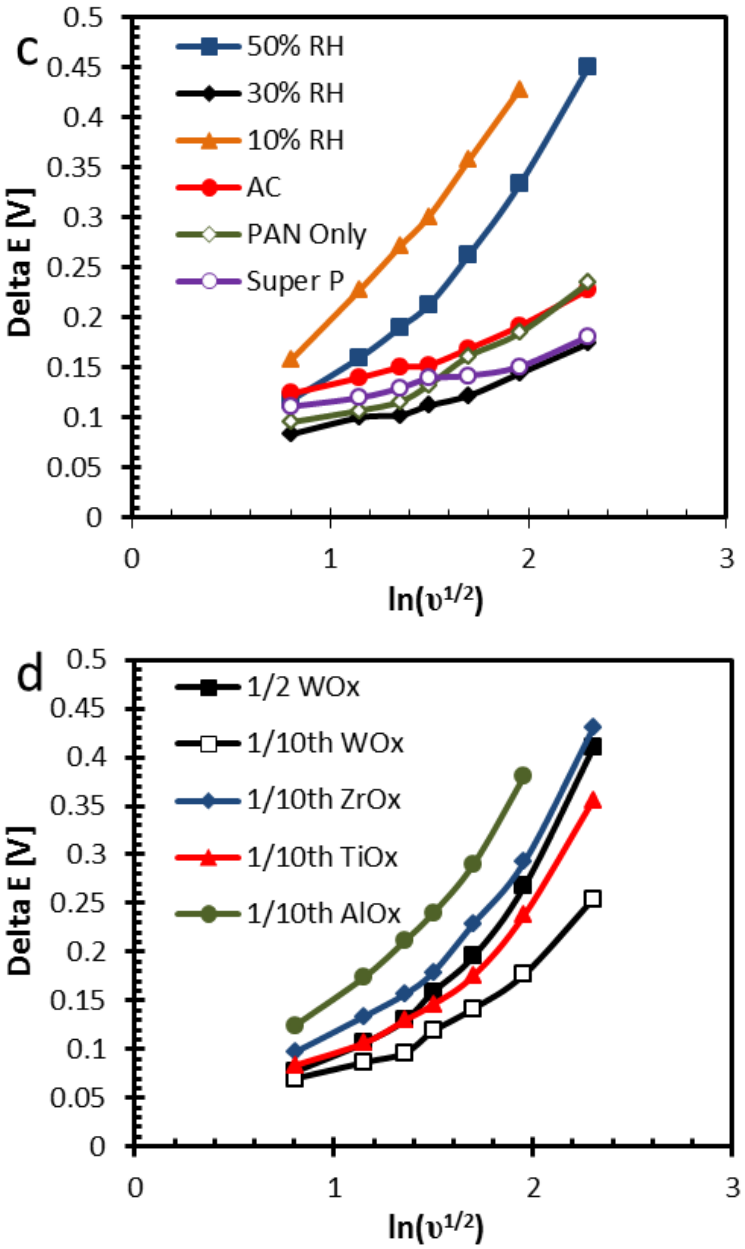

Figure 12: a) and b) are linearized Randles-Sevcik plots graphing the anodic peak current with the square root of the scan rate for coated and uncoated samples. c) and d) are linearized plots of the Klingler and Kochi method graphing the spread of the voltage of anodic and cathodic peak currents with the natural logarithm of the square rate of the scan rate.

4. Conclusions

Starting from a previous work, a hierarchical carbon composing of an activated macroporous carbon nanofiber mat with large tunable mesopores (>10nm) in the nanofibers were made and tested as zinc bromine redox flow battery cathodes. By controlling the humidity during electrospinning to 10% RH, 30% RH, and 50% RH, three sizes of mesopores were made. The largest mesopores (50nm+) were made at 50% RH and it demonstrated higher coulombic efficiency than AC especially at 30mA/cm^2 while 30% RH with the second largest pores demonstrated slight improvement over AC. While the enhanced performance could be from better diffusion through larger pores, a small change in pore size should not drastically alter the performance since only small molecules are diffusing through the pores that are far from the Knudsen regime. Therefore it is thought that the larger pores allow better adsorption of the phase separated bromine complex into the pore. From the first experiment dealing with the orientation of the cell, the importance of direct contact of the complex with the electrode is observed. When metal oxides were added, ZrO_x was found to superior in preventing side reactions with the complexing agent through 1000 deep charge cycle tests while WO_x had the best coulombic performance in galvanostatic testing, surpassing the base MPCNF. When the thickness of the coating was reduced in order to lower charge transfer resistance, ZrO_x improved its coulombic efficiency to a level above its base MPCNF as well. It was concluded that the metal oxide coatings improved performance by adsorbing the complex more strongly. This was concluded from impedance results where the coating lowered the charge transfer resistance lower than the base MPCNF and from the analysis of the CV testing where the higher slopes from the Randles-Sevcik plot would constitute a higher bulk concentration with near constant pore volume and thus similar diffusion limitations.

Acknowledgements

The authors would like to acknowledge Lotte Chemical for supplies and funding throughout this project and the Cornell Center for Materials Research Shared Facilities administration which is supported through the NSF MRSEC program (DMR-1120296).

REFERENCES

1. C. Ponce de León, a. Frías-Ferrer, J. González-García, D. a. Szánto, F.C. Walsh, Redox flow cells for energy conversion, J. Power Sources. 160 (2006) 716–732.
2. M. Skyllas-Kazacos, M.H. Chakrabarti, S. a. Hajimolana, F.S. Mjalli, M. Saleem, Progress in Flow Battery Research and Development, J. Electrochem. Soc. 158 (2011) R55.
3. A.Z. Weber, M.M. Mench, J.P. Meyers, P.N. Ross, J.T. Gostick, Q. Liu, Redox flow batteries: a review, J. Appl. Electrochem. 41 (2011) 1137–1164.
4. T. Nguyen, R.F. Savinell, Flow Batteries, Electrochem. Soc. Interface. Fall (2010) 54–56.
5. M.L. Perry, A.Z. Weber, Advanced Redox-Flow Batteries: A Perspective, J. Electrochem. Soc. 163 (2016) A5064–A5067.
6. K.H. Chua, Y.S. Lim, S. Morris, Cost-benefit assessment of energy storage for utility and customers: A case study in Malaysia, Energy Convers. Manag. 106 (2015) 1071–1081.
7. G. Rajarathnam, A. Vassallo, The Zinc/Bromine Flow Battery: Materials Challenges and Practical Solutions for Technology Advancement, SpringerBriefs in Energy (2016)
8. L. Zhang, H. Zhang, Q. Lai, X. Li, Y. Cheng, Development of carbon coated membrane for zinc/bromine flow battery with high power density, J. Power Sources. 227 (2013) 41–47.
9. S. Gu, K. Gong, E.Z. Yan, Y. Yan, A multiple ion-exchange membrane design for redox flow batteries, Energy Environ. Sci. 7 (2014) 2986.
10. P.C. Butler, P.A. Eidler, P.G. Grimes, S.E. Klassen, R.C. Miles, Zinc/bromine batteries, Handbook of Batteries. 3rd Ed. Chapter 39, Mc Graw-Hill (2002).
11. P. Eidler, Development of Zinc/Bromine Batteries for Load-Leveling Applications: Phase 1 Final Report, Sandia National Laboratories SAND99-1853 (1999)
12. H.S. Lim, A.M. Lackner, R.C. Knechtli, Zinc-Bromine Secondary Battery, J. Electrochem. Soc. Electrochem. Sci. Technol. 124 (1978) 1154–1157.
13. W. Kautek, a Conradi, C. Fabjan, G. Bauer, In situ FTIR spectroscopy of the Zn–Br battery bromine storage complex at glassy carbon electrodes, Electrochim. Acta. 47 (2001) 815–823.

14. G. Bauer, J. Drobits, C. Fabjan, H. Mikosch, P. Schuster, Raman spectroscopic study of the bromine storing complex phase in a zinc-flow battery, J. Electroanal. Chem. 427 (1997) 123–128.
15. W. Kautek, A. Conradi, M. Sahre, C. Fabjan, J. Drobits, G. Bauer, P. Schuster, In Situ Investigations of Bromine-Storing Complex Formation in a Zinc-Flow Battery at Gold Electrodes, 146 (1999) 3211–3216.
16. J.D. Jeon, H.S. Yang, J. Shim, H.S. Kim, J.H. Yang, Dual function of quaternary ammonium in Zn/Br redox flow battery: Capturing the bromine and lowering the charge transfer resistance, Electrochim. Acta. 127 (2014) 397–402.
17. E. Lancry, B.Z. Magnes, I. Ben-David, M. Freiberg, New Bromine Complexing Agents for Bromine bases Batteries, ECS Trans. 53 (2013) 107–115.
18. M.H. Chakrabarti, N.P. Brandon, S.A. Hajimolana, F. Tariq, V. Yufit, M.A. Hashim, M.A. Hussain, C.T.J. Low, P. V. Aravind, Application of carbon materials in redox flow batteries, J. Power Sources. 253 (2014) 150–166.
19. L.J.J. Janssen, J.G. Hoogland, MECHANISM OF BROMINE EVOLUTION AT A GRAPHITE ELECTRODE, Electrochim. Acta. 15 (1970) 1677–1683.
20. M. Mastragostino, C. Gramellim, KINETIC STUDY OF THE ELECTROCHEMICAL PROCESSES OF THE BROMINE / BROMIDE AQUEOUS SYSTEM ON VITREOUS CARBON ELECTRODES, Electrochim. Acta. 30 (1985) 373–380.
21. C. Wang, X. Li, X. Xi, W. Zhou, Q. Lai, H. Zhang, Bimodal highly ordered mesostructure carbon with high activity for Br2/Br− redox couple in bromine based batteries, Nano Energy. 21 (2016) 217–227.
22. M.E. Easton, P. Turner, A.F. Masters, T. Maschmeyer, Zinc bromide in aqueous solutions of ionic liquid bromide salts: the interplay between complexation and electrochemistry, RSC Adv. 5 (2015) 83674–83681.
23. D. Kim, J. Jeon, A Zn(ClO 4)2 Supporting Material for Highly Reversible Zinc-Bromine Electrolytes, Bull. Korean Chem. Soc. 37 (2016) 299–304.
24. G.P. Rajarathnam, M. Schneider, X. Sun, A.M. Vassallo, The Influence of Supporting Electrolytes on Zinc Half-Cell Performance in Zinc/Bromine Flow Batteries, J. Electrochem. Soc. 163 (2016) A5112–A5117.

25. S. Suresh, T. Kesavan, Y. Munaiah, I. Arulraj, S. Dheenadayalan, P. Ragupathy, Zinc–bromine hybrid flow battery: effect of zinc utilization and performance characteristics, RSC Adv. 4 (2014) 37947.
26. P. Singh, B. Jonshagen, Zinc-bromine battery for energy storage, J. Power Sources. 35 (1991) 405–410.
27. W.I. Jang, J.W. Lee, Y.M. Baek, O.O. Park, Development of a PP/carbon/CNT composite electrode for the zinc/bromine redox flow battery, Macromol. Res. 24 (2016) 276–281.
28. Y. Munaiah, S. Dheenadayalan, P. Ragupathy, V.K. Pillai, High Performance Carbon Nanotube Based Electrodes for Zinc Bromine Redox Flow Batteries, ECS J. Solid State Sci. Technol. 2 (2013) M3182–M3186.
29. Y. Munaiah, S. Suresh, S. Dheenadayalan, V.K. Pillai, P. Ragupathy, Comparative Electrocatalytic performance of single-walled and multiwalled carbon nanotubes for zinc bromine redox flow batteries, J. Phys. Chem. C. 118 (2014) 14795–14804.
30. C. Liang, Z. Li, S. Dai, Mesoporous carbon materials: synthesis and modification., Angew. Chem. Int. Ed. Engl. 47 (2008) 3696–717.
31. R. Ryoo, S.H. Joo, M. Kruk, M. Jaroniec, Ordered Mesoporous Carbons, Adv. Mater. 13 (2001) 677–681.
32. J. Lee, J. Kim, T. Hyeon, Recent Progress in the Synthesis of Porous Carbon Materials, Adv. Mater. 18 (2006) 2073–2094.
33. D. Ayme-Perrot, S. Walter, Z. Gabelica, S. Valange, Evaluation of carbon cryogels used as cathodes for non-flowing zinc-bromine storage cells, J. Power Sources. 175 (2008) 644–650.
34. R. Sahore, B.D.A. Levin, M. Pan, D.A. Muller, F.J. DiSalvo, E.P. Giannelis, Design Principles for Optimum Performance of Porous Carbons in Lithium-Sulfur Batteries, Adv. Energy Mater. 6 (2016) 1–9.
35. L. Estevez, R. Dua, N. Bhandari, A. Ramanujapuram, P. Wang, E.P. Giannelis, A facile approach for the synthesis of monolithic hierarchical porous carbons - high performance materials for amine based CO2 capture and supercapacitor electrode, Energy Environ. Sci. 6 (2013) 1785–1790.

36. Z.B. Wang, C.R. Zhao, P.F. Shi, Y.S. Yang, Z.B. Yu, W.K. Wang, G.P. Yin, Effect of a carbon support containing large mesopores on the performance of a Pt-Ru-Ni/C catalyst for direct methanol fuel cells, J. Phys. Chem. C. 114 (2010) 672–677.
37. G. Qi, L. Fu, B.H. Choi, E.P. Giannelis, Efficient CO2 sorbents based on silica foam with ultra-large mesopores, Energy Environ. Sci. 5 (2012) 7368.
38. J.H. Yang, H.S. Yang, H.W. Ra, J. Shim, J.D. Jeon, Effect of a surface active agent on performance of zinc/bromine redox flow batteries: Improvement in current efficiency and system stability, J. Power Sources. 275 (2015) 294–297.
39. B.P. Williams, Y.L. Joo, Tunable Large Mesopores in Carbon Nanofiber Interlayers for High-Rate Lithium Sulfur Batteries, J. Electro. Soc., in review.
40. M. Padmanaban, J. Cho, T. Kudo, D. Rahman, H. Yao, D. McKenzie, A. Dioses, S. Mullen, E. Wolfer, K. Yamamoto, Y. Cao, Y. Her, Progress in Spin-on Hard Mask Materials for Advanced Lithography, J. Photopolym. Sci. Technol. 27 (2014) 503–509.
41. K.T. Cho, M.C. Tucker, M. Ding, P. Ridgway, V.S. Battaglia, V. Srinivasan, A.Z. Weber, Cyclic Performance Analysis of Hydrogen/Bromine Flow Batteries for Grid-Scale Energy Storage, Chempluschem. 80 (2015) 402–411.
42. A. Yokochi. Degradation of Graphite Electrodes in Acidic Bromine Electrolytes, dissertation, Oregon State University. March 2013.
43. Z. Deng, Z. Zhang, Y. Lai, J. Liu, J. Li, Y. Liu, Electrochemical Impedance Spectroscopy Study of a Lithium/Sulfur Battery: Modeling and Analysis of Capacity Fading, J. Electrochem. Soc. 160 (2013) A553–A558.
44. D. Brownson, C. Banks, The Handbook of Graphene Electrochemistry, Chapter 2, Springer-Verlag (2014).
45. A. Bard; L. Faulkner, *Electrochemical Methods: Fundamentals and Applications*, 2 ed.. Wiley, (2000).

CHAPTER 5

Conclusions and Future Directions

Summary of Findings

- Chapter 2: Petcoke has a stronger preference for nonionic dispersants like Pluronic than high rank coals presumably due to low ash and volatiles content of the petcoke. A thick, strongly adsorbed layer was created by the best dispersants. Xanthan gum and Pluronic F127 competitively adsorb to the surface of petcoke where Pluronic slowly breaks up and out adsorb xanthan gum clusters which stabilize the slurry.
- Chapter 3: Interlayers for lithium sulfur batteries operate by a filter mechanism showing improvement to capacity retention at any sulfur loading studied. Large mesopores prevented pore narrowing at their opening at high charge and discharge rates. The thickness and weight of an interlayer matters significantly and improves capacity retention with increasing weight.
- Chapter 4: Large mesopores and metal oxide coatings both show improvements in coulombic efficiency even at higher charge rates. The large mesopores and metal oxides allow for better adsorption of the bromine containing complex which increases the readily available bromine needed for the redox reaction. ZrO_x also offers protection to the complexing agent in deep charges.

Future Directions

For the petcoke project the most interesting academic direction would be continuing to look at the interaction of the stabilizer and dispersants on model surfaces with varying degrees of hydrophobicity and different pairs of stabilizer and dispersants. The goal would be to find dispersant and stabilizer pairs and generalized conditions where the stabilizer would more strongly to the surface and each other than the dispersant without significantly increasing the yield stress. Industrially for petcoke, even simplest of block copolymers was thought to be too expensive of a dispersant. Industry preferred the superplasticizing polycarboxylates made industrially for cement applications with random grafting. However, perhaps a nonionic version of the polycarboxylates with grafted polyethylene oxide chains would be beneficial with petcoke where cements would prefer ionic dispersants.

On the mesoporous carbon nanofibers, PAN tries to shrink during stabilization and CDA is not a perfect form because CDA reaches its melting temperature at around the stabilization temperature and gives in to the shrinking a bit. A solution may be use cellulose triacetate instead which melts at an even higher temperature. Another solution may be to replace PAN and CDA with CDA and another pyrolyzing polymer and convert CDA to cellulose which would stabilize at a lower temperature and not shrink as much. Some fine tuning to the blend ratio may help the interconnectivity of the pores. Another idea to improve interconnectivity could be to freeze water in the nanofiber causing cracks like the lithium sulfide did in the interlayer project. Also, part of the blend polymer method was to make a cost effective mesoporous carbon with large mesopores. Experiments should be compared against Ketjen black, a major competitor in this aspect. Ketjen black is a hollow carbon black with diameters of the large mesopore range made in a very cost effective process.

As for lithium sulfur interlayers, the field of making a new material for use as an interlayer has been fairly well explored. Next would be industrial efforts and academic efforts to increase sulfur loading in three dimensional cathodes. Interlayers are not the entire solution to the problems facing lithium sulfur batteries but are an easy addition to improve performance. They should be a part of any industrial solution to lithium sulfur batteries because there are many options, even those that are simpler than the methods discussed in Chapter 3, to make a working interlayer with net positive impact.

For zinc bromine flow batteries, the binder solution used to bind the MPCNFs to the electrode is a problem since many pores are blocked by PVDF and the binder solution soaks into the nanofiber during binding. One solution, though more of an industrial solution, is to melt press the MPCNF onto a carbon plastic electrode. The melted plastic would probably not be drawn into the fiber mat like the binder solution does. Other ideas on the ZBB project include looking for a metal oxide which is catalytic or looking more into graphene and carbon nanotube dispersions and coatings which are thought to be catalytic. The dispersion of the carbon nanotubes or graphene can be explored by changing the polymer blend and the hydrophobicity of one of the components or change the functional groups on the surface. Finally, since a coating does add a layer of resistance, chemically functionalizing the surface is an area to look into and may protect the carbon electrode just as well.